

Copyright
by
Benjamin Thomas Cardenas
2019

**The Dissertation Committee for Benjamin Thomas Cardenas Certifies that this is
the approved version of the following Dissertation:**

The Accumulation and Preservation of Fluvial and Aeolian Strata

Committee:

David Mohrig, Supervisor

Gary Kocurek

Joel P.L. Johnson

Wonsuck Kim

Zoltan Sylvester

The Accumulation and Preservation of Fluvial and Aeolian Strata

by

Benjamin Thomas Cardenas

Dissertation

Presented to the Faculty of the Graduate School of

The University of Texas at Austin

in Partial Fulfillment

of the Requirements

for the Degree of

Doctor of Philosophy

The University of Texas at Austin

August 2019

Dedication

Dedicated to Rosemary, Ken, Nina, Lily, and Rebekah.

Acknowledgements

The chapters of this dissertation are taken from manuscripts either accepted for publication or approaching it, and these manuscripts have co-authors who have helped with field work, edits, and analysis. For their help, I must acknowledge Travis Swanson, Cory Hughes, Tim Goudge, Jasmine Mason, Joe Levy, Sarah Brothers, John Swartz, Feifei Zhao, and Eric Prokocki. May collaborations continue! I also must acknowledge my committee, who have provided discussions and guidance since my qualifying examination, and specifically Gary Kocurek who played an instrumental role in constructing Chapter 4 and helping develop my field senses. Finally, I feel that any scientific success I have had or will have can be traced back to David Mohrig. Over the last seven years, through the acquisition of two degrees, David has taught me to be critical and skeptical, to get my face in the rocks and actually measure where others had not, and to be collaborative. I also believe David has sculpted me into a geoscientist with a particularly relevant set of skills and experiences, far before I knew what that might mean. David, thank you.

Abstract

The Accumulation and Preservation of Fluvial and Aeolian Strata

Benjamin Thomas Cardenas, PhD

The University of Texas at Austin, 2019

Supervisor: David Mohrig

Sedimentary rocks are a record of the four-dimensional evolution of a planetary surface. Geomorphic features, including fluvial and aeolian dunes, river bars, and entire river channels move across Earth's surface. As Earth's surface evolves with this movement, sediment may accumulate in one location or be removed from another. In this way, through the unsteady processes of deposition and erosion, geomorphology is translated into stratigraphy, and time is lithified. Learning to read this record of Earth's surface evolution is a fundamental goal of sedimentology. This dissertation covers three contributions to this effort. Though the chapters cover different types of sedimentary systems (fluvial and aeolian) at different scales (outcrop and seismic imaging), the fundamental driving questions are largely the same: which elements of the ancient sedimentary systems have been preserved? How is time represented? How do internal processes and external forcings control what makes it into the rock record? Chapter 2 is an examination of exhumed fluvial channel belts of the Cretaceous Cedar Mountain Formation, Utah, USA. Analysis of outcrop mapping and vertical and lateral sections

confirm the preservation of complete barforms, river bed topography, and the formative channel-belt centerline. These features are representative of an aggradational fluvial system avulsing at rapid rates compared to lateral migration rates. Additionally, the preserved strata were constructed rapidly, indicating most of the time recorded in the channel belts is flattened onto erosional surfaces at the bases of each channel belt. Chapter 3 looks at fluvial channel belt preservation at the km scale, using seismic reflection volumes of the subsurface Gulf of Mexico offshore of the Brazos river delta, Texas, USA. Channel belts of two distinct preservation qualities are observed, and their stratigraphic arrangement confirms that a recently discovered source of relief in coastal zones aids in the preservation of channel belts. Chapter 4 discusses an outcrop study of the aeolian Page Sandstone, Arizona, USA. The Page is the record of multiple stacked, generally bypassing dune fields, only preserved because of a fluctuating water table. The lack of dune field aggradation is attributed to a lack of external processes forcing deposition. An exception is found within antecedent topographic depressions, which have preserved climbing cross-sets built by small dunes during the earliest phases of dune field development. Such deposits are absent from the rest of the Page, as they are inevitably reworked in the absence of available antecedent topography.

Table of Contents

Chapter 1: Introduction.....	1
Chapter 2: Anatomy of an exhumed river-channel belt.....	6
2.1 Introduction.....	6
2.1.1 Background.....	7
2.1.1.1 Cedar Mountain Formation.....	7
2.1.1.2 Dune, bar, and channel belt strata.....	10
2.2 Methods.....	12
2.2.1 Field campaign.....	12
2.2.2 Modern analogs and the transport anomaly.....	13
2.3 Results.....	18
2.3.1 Vertical sections.....	18
2.3.2 Sedimentary structures and architecture.....	19
2.3.3 Transport anomalies.....	30
2.4 Discussion.....	39
2.4.1 Dune, bar, belt, and overbank strata.....	39
2.4.2 Channel bed topography.....	41
2.4.3 Channel planform geometry.....	43
2.4.4 Channel-belt thickness.....	43
2.4.5 Reconstructing river-bed kinematics.....	44
2.4.5.1 Dune motion on bars and in the thalweg.....	44
2.4.5.2 Constraints on the time recorded by individual channel belts.....	49
2.4.6 Comparison to other fluvial systems and strata.....	55

2.5 Conclusions.....	56
2.6 Acknowledgements.....	57
Chapter 3: Setting Up the Preservation of Fluvial Channel Belts	58
3.1 Introduction.....	58
3.2 Methods	61
3.3 Results.....	65
3.4 Discussion.....	69
3.5 Conclusions.....	75
3.6 Acknowledgements.....	76
Chapter 4: Autogenic processes and allogenic forcings preserved in aeolian strata	77
4.1 Introduction.....	77
4.1.1 Geologic context and previous work	81
4.1.2 Aeolian stratification types	84
4.1.3 Aeolian set architecture	85
4.2 Methods	87
4.2.1 Field Work	87
4.2.2 Data processing.....	88
4.2.3 Numerical modeling	89
4.3 Results.....	90
4.3.1 Outcrop-scale architecture	90
4.3.2 Outcrop-scale bounding surfaces.....	90
4.3.3 Cross-set architecture.....	98
4.3.3.1 Basal Page architecture	98

4.3.3.2 Lower and middle Page architecture.....	101
4.3.4 Results of numerical modeling	104
4.4 Discussion.....	108
4.4.1 Interpretation of cross-strata	108
4.4.2 Stratigraphic architecture and outcrop-scale bounding-surface topography	110
4.4.2.1 Architecture preserved in antecedent J-2 topography.....	110
4.4.2.2 Scour-and-fill architecture and coeval development of relief on outcrop-scale bounding surfaces.....	111
4.4.3 Dune-Field Kinematics from Set-Thickness Distributions.....	113
4.4.4 Reconstruction of the middle Page dune fields	118
4.4.5 Role of Autogenic vs. Allogenic Controls on the Page Preserved Record.....	120
4.5 Conclusions.....	122
4.6 Acknowledgements.....	122
Chapter 5: Conclusions.....	124
Appendix.....	127
References.....	130

Chapter 1: Introduction

Sedimentary rocks are a record of the four-dimensional evolution of a planetary surface. Geomorphic features, including fluvial and aeolian dunes, river bars, and entire river channels move across Earth's surface. As Earth's surface evolves with this movement, sediment may accumulate in one location or be removed from another. In this way, through the unsteady processes of deposition and erosion, geomorphology is translated into stratigraphy, and time is lithified. Learning to read this record of Earth's surface evolution is a fundamental goal of sedimentology. This dissertation covers three contributions to this effort. Though the chapters cover different types of sedimentary systems (fluvial and aeolian) at different scales (outcrop and seismic imaging), the fundamental driving questions are largely the same: which elements of the ancient sedimentary systems have been preserved? How is time represented? How do internal processes and external forcings control what makes it into the rock record?

Chapter 2 discusses a field study of ancient fluvial strata. Sediment transport processes variably rework and preserve existing strata during the formation of new deposits. The degree of reworking and preservation of a sedimentary deposit is therefore a key to understanding its formative processes. To understand the preservation of fluvial channel belts, preserved elements of the formative river channels, including bars, planform geometry, and bed topography, are sought within exhumed fluvial strata exposed as ridges in the Cretaceous Cedar Mountain Formation, Utah, USA. High-resolution photopans created by Unmanned Aerial Vehicles facilitated geologic field mapping, and were

combined with vertical and lateral sections. The studied ridges are compound structures composed of the stacked deposits of multiple, individual channel belts representing 5 to 6 channel re-occupations. Lateral sections reveal bar strata made up of sets of dune cross-beds constructing well-preserved barforms. Locally, the paleo-topography of Cretaceous-age barforms even defines the upper surface of the outcrop. Comparison of the channel-belt centerline to local paleotransport directions indicate channel planform was preserved through multiple re-occupations and minimal lateral migration. The preservation of these channel elements is the product of the kinematics of the depositional system. Rapid avulsions preserve the final state of the active channel bed and its individual bars. Frequent avulsions with respect to lateral migration rates minimize lateral channel amalgamation. A frequently avulsing river system also favors multiple channel re-occupations. Calculated sedimentation times vary within the belt from a day to 16 days, indicating most of the time recorded in these compound channel belts is represented by basal erosional surfaces. The well-preserved belts may be indicative of a higher-order topography driving sedimentation at the belt scale, much as bar topography can increase dune sedimentation rates and preservation. This work provides a foundation for future studies connecting properties of fluvial systems to the construction of channel-belt strata.

Chapter 3 examines the preservation of fluvial strata at the scale of seismic reflection imaging. A significant source of relief was recently recognized along coastal plains of the US Gulf of Mexico and Atlantic, regions generally considered flat. Alluvial ridges, built from aggraded channel beds, bound topographically-low regions which develop tributary drainage networks initiating at the bounding ridges and draining into the

gulf. Does this relief drive variability in fluvial sedimentation, thus controlling the way coastal river-channel belts accumulate and become preserved in the rock record? To answer this, buried fluvial channel belts are mapped in a 3D seismic volume offshore of the Brazos river delta, Texas, USA. Fluvial channel belts of two distinct preservational qualities are distinguished based on their length normalized to their width: a poorly-preserved population with a mean normalized length of 2.4, and a well-preserved population with a mean normalized length of 22.2. These two populations of belts are found within the same planview extent, and in close proximity of each other in terms of burial depth. Consistently, the poorly-preserved belts can be used to define stratigraphic surfaces which the well-preserved belts sit directly above or scour slightly into. The surfaces defined by poorly-preserved belts are interpreted to represent the basal surfaces of coastal tributary basins, which are consistently reworked without significant sediment accumulation. The belts sitting above these surfaces record the sudden occupation and filling of these basins following avulsions of major river systems. Both the focused sedimentation and the protection offered by the basin prevent the major reworking of these well-preserved belts, resulting in a well-preserved belt recording ‘strangely ordinary’ transport conditions.

Chapter 4 covers an in-depth field study of an aeolian sandstone. The stratigraphic architecture of aeolian sandstones is thought to record signals originating from both autogenic dune behavior and allogenic environmental boundary conditions within which the dune field evolves. Mapping of outcrop-scale surfaces and sets of cross-strata between these surfaces for the Jurassic Page Sandstone near Page, Arizona, USA, demonstrates that the stratigraphic signature of autogenic behavior is captured by variable scour depths and

subsequent fillings, whereas the dominant signatures of allogenic boundary conditions are associated with antecedent surface topography and variable water-table elevations. At the study area, the Page Sandstone ranges from 55 to 65 m thick and is separated from the underlying Navajo Sandstone by the J-2 regional unconformity with meters of relief. Thin, climbing sets of cross-strata of the basal Page representing early dune-field accumulations fill J-2 depressions. In contrast, the overlying lower and middle Page consist of cross-strata ranging from less than 1 to 15 meters thick (average 2.44 m), and packaged between outcrop-scale bounding surfaces, though parts of the lower Page are bounded from beneath by the J-2. These bounding surfaces have been previously correlated to high stand deposits of the adjacent Carmel sea and at this site possess up to 13 meters of erosional relief produced by dune scour. Notably absent in packages of cross-strata bounded by these outcrop-scale surfaces are strata of early dune-field accumulations, any interdune deposits, and climbing-dune strata. Instead, these packages preserve a scour-and-fill architecture created by large dunes migrating in a dry, mature, dune field undergoing negligible bed aggradation. Any record of early phases of dune-field construction for the lower and middle Page are interpreted to have been cannibalized by the deepest scours of later, large dunes. Interpretations are independently supported by the relatively large coefficients of variation (c_v) in middle Page set thicknesses ($c_v = 0.90$), which are consistent with set production by successive deepest trough scours, the relatively low coefficient of variation for the depression-filling basal Page and lower Page sets consistent with a significant component of bed aggradation in J-2 depressions ($c_v = 0.64$ and 0.49), and the fit of set thickness distributions to established theory. Numerical modeling presented here and more

completely in the companion paper demonstrates how this cannibalization of early-phase stratigraphy is an expected outcome of autogenic dune-growth processes, and that early-phase strata can be preserved within antecedent depressions. Relative rise of the inland water table from basin subsidence and changing Carmel sea level forced preservation of 5-6 stacked packages composed of scour-and-fill architecture. Without these allogenic forcings, the Page would be little more than an erosional surface.

Chapter 2: Anatomy of an exhumed river-channel belt

2.1 INTRODUCTION

Fluvial channel belts are the time-integrated, channel-filling deposits of rivers. These channel-filling deposits include strata associated with bedforms, such as ripples and dunes, as well as free and forced bars. The vertical and lateral motion of a river is recorded by the motion of these bedforms and bars, which in turn control the geometry of the resultant channel-belt deposits and drive the belt's geometry away from that of the formative river (Van De Lagewag et al., 2013). Therefore, a successful pathway towards understanding the way ancient rivers migrated, aggraded, and avulsed, is to understand the accumulation and preservation of the bedform and barform strata within the associated channel belts (e.g., Reesink et al., 2015; Durkin et al., 2018; Paola et al., 2018; Chamberlin and Hajek, 2019).

This work examines an erosionally exhumed, laterally and vertically amalgamated complex of fluvial channel belts in the Cretaceous Cedar Mountain Formation, Utah, USA (Fig. 2.1) in order to determine what aspects of ancient river bathymetry and form are partially-to-fully preserved within the channel belts. Paleo-environmental properties such as water and sediment discharge associated with an ancient fluvial system can be quantitatively estimated using geometric properties of its paleo-channels, if these geometries can be accurately estimated from deposits representing the time-integrated record of channel motion, deposition, and erosion. Our goal is to develop methodologies for extracting the river-channel kinematics from channel-belt deposits so that the most accurate picture of the channel that built a belt can be established. In the process, what the

belt deposits actually represent can be determined. For example, were these belts produced during incremental sedimentation, or do they represent a snapshot of the channel topography at the time of avulsion? This topography includes barforms and bedforms, as well as planform channel geometry. The measurements presented here cover the channel belts across a range of scales, from local stacks of cross sets to the entirety of the outcrop, in order to understand the Cedar Mountain producing river system. The datasets analyzed in this work include Unmanned Aerial Vehicle (UAV) images, field maps, vertical and lateral sections, modern river analogs, and another ancient example in the nearby Jurassic Morrison Formation. These methods and results provide a good comparative baseline for future studies of fluvial channel belts and their associated ancient fluvial systems. The reconstruction of bed aggradation rates using these methods will also further the community's understanding of how time in the rock record is recorded by preserved strata and erosional surfaces (Sadler, 1981; Paola et al., 2018).

2.1.1 Background

2.1.1.1 Cedar Mountain Formation

The rivers associated with the deposition of the lower Cretaceous Cedar Mountain Formation drained uplifted areas of modern-day western Utah northeastward into the Mowry Sea and its successor, the Western Interior Seaway. Ultimately, basin subsidence led to the burial of the Cedar Mountain Formation by late Cretaceous coastal and marine

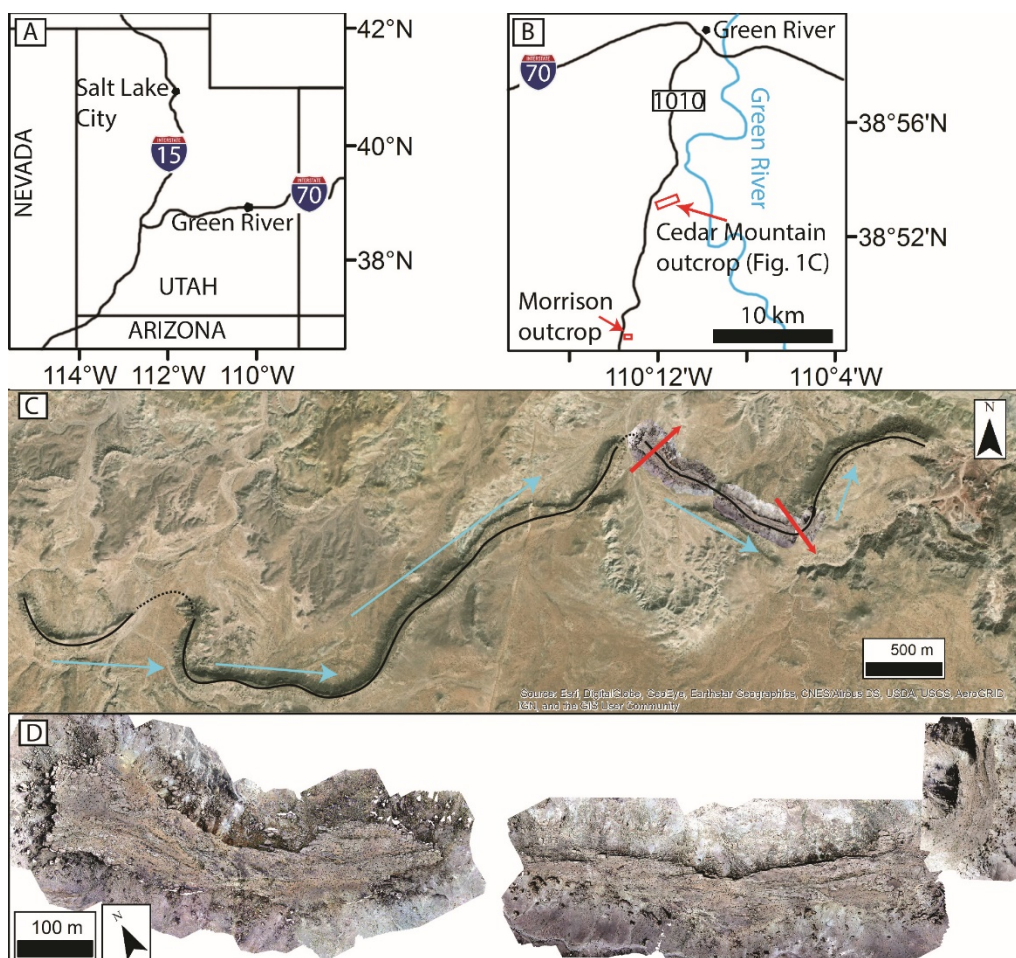


Figure 2.1 (A) Map of Utah showing major highways, Salt Lake City and Green River. (B) Zoom in near Green River, showing the location of the town as well as the studied ridges of the Cedar Mountain and the Morrison Formation south of town along 1010. (C) Zoomed out view showing the Cedar Mountain ridges beyond the study area. A black lines maps out a ridge centerline for several km, with interpreted dashed segments bridging erosional discontinuities. Teal arrows show the general direction of paleoflow. Red arrows mark the two major bends bounding the studied part of the ridge. The arrows point away from the center of curvature, and match with the general dip directions of local dipping bar strata. (D) Drone photomosaics of the studied eastern and western ridges of the Cedar Mountain Formation ridges overlying an aerial photo basemap. The photomosaics are rotated slightly to fit the panel, but are correctly co-located.

deposits of the Dakota Sandstone and the Mancos Shale (Currie, 1998). A regional unconformity separates the base of the Cedar Mountain Formation from the top of the upper Jurassic Morrison Formation (Peterson and Ryder, 1975; Kowallis et al., 1986). The Cedar Mountain Formation has been interpreted as consisting of river channel-filling sandstones and conglomerates, and overbank mudstones and paleosols (Stokes, 1961; Currie, 1998; Garrison et al., 2007; Nuse, 2015; Hayden et al., 2019).

Much of the recent work regarding the Cedar Mountain Formation has focused on the geomorphology of exhumed channel-filling deposits. The channel belts are more resistant than the surrounding floodplain material, resulting in the preferential erosion of floodplain strata and preservation of the channel fill (Williams et al., 2007; 2009; Hayden et al., 2019). The landscape within the eroding Cedar Mountain is defined by ridges as tall as 35 m and 60-90 m wide on average, composed of exhumed channel belts that are exposed in three dimensions. The recent interest in these landforms and other exhumed channel fills (e.g., Hayden et al., 2019; in Oman, Maizels 1987, 1990; Maizels and McBean, 1990; in Egypt, Zaki et al., 2018) has partially been driven by high-resolution images of similar ‘fluvial sinuous ridges’ on Mars (e.g., Burr et al., 2009; Davis et al., 2016; Cardenas et al., 2018; Hughes et al., 2019). Hayden et al. (2019) have provided an important comparison between field and remote-sensing based, paleo-hydraulic reconstructions for the Cedar Mountain Formation ridges, but a detailed sedimentologic workup provides additional information for any paleo-environmental analysis.

2.1.1.2 Dune, bar, and channel belt strata

The dip direction of a dune cross stratum records the orientation of the formative dune lee face, and reflects local dune migration direction (Allen, 1970b; Rubin and Hunter, 1982). This relationship is complicated for dunes with sinuous crestlines and variably deep troughs, which create trough cross-stratification (McKee and Weir, 1953; DeCelles et al., 1983; Rubin, 1987). Because of the sinuosity, the local dip direction of a set of trough cross-stratification may represent the mean migration direction of the associated dune plus or minus as much as 90° (Dott Jr., 1973). In planview exposures where all of this variability can be seen together, the central axis of a set of trough-cross strata is clearly seen and migration direction is unambiguously determined (Dott Jr., 1973).

Dipping strata composed of superimposed sets of dune cross strata, represent the accretion surfaces of larger-scale barforms. In active rivers, barforms are either forced by channel shape or are free to migrate downstream (Miall, 1977; Seminara and Tubino, 1989; Ikeda, 1989; Hooke and Yorke, 2011). Bars fixed to the inner bank of a channel bend, i.e., point bars, grow into the channel (Ikeda et al., 1981) and record lateral river migration, and have been identified in the rock record based on sigmoidal lateral accretion surfaces dipping at approximately perpendicular angles to the local dip directions of dune cross strata (e.g., Edwards et al., 1983; Wu et al., 2015; Almeida et al., 2016). Free bars may preserve a wider array of relationships between local dune migration direction and the bar surface dip direction (e.g., Allen, 1983; Almeida et al., 2016). Although not commonly discussed in the literature, free bars and forced (point) bars do commonly coexist in

channels (Fig. 2.2A to D; Kinoshita and Miwa, 1974; Whiting and Dietrich, 1993; Hooke and Yorke, 2011).

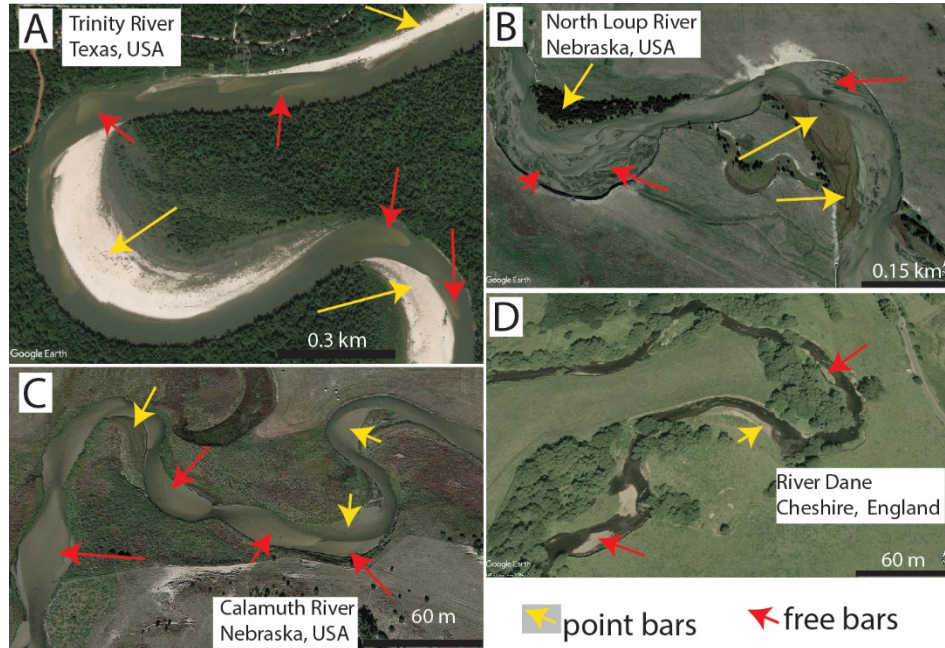


Figure 2.2 Free bars (red arrows) and point bars (yellow arrows) commonly coexist in rivers, both in straight reaches and bends. (A) Trinity River, Texas, USA. Image centered at 30.134° N, -94.815° E. (B) North Loup River, Nebraska, USA. Image centered at 42.019° N, -100.098° E. (C) Calamuth River, Nebraska, USA. Image centered at 42.083° N, -99.649° E. (D) River Dane, Cheshire, England. Image centered at 53.183° N, -2.259° E.

In net-depositional settings, aggradation of the riverbed is coupled with aggradation of the channel margins that exceeds distal floodplain aggradation (Pizzuto, 1987). Over time, the channel becomes elevated relative to the floodplain, and the difference between the two elevations is the channel's superelevation. Mohrig et al. (2000) discussed a system where a superelevation of 0.6 times flow depth characterized the threshold for river avulsion, the process by which flow abandons a channel in favor of a lower topographic position (Heller and Paola, 1996; add more). Studies of both modern and ancient avulsive

rivers suggest that rivers tend to return to once abandoned channels that became gravitational attractors to flow following the aggradation of the adjacent floodplain (Heller and Paola, 1996; Reitz et al., 2010; Edmonds et al., 2016). Such systems leave behind channel-belt complexes, sedimentary deposits composed of stacked channel-belts (Friend, 1979; Mohrig et al., 2000; Jones and Hajek, 2007; Cuevas Martínez et al., 2010; Chamberlin and Hajek, 2015; Hayden et al., 2019).

2.2 METHODS

2.2.1 Field campaign

For this study, several datasets were acquired during a field campaign at two ridges formed from exhumed fluvial channel belts of the Ruby Ranch Member of the Cedar Mountain Formation (Fig. 2.1A and B). Aerial drone photosurveys, collected with a DJI Phantom 2 Vision Plus UAV, imaged the top surfaces of both ridges with >75% along path and side overlap in photos (Fig. 2.1C-D). Using ground control points and the GPS point for each photograph, the Agisoft PhotoScan software package created both photomosaics from the common point detection in overlapping photos. Photomosaics of orthorectified image data have pixel lengths of 0.05 m, and cover an area of 213,000 m² over the eastern and western ridges (Fig. 2.1C to D). These datasets were used to map the locations of bounding surfaces of cross-sets of various scales and major erosional surfaces. Cross-strata dip directions were measured for each cross-set by two workers using compasses. During this survey, each set was classified as either being composed of sandstone or conglomerate.

In addition to the planview data, several sets of vertical sections were logged at separate times, at separate scales, with distinct goals. Around the perimeters of each ridge, 59 vertical sections were measured covering the entirety of the available vertical exposure of the ridge-capping rock, resulting in 276 total meters of section. Collecting the thicknesses of units between major bounding surfaces was the primary goal of this effort. During a separate survey, we documented an additional 31 2-D panels ranging from 1 m to 10 m wide around the perimeters of both ridges in order to describe the smaller, cross-set scale architectural elements of the channel belts. Architectural variability in the transport direction at the scale of a few meters was recorded, including changes in set thickness and the dips of bounding surfaces. Across all of these surveys, the thickness of 362 sets of cross strata were measured, and grain size was measured for 75 of those sets in the field using a grain size card. Using a geographic information system (GIS), field mapping results were merged with the remote sensing measurements. Ridge-scale bounding surfaces were digitized as lines, and 1,071 sets of planform exposed trough cross strata and 107 exposures of large-scale dipping strata were digitized as polygons.

2.2.2 Modern analogs and the transport anomaly

To test how well the ridge centerlines represent original channel centerlines, a metric named here as the transport anomaly, Θ_{TA} , is defined for both modern rivers and the exhumed channel fills.

$$\Theta_{TA-CHANNEL} = \Theta_{CL-CHANNEL} - \Theta_{D-CHANNEL} \quad (1a)$$

$$\Theta_{TA-RIDGE} = \Theta_{CL-RIDGE} - \Theta_{D-RIDGE} \quad (1b)$$

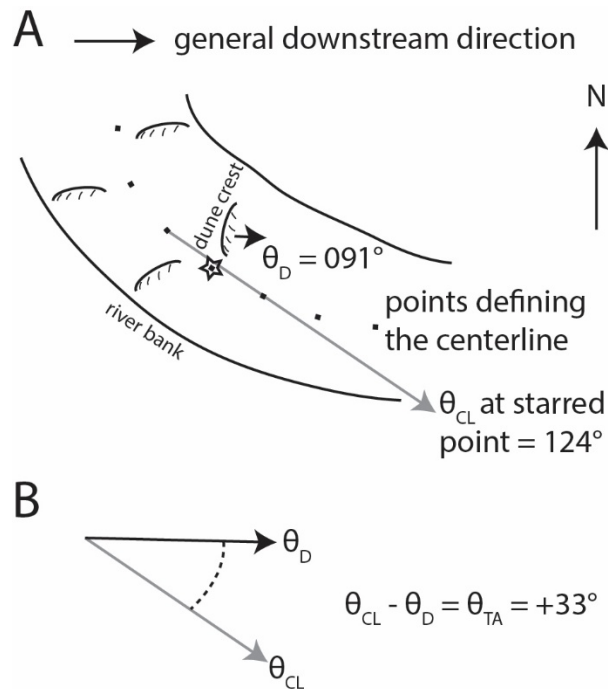


Figure 2.3 (A) Diagram defining the components of the transport anomaly, θ_{TA} . A measurement of transport direction, θ_D , is made from the orientation of a dune crest (short black arrow; 091°). The centerline point closest to the measurement of θ_D is starred. The orientation of the starred centerline point, θ_{CL} , is defined as the trend of the ray originating at the adjacent upstream point and passing through the adjacent downstream point (gray arrow; 124°). (B) The transport anomaly, θ_{TA} , is defined as $\theta_{CL} - \theta_D$. It may be positive or negative, and is bound between -180° and positive 180° . In this scenario, $\theta_{TA} = 124^\circ - 091^\circ = 33^\circ$.

where θ_D is the $0 - 359^\circ$ orientation of a transport or paleotransport measurement from an active dune ($\theta_{D-CHANNEL}$; Eq. 1a) or cross set ($\theta_{D-RIDGE}$; Eq. 1b), and θ_{CL} is the orientation of the centerline nearest to the location where θ_D was measured (Fig. 2.3). Values of θ_{TA} may be positive or negative, and are calculated using the Circular Statistics Toolbox available for MATLAB, which measures the shortest angular distance, positive or negative, between the two directions such that no measurement exceeds 180° or is less than -180° (Berens, 2009). By measuring $\theta_{D-CHANNEL}$ from dunes in modern rivers and $\theta_{TA-RIDGE}$ from

planform-exposed cross sets in the Cedar Mountain, hundreds of measurements of Θ_{TA} (Eq. 1a to b) between the two systems were compared to understand how well the centerlines of formative Cedar Mountain rivers are preserved in the exhumed channel belts and represented by ridge geometry (Fig. 2.4A and B). For example, if the mean and standard deviation (σ) of $\Theta_{TA-RIDGE}$ (Eq. 1b) approximately equal those of $\Theta_{TA-CHANNEL}$ (Eq. 1a), then the transport anomaly of the Cedar Mountain is no greater than the variability in a modern river, and is consistent with ridge planform preserving the formative channel planform (Fig. 2.4A). If lateral migration and reworking has greatly widened the belt and reduced its overall sinuosity from that of the formative channels, σ should be greater in the Cedar Mountain, as well as a more random distribution of $\Theta_{TA-RIDGE}$ (Fig. 2.4B). For example, visual inspection of point bar strata of the Ferron Sandstone in Wu et al., (2015, their Fig. 13; 2016, their Fig. 8) shows a general northwest-curving paleotransport trend along a northeast trending exposure, making their study location a high paleo-transport anomaly zone. Note that the deviation angle in Wu et al. (2016) is calculated relative to an interpreted channel-form, not the exhumed channel-belt shape. Wang and Bhattacharya (2017) show a more pronounced example linked to point bar growth in their Figure 10A. Durkin et al. (2018) show examples of this lateral amalgamation in ancient (McMurray Formation) and the modern (Mississippi and New Madrid Rivers). In a third scenario where erosion patterns have not exhumed the belt relatively evenly from all directions, neither of the prior scenarios would be observed.

Measurements from active dune fields in a braided reach of the North Loup River, Nebraska, USA, and the meandering Trinity River, Texas, USA, were used in this analysis.

The North Loup is a sand bed river that has been used as a modern analog to ancient fluvial strata (Mohrig et al., 2000; Mahon and McElroy, 2018). We used a UAV photomosaic collected by Swanson et al. (2018), which images a 760 m reach of the river in which downstream migrating bars and dunes, as well as the channel banks, are clearly identifiable. The evolution of the Trinity River has recently been studied in detail using topographic and bathymetric datasets (Mason and Mohrig, 2018; in review). These datasets provide 32 river km to map dune crests on the river bed, as well as dunes formed during bankfull flow and currently stranded on subaerially-exposed point bar surfaces.

Points defining the centerlines of each river were calculated using the series of points defining each channel bank. For each point on one bank, the distance to the nearest point on the opposite bank is calculated and taken as a local width measurement, and a centerline point is placed at the location exactly between the two points. The North Loup banks, and therefore the centerline, are defined by points spaced about 1 m apart, approximately that of a representative dune wavelength in the North Loup River (Swanson et al., 2018). As validation of these width measurements, the average channel width is also calculated as the area bound by the channel banks divided by the length of the centerline. The difference in average width between the 2 methods is less than 2%. In a GIS, the brink lines of 2,871 dunes covering a 763-m reach of the river using an orthorectified UAV photomosaic. The orientation of each dune was estimated by a best-fit line to a series of mapped brink points. The normal to each brink line, in turn, was taken as the local transport direction for that dune, $\theta_{D-CHANNEL}$. $\theta_{D-CHANNEL}$ was then tied to a point located at the average XY coordinate of all XY coordinates defining that particular dune brink line. The

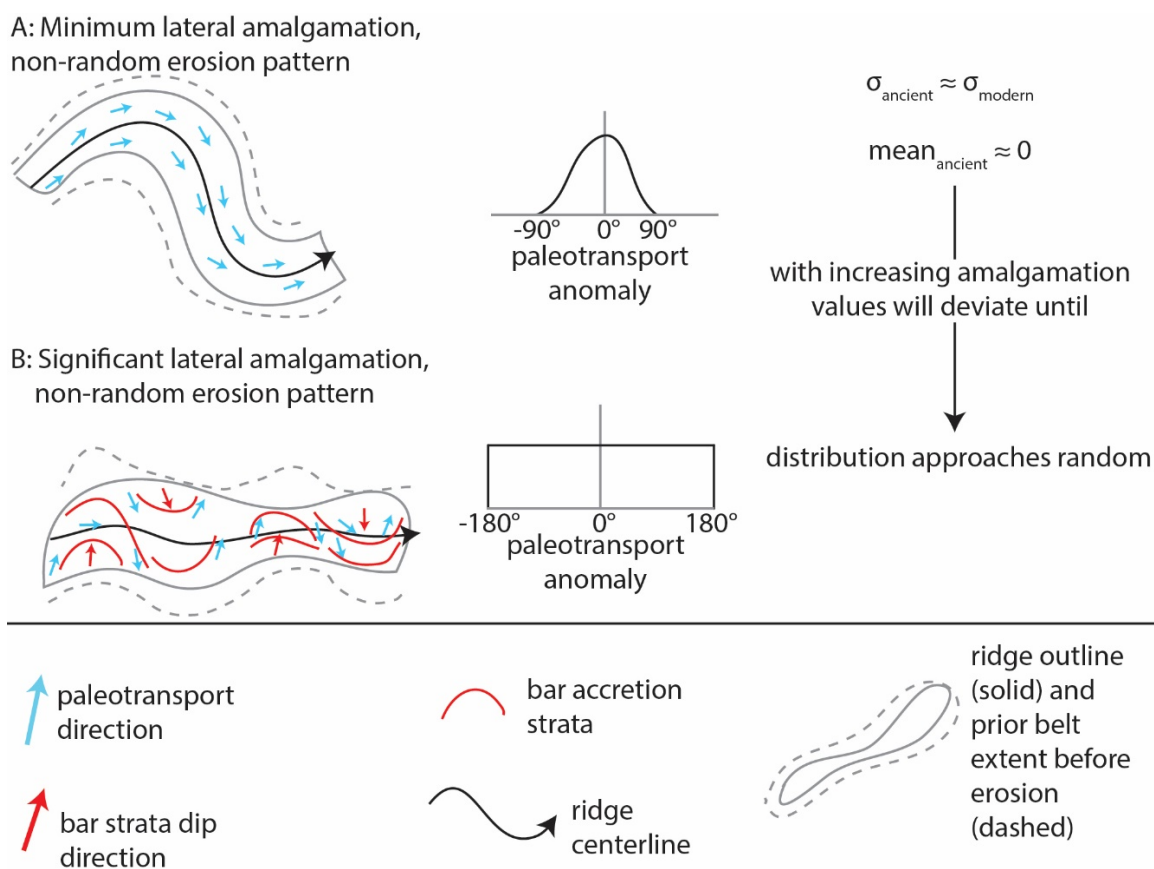


Figure 2.4 Hypothesized scenarios guiding interpretations of paleotransport anomaly results. Schematic diagrams are on the left, the distribution of paleotransport anomaly measurements are in the middle, and relevant statistical moments are on the right. Standard deviation is shown by σ . Legend is at the bottom. (A) The ridge centerline represents well the formative channel centerline. With increasing lateral amalgamation, results will instead approach the scenario in panel B. (B) Lateral amalgamation of the channel-belt separates any formative channel centerline from the ridge centerline. Laterally-accreting bar strata are preserved. A random exhumation pattern not following the edges of the channel belt is unlikely to show any of these patterns.

same process was applied to 2,190 bedforms over the imaged 32 km reach of the Trinity River imaged using sonar profiles of dunes on the channel bed (dataset from Mason and Mohrig, in review), as well as dunes frozen on subaerially exposed point bar surfaces formed during the previous bankfull flood imaged in a 2015 lidar survey (Mason and

Mohrig, 2018). In the Cedar Mountain, ridge centerlines were calculated using mid-points between the left- and right-hand ridge edges, and smoothed using a spline method in the MATLAB curve fitting toolbox. Centerlines are ultimately defined as points spaced ~1 m apart along the smoothed line. Ridge width was measured at 10 m intervals along the centerline. Values for $\Theta_{D-RIDGE}$ are taken from field measurements of planform trough cross strata across the top surfaces of the two ridges ($n = 1,071$), and assigned associated XY coordinates at the center of each mapped set.

2.3 RESULTS

2.3.1 Vertical sections

The measured vertical sections from around the perimeters of each ridge were composed of over 99% cross-stratified sandstones and conglomerates. Where mudstones are incorporated within the vertical sections and associated with ridge-scale erosional surfaces, thicknesses range from pinched out to 0.60 m. Mudstone thickness can vary over short, meters-scale distances due to erosion from above, but the erosional surfaces these mudstones were deposited on top of are laterally persistent at the ridge scale. These persistent erosional surfaces are used to define and separate individual channel-belt stories (Fig. 2.5A and B and 2.6A and B; Friend et al., 1979). Any given vertical section exposes 1-4 stacked stories which locally vary in thickness from 0.10 m to 8.60 m, with a mean of $3.10 \text{ m} \pm 0.22 \text{ m}$ (the calculated standard error of the mean), median of $2.80 \text{ m} \pm 0.27 \text{ m}$ (the calculated standard error of the median) and σ of $2.03 \text{ m} \pm 0.15 \text{ m}$ (the calculated standard error of the standard deviation; $n = 89$; Fig. 2.6C). These story-bounding surfaces

are also exposed along the top surfaces of the ridges. Five of these surfaces have been mapped across the western ridge, and four have been mapped across the eastern ridge (Fig. 2.5C).

2.3.2 Sedimentary structures and architecture

The most common sedimentary structures preserved in planview and vertical exposures of the Cedar Mountain Formation ridges are trough cross sets (Fig. 2.7A to D) with median grain sizes ranging from upper-fine sand to medium pebbles (Fig. 2.8A to C). The mean thickness of these sets is $0.12 \text{ m} \pm 0.005 \text{ m}$, with a standard deviation of $0.09 \text{ m} \pm 0.003 \text{ m}$, and a coefficient of variation of 0.79 ± 0.04 ($c_v = \sigma/\text{mean}$, with propagated errors; $n = 350$). Along the top ridge surfaces where these structures are exposed and mapped in planview (Fig. 2.9), the dominant dip direction of these sets was clearly identified and representative of the associated bedform's migration direction. The polygons outlining these planform exposed sets ($n = 1,071$) sum to a total area of $5,019 \text{ m}^2$. Of the 1,071 sets mapped in planform, 269 were identified as conglomerate, representing 25.1% of sets and 26.5% (1330 m^2) of total set area. The remaining 802 sets were identified as sandstone, representing 74.9% of sets and 73.5% (3689 m^2) of total set area. Larger scale thicker compound cross-sets ($n = 12$), with a mean of $1.28 \text{ m} \pm 0.05 \text{ m}$ and a σ of $0.19 \text{ m} \pm 0.04 \text{ m}$ measured at preserved rollovers, and are also exposed in planview (Fig. 2.10A-D). The locations of planview measurements of both types of sedimentary structures are shown in Figure 2.11. The summed planform exposure area of these sets ($n = 103$) is 520

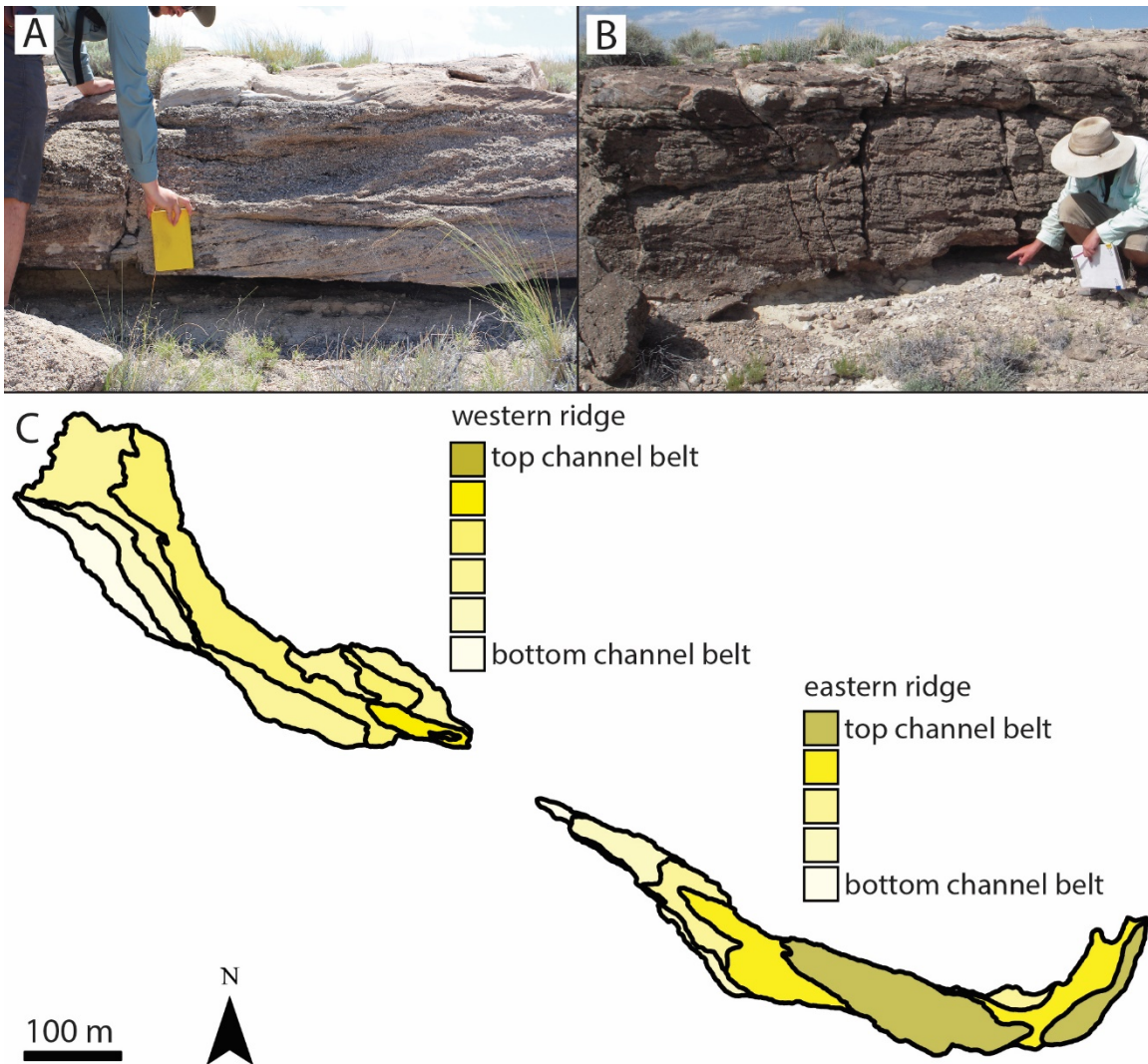


Figure 2.5 (A-B) Beneath the yellow notebook (A) and at where the finger is point (B) are erosional surfaces associated with friable, recessed mudstones separating coarse-grained, cross-bedded packages. These erosional surfaces are interpreted to represent the contacts between stacked channel belts. Not all mudstones are associated with these surfaces. (C) Geologic maps showing the stacking patterns of channel-belts exposed at the surface of both ridges. Darker yellows indicate higher stratigraphic positions. There is no attempt to correlate individual channel belts between ridges.

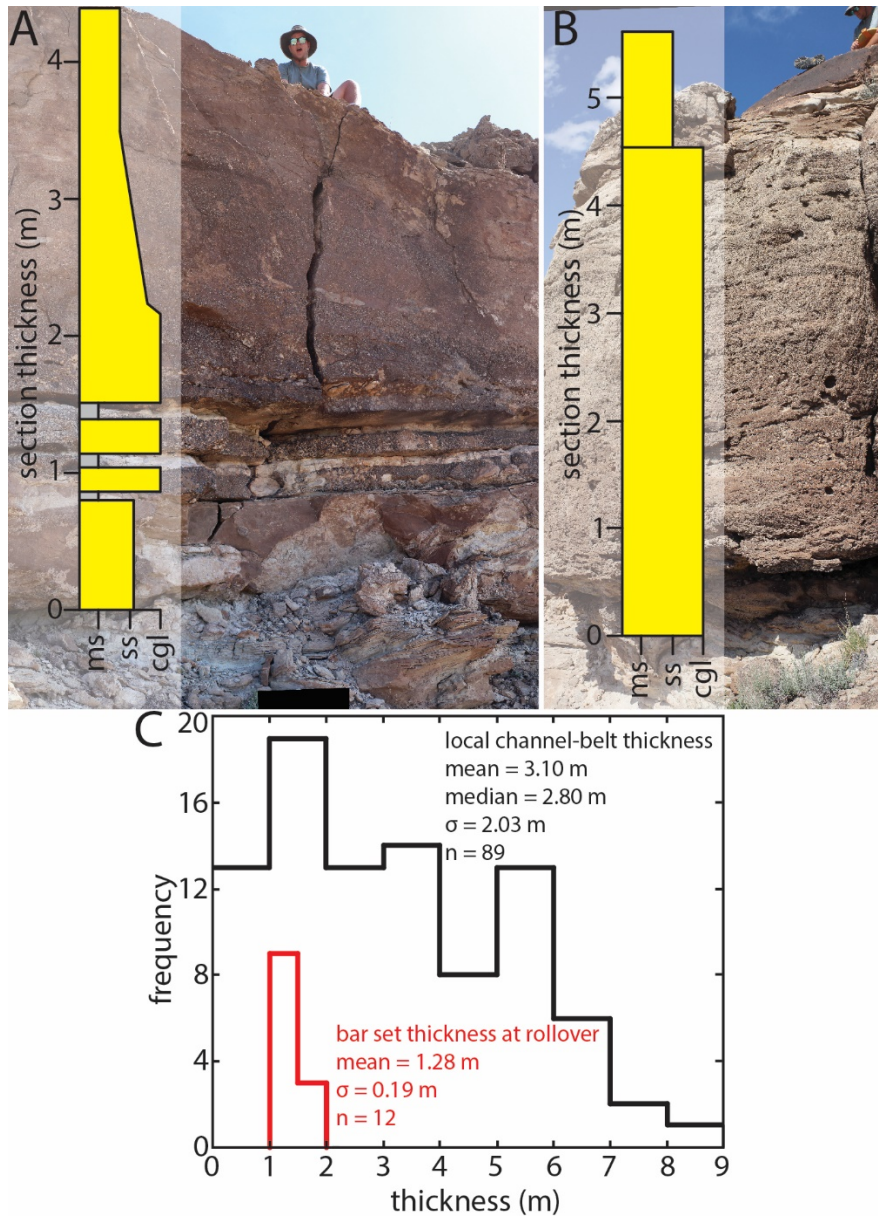


Figure 2.6 (A) Vertical section showing story-bounding surfaces and associated mudstones. Stories in this section are of average to below-average thickness. (B) Two stories bounded by an erosional surface with no associated mudstone. The bottom story is above average thickness. (C) Histogram of local channel-belt (story) thicknesses measured from vertical sections, and the mean thickness of a bar set at the rollover (red line), which is used as a proxy for channel depth. The difference between channel depth and channel-belt thickness is due to aggradation of the channel bed.

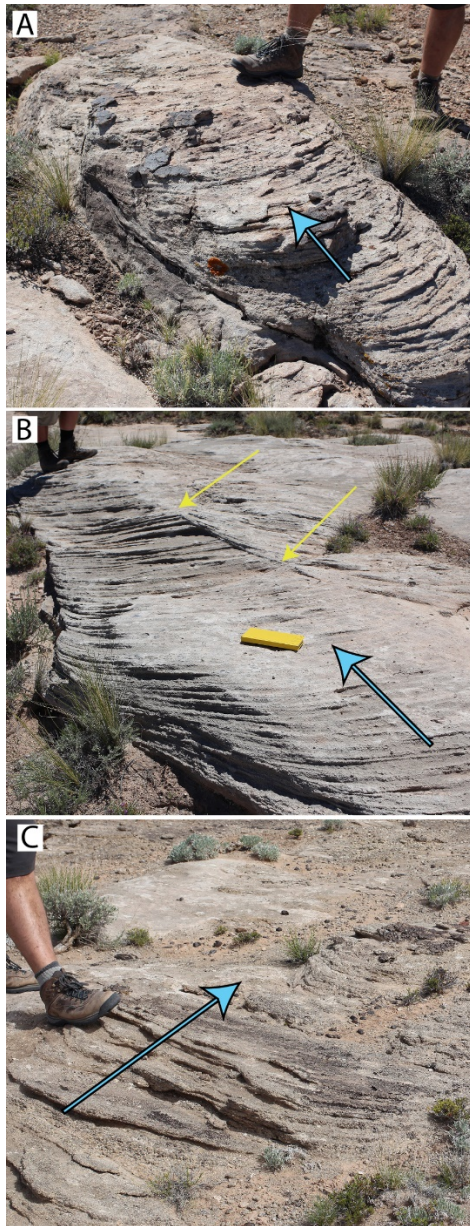


Figure 2.7 Photos of cross strata exposed in planview along upper ridge surfaces. Teal arrows show the mean dip directions of cross strata. (A) This 3-D outcrop of a sandstone set shows the relationship between planform-exposed cross strata and vertically exposed cross strata. Boots for scale. (B) A 3-D exposure of a sandstone set. Yellow arrows point to the bounding surface separating two sets. This sort of amalgamation is common. Yellow field book for scale. (C) A conglomerate set showing minimal planform curvature. Boot for scale.

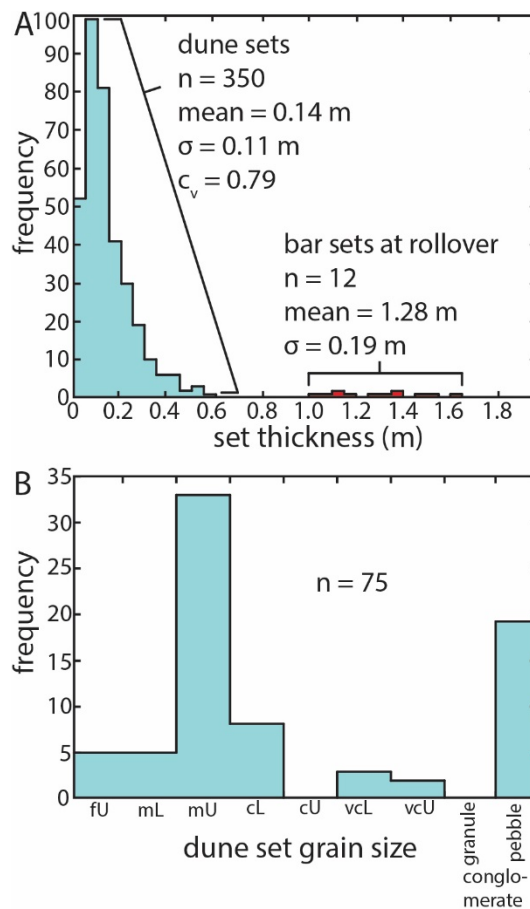


Figure 2.8 (A) Teal histogram shows the distribution of the entire population of dune cross-set thicknesses, with statistical moments and the coefficient of variation (c_v). The distribution of bar set thicknesses at the rollover is shown in the red histogram. When measuring bar sets at the rollover, there is a break in the distribution of dune sets and bar sets. (B) Distribution of grain sizes of dune cross-sets. Measurements made in the field with a grain size card and hand lens.

m^2 , or covering 10.3% the planform area compared to trough cross-sets. Within individual channel belt stories, shingled trough cross-sets record transport up and down larger-scale topography (Fig. 2.12A-D).

Four arrangements of cross beds were observed. Type A featured a thick basal set of compound strata scoured along its top by an upstream-dipping surface, and overlain by

a thinner coset composed of smaller cross beds with a mean thickness and standard deviation of $0.12 \text{ m} \pm 0.01 \text{ m}$ and $0.07 \text{ m} \pm 0.01 \text{ m}$ (Fig. 2.13). The upstream dips of the scour surface range from 5° - 13° (mean = 7° , n = 6). In this case, orientation of small cross beds roughly parallel the dip direction of the larger cross beds. Type B featured a thick basal set of compound cross-sets that change both dip and thickness in the downstream direction (Fig. 2.14). Individual cross beds thickened by as much as 300% over the course of 1.5 meters in the downstream direction (0.08 m to 0.23 m, 0.07 m to 0.23 m, and 0.06 m to 0.19 m). Correspondingly, the bounding surfaces separating these cross beds shallow downstream from as steep as 26° to as shallow as 5° , and the upper bounding surface transitions from being markedly erosional to conformable (Fig. 2.14). Similar to type A, the smaller cross beds roughly parallel the dip direction of the larger cross beds. The mean thickness and standard deviation of these sets at shallowly dipping sections was $0.13 \text{ m} \pm 0.01 \text{ m}$, and $0.08 \text{ m} \pm 0.01 \text{ m}$. Type C was also composed of compound strata, but in these cases the dip direction of the smaller foresets were roughly transverse to the dip direction of the larger cross beds (Fig. 2.10D). Type C sets were identified in planview exposures, so set thickness measurements were not made.

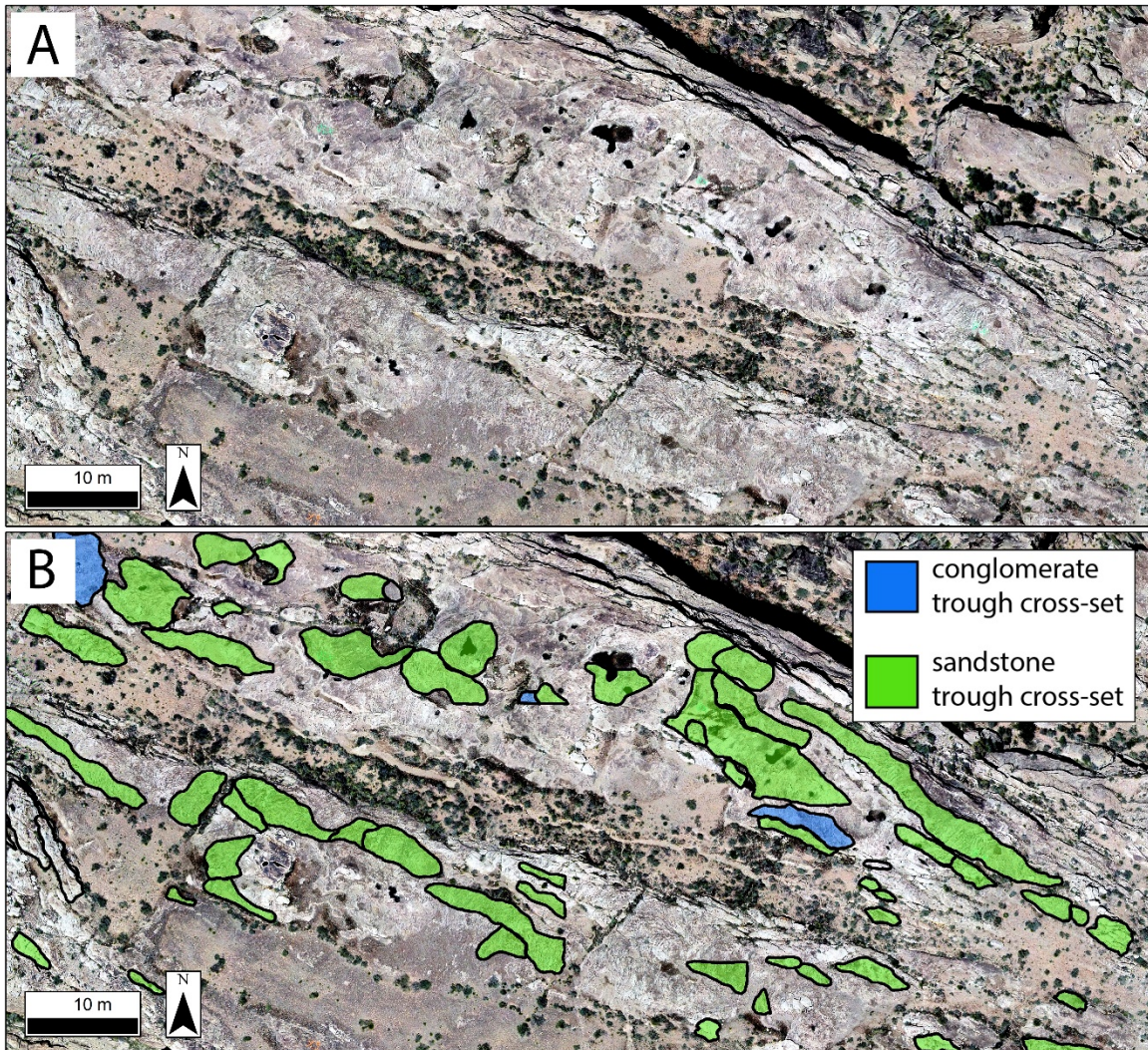


Figure 2.9 (A) Example of unmanned aerial vehicle photomosaics used as field base maps. (B) Digitized field map showing planform-exposed sets of cross strata outlined and filled in with green (sandstone) or blue (pebble conglomerate).

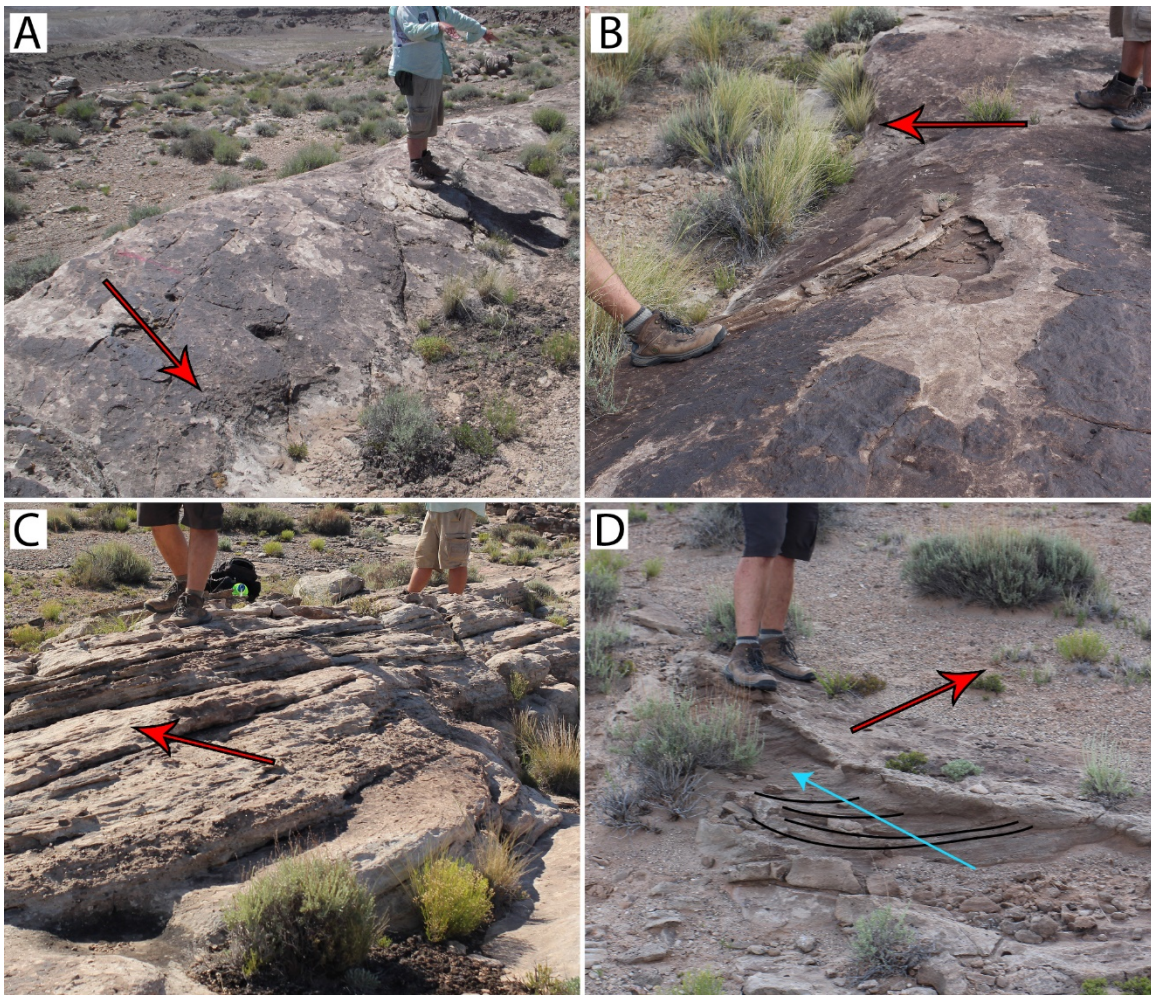


Figure 2.10 Examples of larger-scale accretion strata in the field. Red arrows show the dip direction of the strata in each panel. (A) A typical example exposed for several meters. A lack of exposed bounding surfaces on this topographic surface suggests the topography itself represents a bounding surface. (B) Beneath the arrow, erosion exposes internal stratification parallel to the surface. (C) A 3-D outcrop of larger-scale dipping strata composed of smaller-scale stratification exposed by erosion. (D) Compound cross strata with a larger-scale accretion surface (red arrow) dipping obliquely to a smaller-scale dune set (teal arrow). A few dune cross strata are mapped in black lines.

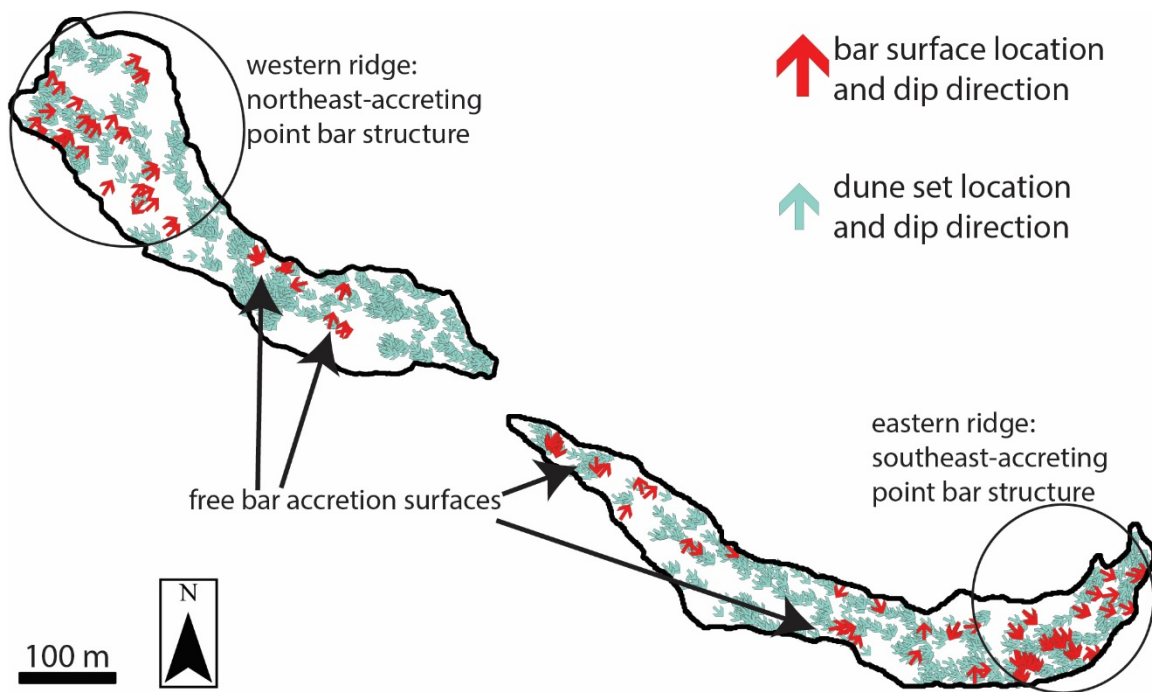


Figure 2.11 Planform maps outlining the top surfaces of both studied ridges. Teal arrows show the locations of paleotransport measurements and point towards the measured direction. Red arrows show dip directions of large-scale dipping strata. Two locations with clusters of similarly-dipping bar accretion surfaces following ridge curvature are interpreted to represent point bars. The northeast-accreting point bar structure of the western ridge corresponds with a larger-scale ridge curvature beyond the extent of the study area (Fig. 2.1C). Bar accretion surfaces not clearly associated with a point bar are interpreted as free-bar accretion surfaces.

Strata composing Types A, B, and C are sandstones. Type D featured no compound cross-stratification, and bounding surfaces were sub-horizontal or show local variable curvature associated with trough geometry. Type D strata featured pebble conglomerates and a $\sim 90^\circ$ scatter of transport directions, apparent by the juxtaposition of trough and dip-normal exposures (Fig. 2.15). The mean thickness and σ of type D sets was $0.19 \text{ m} \pm 0.02 \text{ m}$ and $14.7 \text{ m} \pm 0.02 \text{ m}$, and sections contain up to ten stacked sets.

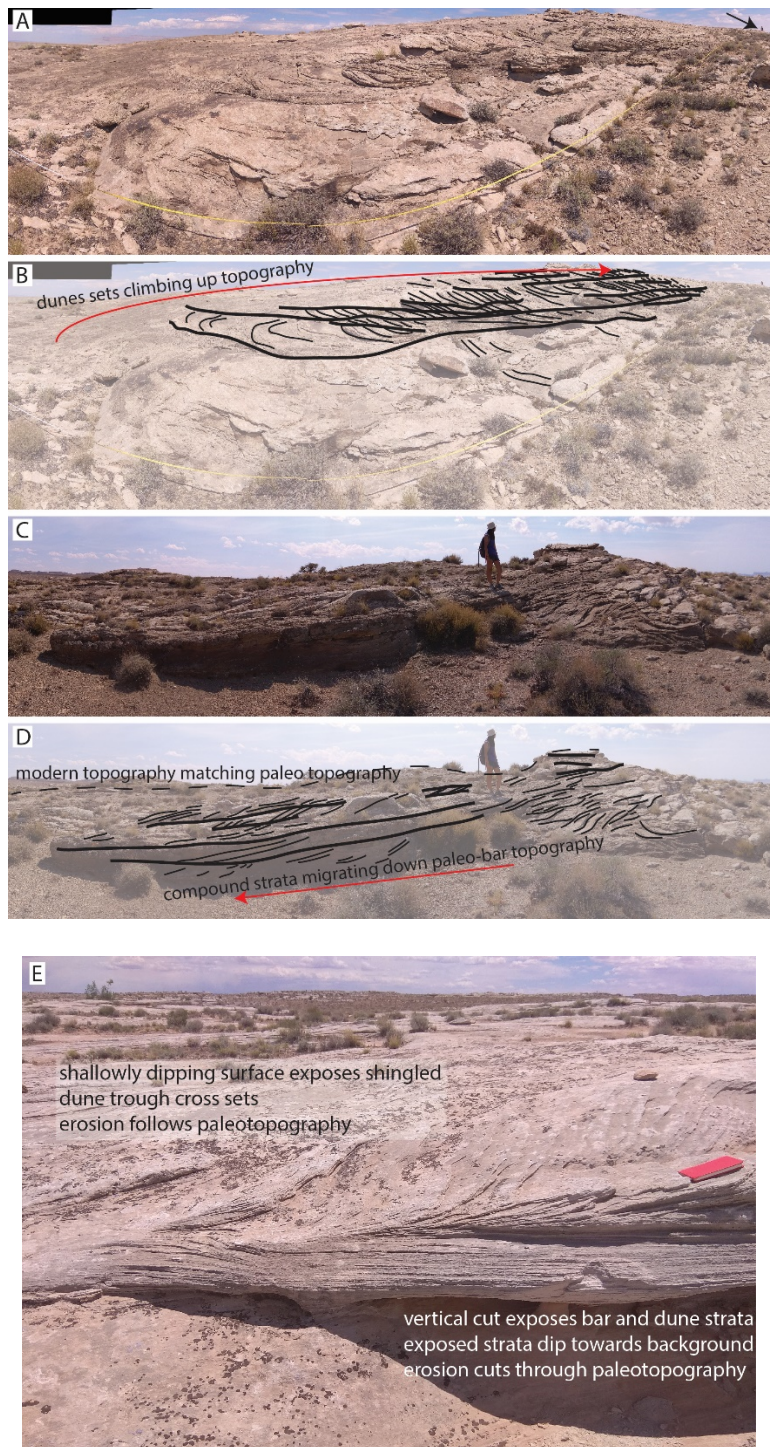


Figure 2.12

Figure 2.12 The preservation of bar topography on upper-ridge surfaces. (A) Fisheye view of a sandstone mound rising towards the downstream direction (left to right), with a surface defined by shingled cross-sets climbing with topography. Interpreted as the stoss surface of a downstream-migrating barform. Tape measure for scale in foreground, arrow pointing to person in background. (B) Interpretation of panel A. (C) Downstream end of sandstone mound featuring cross sets and topography falling in the downstream direction. Interpreted as the lee slope of a downstream-migrating barform. Person for scale. (D) Interpretation of panel C. (E) Preserved point bar topography in the nearby Morrison Formation (Fig. 2.1B). In the foreground, the vertical exposure cuts through dune and bar stratigraphy, and clearly does not follow the paleotopography of the bar. Contrast this with the steeper surface just beyond the vertical cut filling most of the background, which exposes shingled sets of planview-exposed dune cross sets. This surface approximates the original topography of the bar.

2.3.3 Transport anomalies

Maps of transport anomalies (Θ_{TA}) for the Cedar Mountain Formation and North Loup River are presented in Fig. 2.16A to C. The associated Θ_{TA} histograms and statistical moments for these systems and the Trinity River are presented in Figure 2.17A to D. Significantly, all datasets have mean values ranging between -12 and +6 degrees, and standard deviations ranging from 25° to 35°. In the North Loup, anomalies were clearly connected to local bar topography, but measurements approach the reach mean when assembled over a downstream distance of ~3 bar lengths (Figs. 2.16C and 2.18A to C). In the Trinity, and meandering rivers generally, both the magnitude of the mean and standard deviation of the transport anomalies are the smallest (Fig. 2.17D). Transport anomalies that are observed are largely due to the deflection of flow obliquely down point bar surfaces (Dietrich and Smith, 1984). In the Cedar Mountain, areas with concentrated high anomalies were found to be located at ridge bends (Fig. 2.16A to B).

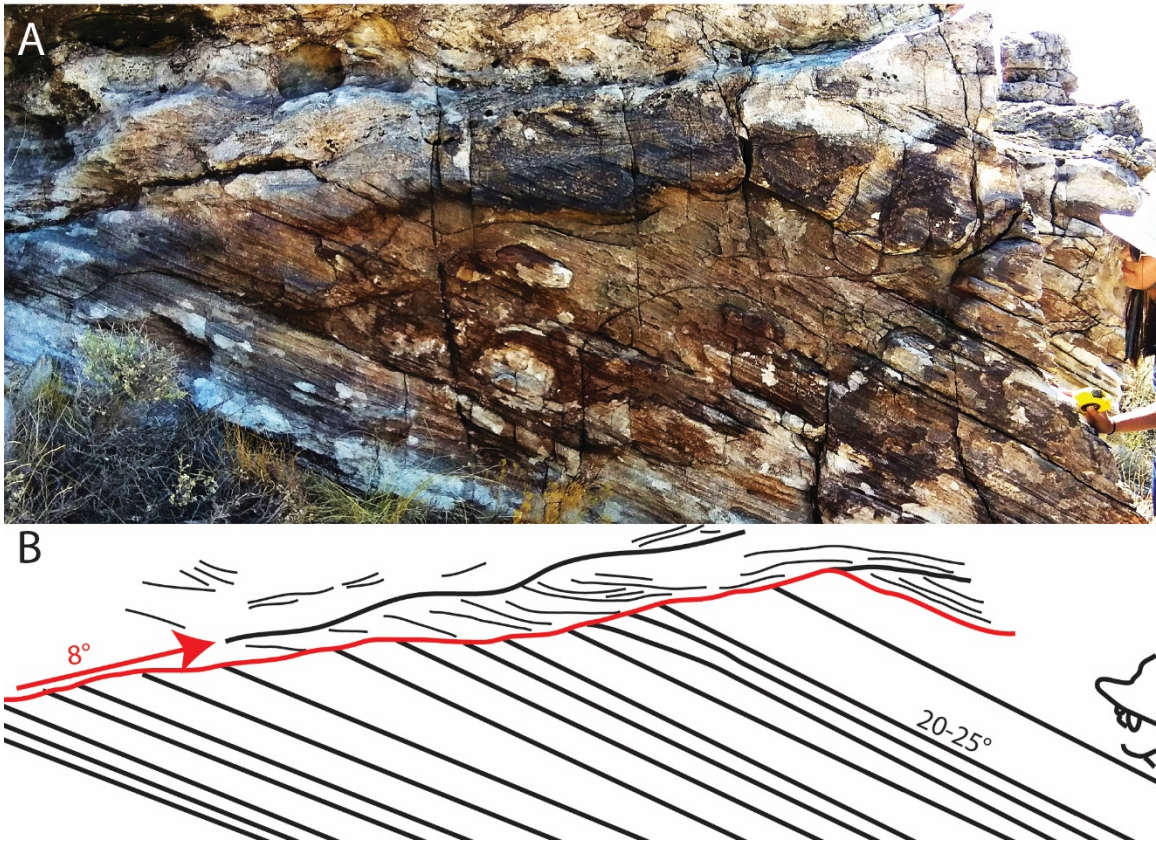


Figure 2.13 Cross-sectional view of preserved strata from the stoss side of a bar, with an interpreted transition to the lee side. Flow was from left to right. In the sketch, the truncation surface separating lee-side (underneath) from stoss-side (above) strata is marked as a red line. This line is interpreted to preserve the upstream-dipping, stoss-side slope for the bar of 8° . Sets of dune strata are marked by thick black lines and dune cross strata by thinner black lines. Deposition on the stoss-side of the bar is best shown by the upward climbing dune sets at the right-side side of the panel. Beneath these stoss-side strata are steeply dipping beds recording the prior lee face of the bar. At the left-hand side of the exposure it is particularly clear that the bar form is composed of compound strata in which the bar shape evolved through deposition of dune cross-beds. At this same location the truncation surface separating stoss and lee strata becomes conformable. The package of thick dune sets at this position is interpreted to be associated with higher sedimentation rates on the lee face of the bar. The observed spatial change in the dip angles of dune sets and the truncation surface document change in bar shape through time.

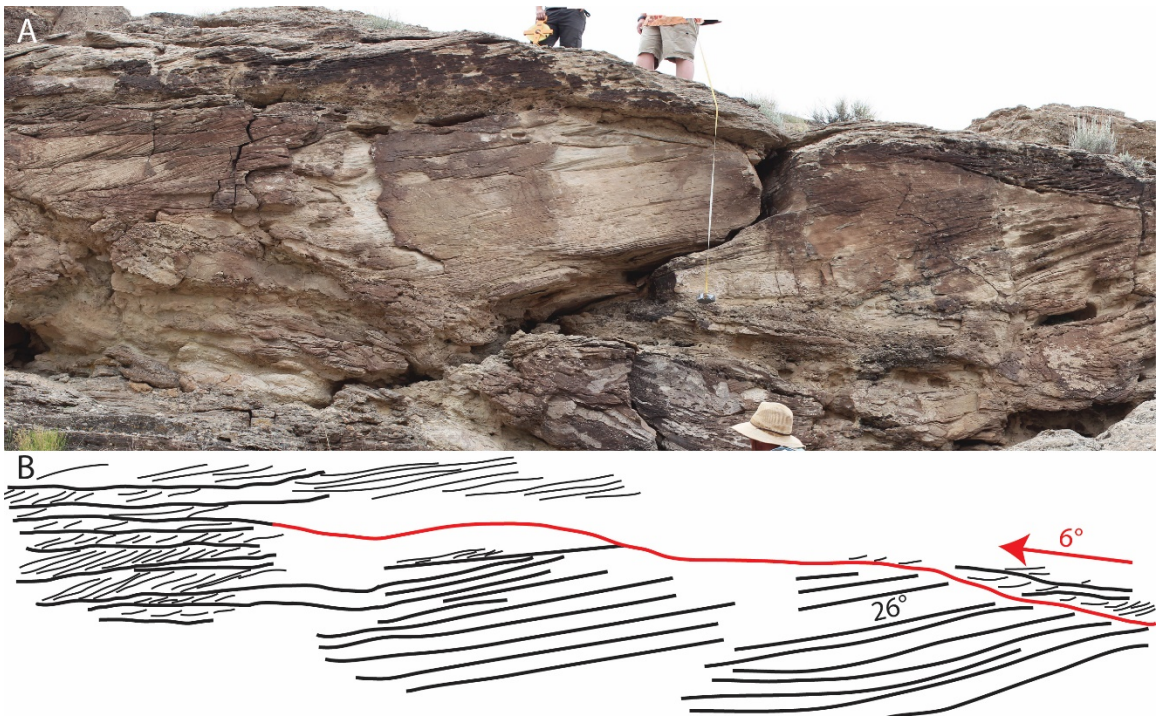


Figure 2.14 Cross-sectional view of preserved strata from the lee and stoss sides of a bar form. Flow was from right to left. In the sketch, the truncation surface separating lee-side (underneath) from stoss-side (above) strata is marked as a red line. This line is interpreted to preserve the upstream-dipping, stoss-side slope for the bar of 6° . Sets of dune strata are marked by thick black lines and dune cross strata by thinner black lines. Deposition on the stoss-side of the bar is best shown by the upward climbing dune sets at the right-side side of the panel. Beneath these stoss-side strata are steeply dipping beds recording the prior lee face of the bar. At the left-hand side of the exposure it is particularly clear that the bar form is composed of compound strata in which the bar shape evolved through deposition of dune cross-beds. At this same location the truncation surface separating stoss and lee strata becomes conformable. The package of thick dune sets at this position is interpreted to be associated with higher sedimentation rates on the lee face of the bar. The observed spatial change in the dip angles of dune sets and the truncation surface document change in bar shape through time.

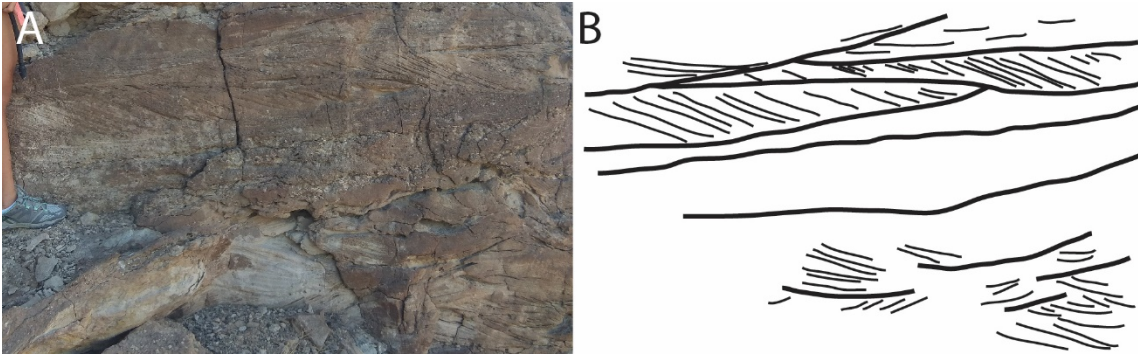


Figure 2.15 Cross-sectional view of strata featuring a $\pm 90^\circ$ spread in transport direction, conglomerates, and a lack of bar architecture. This type of architecture is interpreted as a thalweg due to the coarser grains driven by higher velocity flow, and a larger spread in transport driven by changes in steering due to bar growth. The sketch shows bounding surfaces and cross strata.

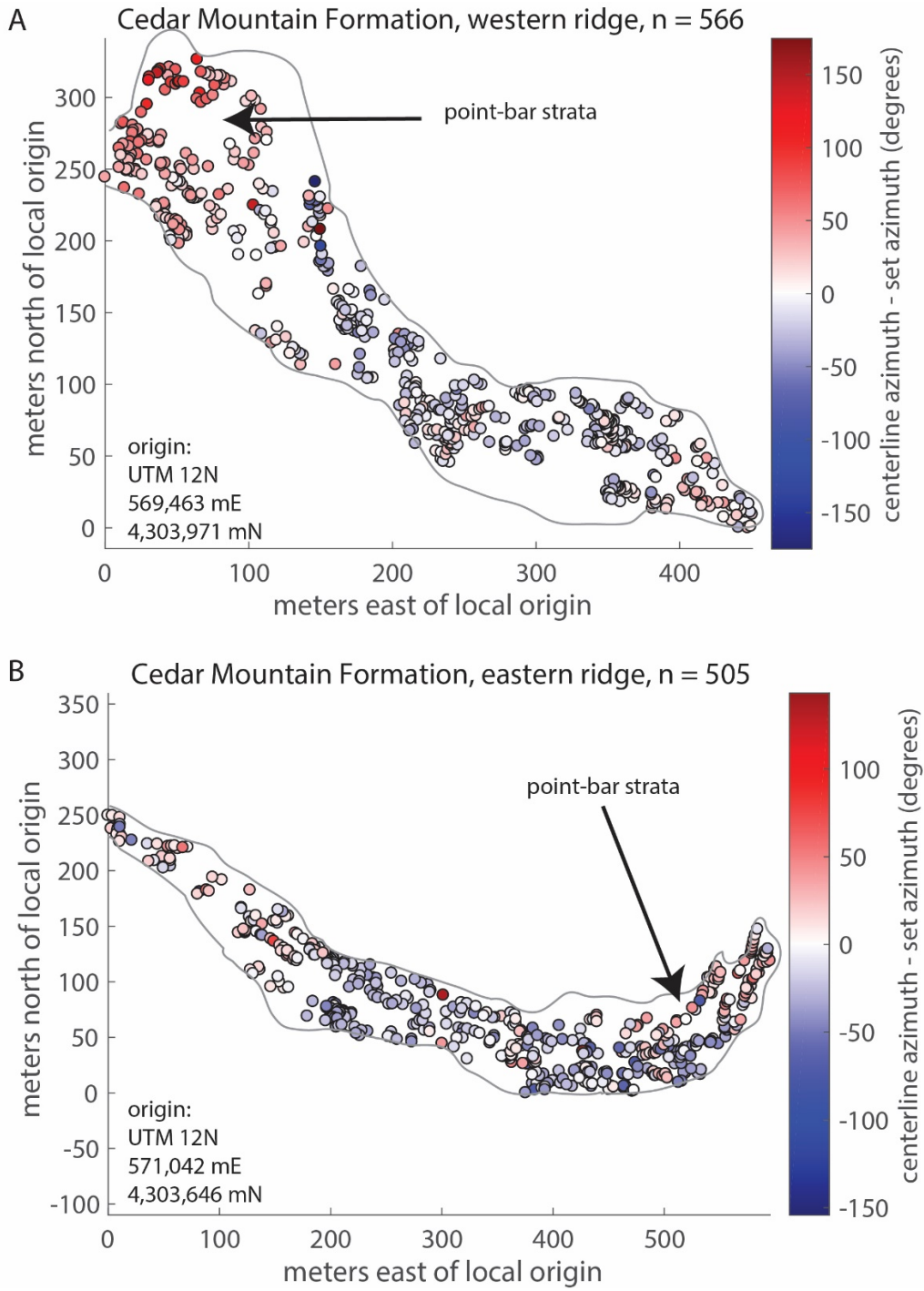


Figure 2.16A-B

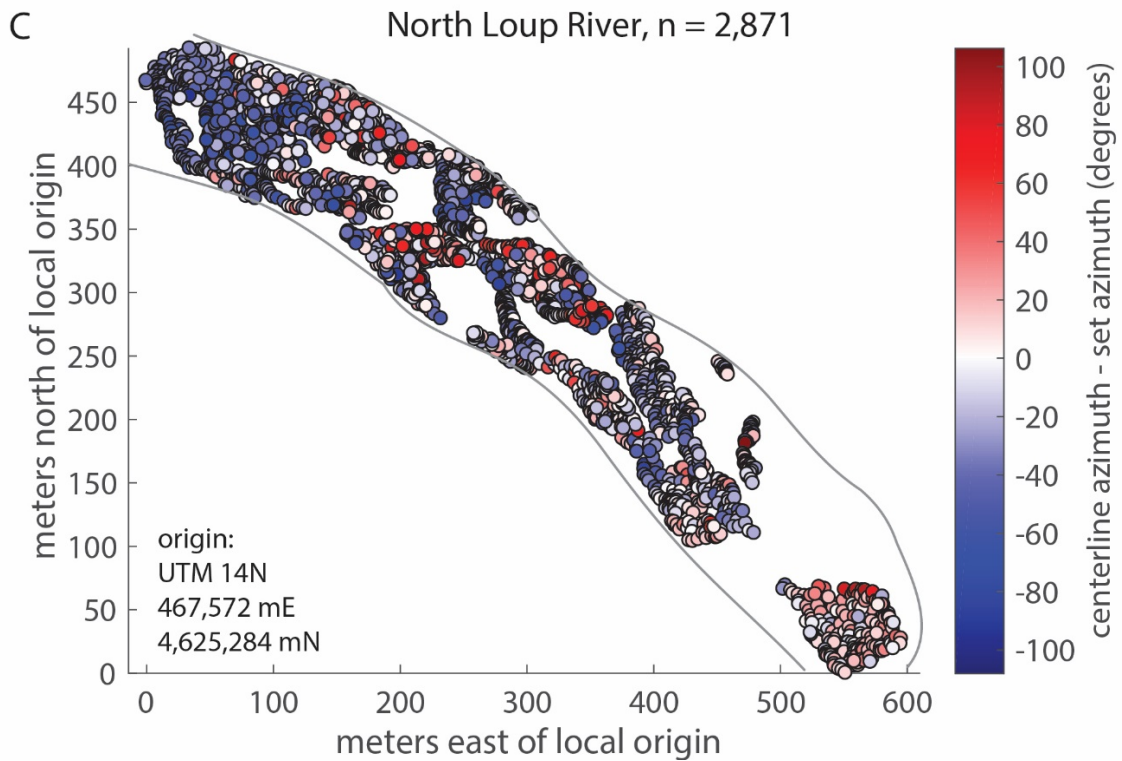


Figure 2.16 Transport anomaly maps of the western ridge of the Cedar Mountain Formation (A), the eastern ridge (B), and the North Loup River (C). X and Y coordinates are relative to a different local datum in each map, shown in the bottom left corner of each panel. Circles show the location of paleotransport or modern transport direction measurements. The color at each point represents the paleotransport or transport anomaly (Fig. 2.3A-B). Gray lines represent ridge outlines and the banks of the North Loup River. Black arrows in panels A and B point to regions recording point bar accretion, and are associated with relatively high anomaly values, particularly in the western ridge (Figs. 2.1C and 2.11).

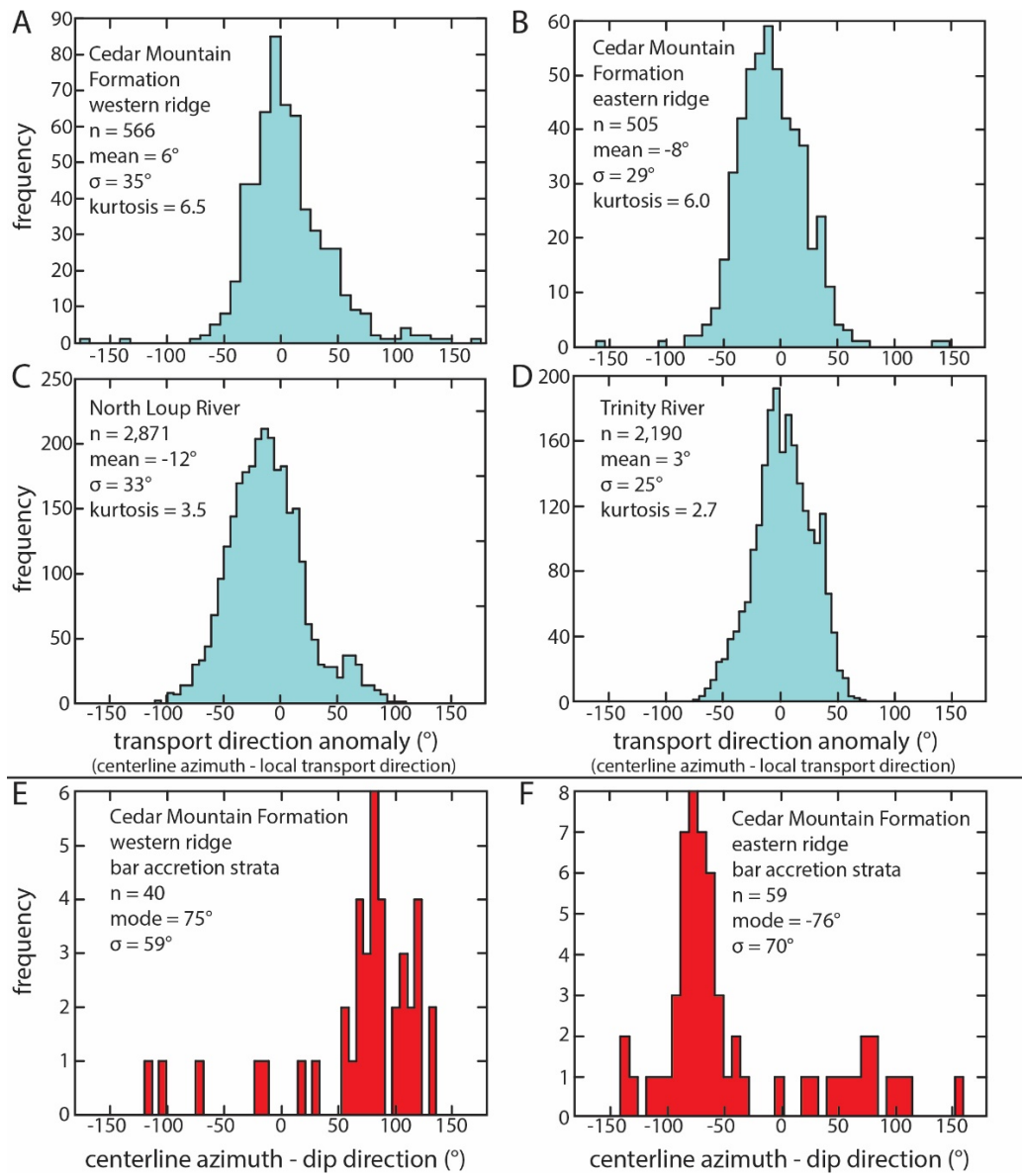


Figure 2.17 Histograms showing the distribution of paleotransport/transport anomalies of the western (A) and eastern (B) ridges of the Cedar Mountain Formation, and the modern North Loup River (C) and Trinity River (D). The number of measurements, mean, and standard deviation are reported in each panel. Note the similarity in mean and standard deviation between the ancient and modern datasets. Histograms (D) and (E) show the difference between dip directions of bar accretion strata exposed along the upper surfaces of ridges and the centerline. Both histograms show a wide distribution of values with peaks approaching perpendicular to the centerline trend.

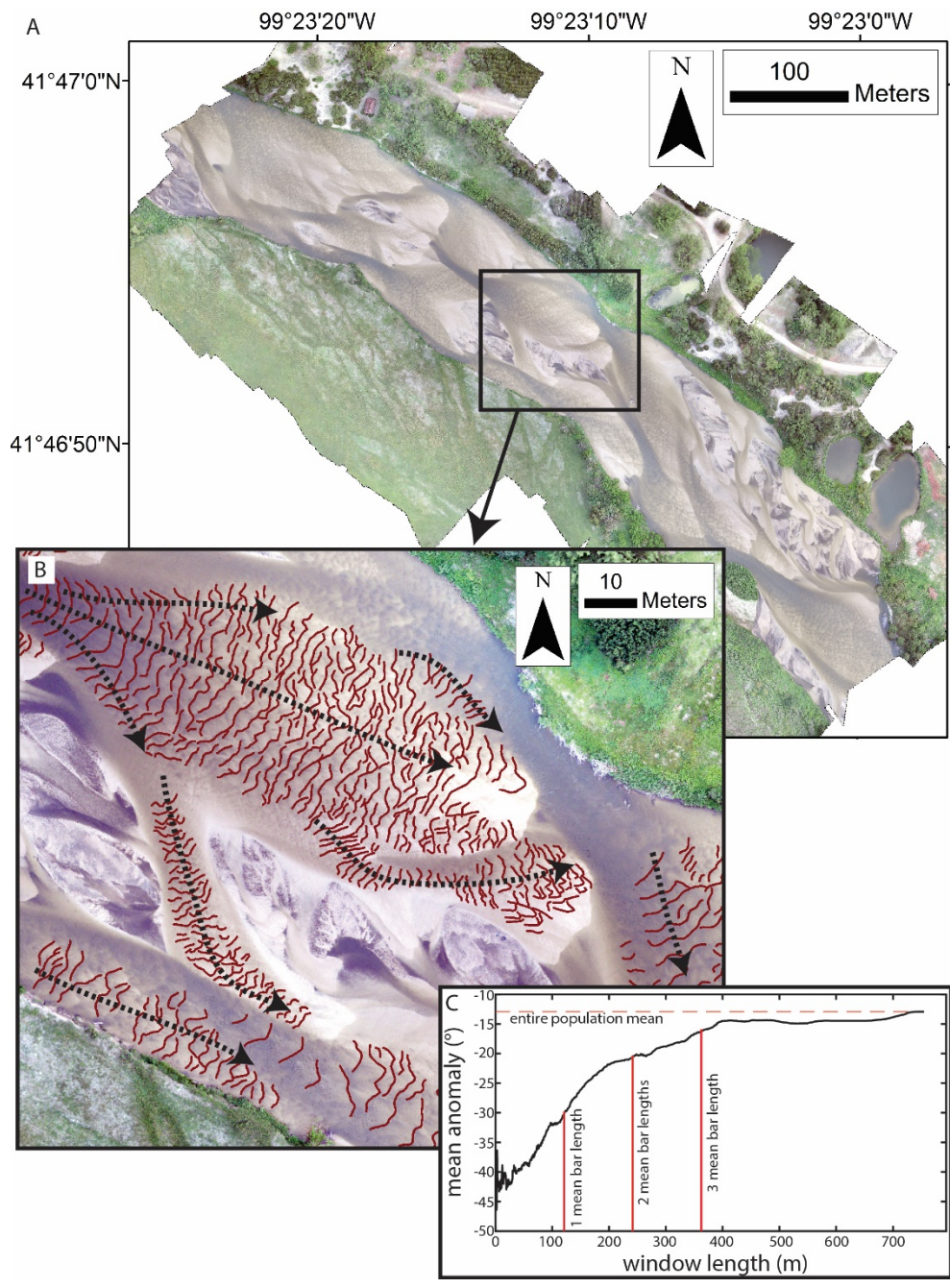


Figure 2.18

Figure 2.18 (A) Drone photomosaic of the North Loup River near Taylor, Nebraska, USA (Swanson et al., 2018). Brighter tan colors within the channel are subaqueous and represent higher portions of downstream-migrating bars beneath shallow water. Darker reaches of the channel represent deeper water. Mixed white and black areas with no crestlines mapped are subaerially exposed bar tops that are not currently undergoing fluvial transport. The location of panel B is shown in the black box. (B) Zoom in showing dune crestlines (short red lines) interpreted as perpendicular to dune transport direction. Black dashed arrows show general trends in local transport directions due to the steering of flow around bars. (C) Window length vs. the mean transport anomaly within the window. As the window length approaches that of the ~ 3 barforms, the sampled mean approaches the mean of the entire dataset. Changes in curvature of this line happen near multiples of mean bar length (red vertical lines), supporting topographic steering as the source of the transport anomaly.

2.4 DISCUSSION

2.4.1 Dune, bar, belt, and overbank strata

A distinction is drawn between cross sets on either side of the break in scale shown in Figure 2.8A. The thinner-bedded trough cross strata (Fig. 2.7A to C) are interpreted as forming via the migration of 3-D dunes with variably deep troughs (Rubin, 1987). In planform and vertical sections, these are clearly distinct from larger scale dipping strata (Fig. 2.10A to D), which do not show the same bounding-surface curvature and, significantly, feature cross strata defined by compound cross-sets (Figs. 2.10D and 2.14A and B). These larger scale strata are interpreted as accretionary river-bar deposits (Edwards et al., 1983). The population of dip direction vs. centerline trend anomalies for the bar strata feature a larger spread of values and modes situated far from zero (compare Fig. 2.17A to D against Fig. 2.17E to F). The range of values suggests the formative bar types included point bars with primarily cross-stream accreting surfaces (Fig. 2.10D), and free bars which can feature cross-stream-, downstream-, and upstream-dipping accretion surfaces (Skelly et al., 2003). Point bar structures are best observed at the ridge scale, where clusters of bar surfaces dip towards the convex sides of ridge bends (Fig. 2.11; note that the western-most point bar strata define a convex-north bend, Fig. 2.1C). Together, these dune and bar scale cross strata are interpreted as deposits filling river channels during episodes of active transport within that channel reach. The mudstones associated with ridge-scale erosional surfaces are interpreted to represent sedimentation during periods of channel abandonment, which would be expected in a system that experienced multiple avulsions (Mohrig et al., 2000; Jones and Hajek, 2007; Cuevas Martínez et al., 2010), although not every

reoccupation of a channel during avulsion preserves a mudstone layer connected to the channel-belt boundary.

The four cross-stratal types observed in the Cedar Mountain ridges document the interaction of the ancient dunes and bars. Type A architectures are characteristic of free bars, and possess a bar-scale bounding surface, shown in red in Figure 2.13, separating lee strata below from deposits of the stoss surface above. As such, this bounding surface preserves the characteristic dip of the stoss side of the bar form. At first glance, it might seem surprising to accumulate a coset of stoss-side deposits, but theory (Paola and Borgman, 1991) and a recent morphodynamic bedform model (Swanson et al., 2019) show that set stacking can occur even under conditions of net bypass and net erosion because of variability in dune scour depths. Type B architectures highlight change due to migration of free bars (Fig. 2.14). The steepest 26° cross strata represent lee construction most perpendicular to the average transport direction. The observed shallowing of bounding-surface dips and thickening of sets in the downstream direction records the planform deformation of the bar crest over time, where steep downstream-accreting surfaces gradually become more laterally accreting. As evident from the compound nature of these sets (Fig. 2.14), this bar growth is driven by dune accretion in front of the bar. At the two locations where A and B type architectures are adjacent (Figs. 2.13 and 2.14), the transition of the stoss scour surface to the conformable bounding surface of a cross-stratum represents the delivery of sediment mined from the bar stoss up and over the crest of the bar, and onto the bar lee. Taken together, these two architectures preserve the processes associated with bar migration via the mining and delivery of sediment by a surface veneer of smaller dunes

compound to a larger free bar. These are the ‘form sets’ of Reesink et al. (2015), but observed in bar strata rather than dune strata. One lateral section shows the stacking of lee strata on stoss strata, recording the aggradation and migration of a bar (Fig. 2.19). The type C compound strata define bar growth at an oblique angle to the net transport direction, and define the lateral migration of a bank-attached bar form (Fig. 2.10D). The coarser, non-compound type D architectures are interpreted as thalweg deposits (Fig. 2.15). Together, these four architectural types describe the construction of channel-bottom topography within individual channel belts via the migration and growth of dunes (both on bars and in the thalweg), free bars, and point bars.

2.4.2 Channel bed topography

Preserved bar form topography is interpreted to record the moment of channel abandonment (Fig. 2.12A to D). Two lines of evidence support this and, significantly, these lines of evidence are true for the Cedar Mountain Formation, as well as nearby outcrop of the Jurassic Morrison Formation (Fig. 2.12E; location shown in Fig. 2.1B). In both cross section and map view, the compound relationship between dune and bar strata informs us that entire bar forms are preserved (Figs. 2.12, 2.13, 2.14, and 2.19). The stoss-positioned dune sets are restricted to a surface veneer composing less than the upper 25% of the bar, with the remainder composed of steeply-dipping bar-scale strata. If deflation of ridge surfaces commonly broke through the surface veneer of dune sets, large bar scale strata would constitute a greater percentage of sedimentary structures exposed on ridge surfaces. The preservation of the river-bottom topography at the time of avulsion is interpreted to be

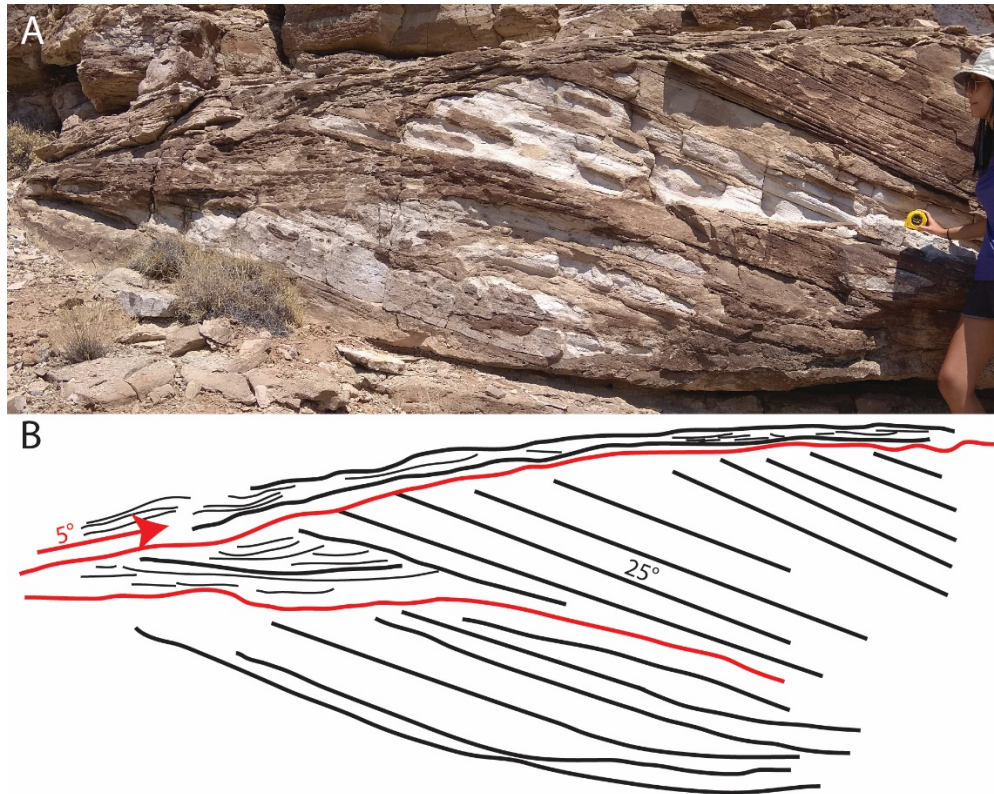


Figure 2.19 Cross-sectional view showing the internal structure of a barform. Flow was from left to right. In the sketch, the bottom-most red line marks a surface at which lower bar-scale cross strata are truncated. This surface becomes conformable with the bar strata downstream, and features a veneer of smaller-scale sets above it. This arrangement is consistent with a bar stoss-to-lee transition. The upper-most red line defines a 5° upstream-dipping surface truncating 25° downstream dipping bar-scale strata. Above this surface are two dune-scale sets. The architecture arranged around this red surface is consistent with a bar stoss environment. From bottom to top, the transition from stoss-to-lee architecture to lee architecture, all within the same barform, records the forward migration and aggradation of the barform.

the consequence of a relatively rapid channel abandonment. The barform/bedform preservation in the Cedar Mountain and Morrison Formations (Fig. 2.1B) speaks to a potential universality of the preservation of bed topography at the tops of individual channel belts.

2.4.3 Channel planform geometry

The near zero means, the similarity of the standard deviations measured in the ancient and the modern, and the high kurtosis of the Cedar Mountain Formation paleo-transport anomaly measurements are interpreted to represent the preservation of the formative river centerlines in a reliable way (Fig. 2.17A to D). Regions of the channel belts showing concentrations of high transport anomaly measurements are associated with point bar lateral accretion surfaces (Figs. 2.1C, 2.11, and 2.16A to B), supporting the hypothesis that lateral point bar migration is a cause of high anomaly measurements (Fig. 2.4B). However, these regions do not represent a majority of the ridge area. The studied ridges are composed of several vertically-stacked channel-fills. The preservation of the formative river channel centerlines through multiple re-occupations of the channel is expected in fluvial settings with high rates of vertical aggradation within the channel relative to lateral migration rates (Gibling, 2006; Jerolmack and Mohrig, 2007). As a result, there is a general lack of centerline distortion, even though the ridge represents a channel-belt complex. An interesting corollary is that the sinuous planform of the lowest river must have been at least partially inherited from the antecedent surface (e.g., Lazarus and Constantine, 2013), as the point bars seem to have been forced by pre-existing curvature rather than driving the formation of channel sinuosity.

2.4.4 Channel-belt thickness

Because avulsions are likely to occur when a channel bed has aggraded, the thickness of a preserved channel belt, on average, is posited to equal paleo-channel depth plus an aggradational component. Mohrig et al. (2000) report an average superelevation of

0.61 times flow depth before avulsion occurs from the Guadalupe-Matarranya ancient fluvial system in Spain. The thickness of a free bar deposit from rollover to bottom is assumed to be a measure of local channel depth (Mohrig et al., 2000). Bar measurements reported in Fig. 2.8A suggest an overall, mean channel depth of 1.28 ± 0.05 m. The median belt thickness of $2.80 \text{ m} \pm 0.27 \text{ m}$ (Fig. 2.6C) indicates that, on average, a channel aggraded to a height of 2.19 ± 0.23 times its original depth before avulsing. This is a slightly higher value than the dataset of Mohrig et al. (2000). In their Table 2, the sum of the incision depth and superelevation is equal to the belt thickness measurements presented here. Dividing their belt thickness measurements by local channel depth yields an average total aggradation before avulsion of 1.84 times channel depth. Overall, this suggests the ancient Cedar Mountain fluvial system was able to support more channel bed aggradation before avulsion, suggesting a higher ratio of floodplain aggradation rate to channel bed aggradation rate than in the Guadalupe-Matarranya system (Mohrig, 2000).

2.4.5 Reconstructing river-bed kinematics

2.4.5.1 Dune motion on bars and in the thalweg

Analysis of Paola and Borgman (1991) shows that bedforms with gamma-distributed heights create a predictable exponential distribution of set thicknesses in cases of no net aggradation. Bridge and Best (1997) and Jerolmack and Mohrig (2005) emphasize the importance of bed aggradation as a control on the distribution of set thickness, showing that increased aggradation rates decrease the relative control of variable scour depth on set thickness. Jerolmack and Mohrig (2005) showed that the coefficient of variation (c_v) of set

thicknesses, which is equal to the standard deviation of the population divided by its mean, decreases from a value of 0.88 in the case of no aggradation, to values approaching the c_v of the formative bedform heights with significant bed aggradation. Coupled with this change in c_v is a gradual move from the predicted exponential distribution of set thicknesses, to a gamma distribution mirroring the distribution of the formative bedforms. Significantly, this analysis has been shown general enough to apply to ancient fluvial (Jerolmack and Mohrig, 2005) and aeolian strata (Swanson et al., 2019; Cardenas et al., 2019). Therefore, the reporting and analysis of set thickness distributions should be considered a significant part of any quantitative reconstruction of clastic sedimentary systems where there is an interest in understanding the kinematics and transport within the ancient system.

When taken together, all measured dune sets ($n = 350$) have a c_v of 0.79 ± 0.04 . While not in the realm of true bypass ($c_v = 0.88 \pm 0.3$; Bridge 1997), the value implies variable scour is the dominant control on stratification. The scour-dominated case also creates laterally discontinuous sets (Jerolmack and Mohrig, 2005; Cardenas et al., 2019). This scour dominance appears to be at odds with the preservation of bar ‘form sets’ described above. To understand the construction of the channel belt, measurements must be subdivided by environment and locally normalized. The blind application of these analyses, without considering local architecture, can result in inaccurate interpretations.

Set-thickness analysis performed separately for bar lee sets, bar stoss sets, and thalweg sets yielded a different result. In order to combine all of the measurements from these three different channel-bottom environments, set thicknesses were first normalized

by their local average value. Normalized cumulative distribution functions (CDFs) are shown in Figure 2.20A to C. Coefficients of variation for the normalized distributions are 0.29 ± 0.04 for lee sets, 0.47 ± 0.07 for stoss sets, and 0.67 ± 0.10 for thalweg sets. Although c_v values as low as 0.29 were not examined by Jerolmack and Mohrig (2005), interpolation of their Figure 4B leads to a ratio of aggradation rate to migration rate for lee sets of $\sim 10^{-1}$ (climb angle from 5° - 6°). Stoss sets have a ratio of $\sim 10^{-1.5}$ (climb angle from 1° - 2°), and thalweg sets have a ratio of $\sim 10^{-2.5}$ (climb angle from 0.1° - 0.2°). The lee sides of downstream-migrating barforms, where we should expect the most sedimentation (Reesink et al., 2015), have the highest ratio of aggradation rate to migration rate. This significant aggradation is supported by a Kolmogorov-Smirnov statistical test comparing the measurements to fitted exponential and gamma curves (Fig. 2.20A to C). For lee sets, the exponential curve is rejected at a significance level of 0.05 ($p < 0.001$), and the gamma curve is not ($p = 0.46$). This is consistent with the observed stacking and downstream thickening of sets in lee-type architectures (Fig. 2.14). Even though thalweg sets are rejected as being exponentially distributed ($p = 0.02$) and not rejected as gamma distributed ($p = 0.17$), the two fitted curves are more similar than in the lee and stoss cases.

A non-trivial amount of climb is recorded by stoss sets, given the c_v of 0.47 ± 0.07 , rejection of an exponential fit ($p = 0.01$), and non-rejection of a gamma fit ($p = 0.90$). This does not directly support the interpretation that these sets are the record of erosive dunes removing sediment from bar stoss slopes and transporting it to bar lee slopes, driving bar migration. The upstream-dipping basal scour surfaces and the presence of few stacked sets support the stoss interpretation (Fig. 2.13), but a significantly higher c_v of 0.88 ± 0.3 is

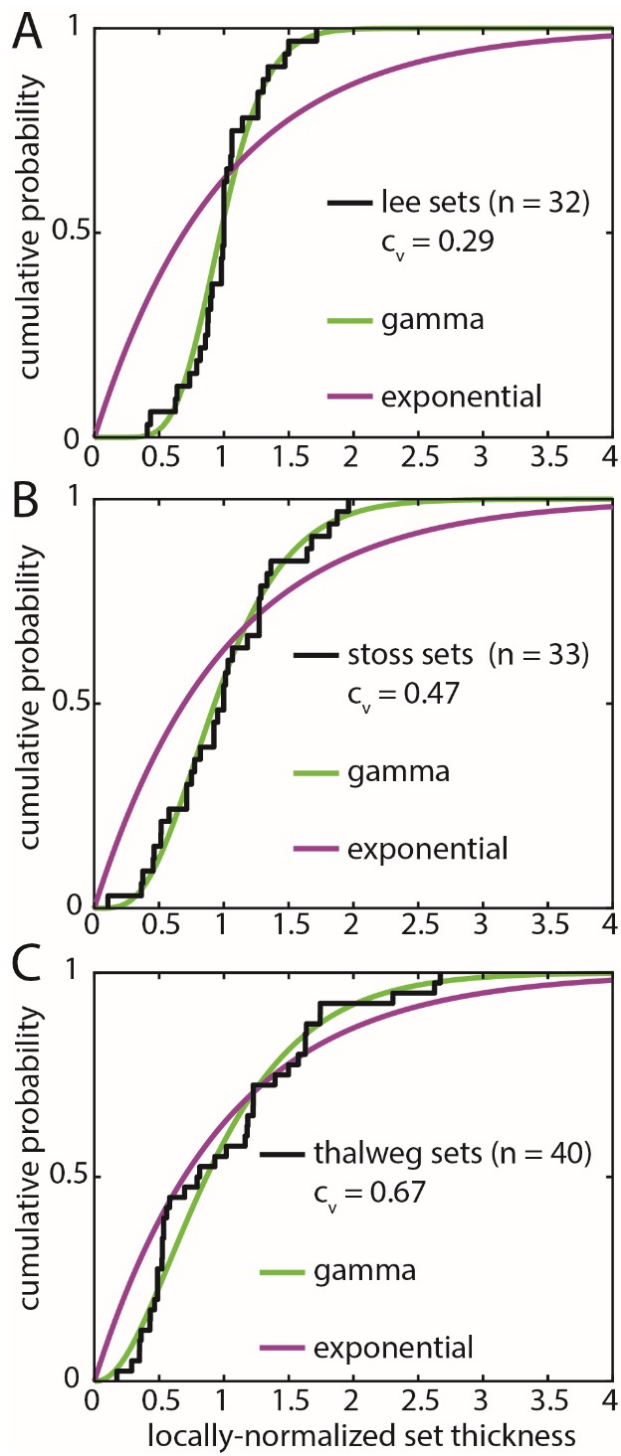


Figure 2.20

Figure 2.20 (A) Cumulative distribution function (CDF) showing the mean-normalized distribution of set thickness located within bar lee environments (Fig. 2.14). (B) CDF of set thickness within bar stoss environments (Fig. 2.13). (C) CDF of thalweg set thickness (Fig. 2.15). The best-fit gamma and exponential curves are shown for each distribution. In all cases, the exponential fits are rejected using a Kalmogorov-Smirnov test at a significance level of .05, and the gamma fits are not. This suggests all architectures required a significant rate of bed aggradation relative to the rate of dune migration, although the similarity of the two curves for thalweg sets indicates the ratio of bed aggradation to dune migration was the lowest of the three environments (Paola and Borgman, 1991; Jerolmack and Mohrig, 2005).

expected (Paola and Borgman, 1991; Bridge, 1997). Bar stoss slopes are erosional most of the time, as required for bar migration, but by chance, we have primarily observed the record of short-lived episodes of upstream stoss-slope accretion. Using ground-penetrating radar cross sections, Skelly et al. (2003) interpreted upstream accretion in recent fluvial channel-fills of the Niobrara River, Nebraska, USA.

2.4.5.2 Constraints on the time recorded by individual channel belts

How is time distributed through Cedar Mountain channel belts? Backing out sedimentation rates from these strata would provide information on the kinematics of the Cedar Mountain rivers, as well as how local controls might dictate the construction of the rock record (Sadler, 1981; Jerolmack and Sadler, 2015; Paola et al., 2018). The distribution of cross-set thicknesses, in conjunction with assumed bedform migration rates, provides some sense of how much time is preserved within individual channel belts. Given that the accumulation of dune sets at the bar lee is the process through which these bars migrated (Fig. 2.14), it follows that

$$r_{lee} / c_{lee} = s_{bar} / m_{bar} \quad (2)$$

where r_{lee} is the aggradation rate of the bed, c_{lee} is the migration rate of dunes, r_{lee} / c_{lee} is associated with a particular c_v and does not vary significantly with the calculated standard error (Jerolmack and Mohrig, 2005, their Fig. 2.4B), and m_{bar} is the dune migration distance required to stack cross sets up to the average bar thickness, s_{bar} (Fig. 2.21A-C). Solving for s_{bar} , the only unknown, yields

$$s_{bar} = 1.28 \text{ m} \pm 0.05 \text{ m} / 10^{-1} \quad (3)$$

which equals $12.8 \text{ m} \pm 0.5 \text{ m}$ of bar migration. In the North Loup River, downstream-migrating bars migrate $\sim 10 \text{ m}$ per day. Assuming this is a comparable rate to the ancient Cedar Mountain fluvial system, the observed lee architectures are a record of only $\sim 1.28 \pm 0.05$ days of sedimentation. This suggests (1) the bar strata and associated compound dune strata do not record the gradual aggradation of the channel bed towards leading up to avulsion, but rather record the higher frequency modification of the channel bed via bar migration, and (2) the gradual aggradation of the channel bed might instead be recorded in thalweg strata. To test this hypothesis, we redefine Equation 2 in terms of the thalweg sets and the average channel belt thickness:

$$r_{thalweg} / c_{thalweg} = s_{belt} / m_{thalweg} \quad (4)$$

Solving for the amount of necessary dune migration to construct the median channel belt thickness,

$$m_{thalweg} = 2.80 \text{ m} \pm 0.27 \text{ m} / 10^{-2.5} \quad (5)$$

which equals $885 \text{ m} \pm 85 \text{ m}$ of necessary dune migration (Fig. 2.21A-C). The average instantaneous dune migration rate in the North Loup, independent of flow size or dune depth, is 60 m per day (Mohrig and Smith, 1996). Assuming steady construction at this rate, only $14.8 \text{ days} \pm 1.4 \text{ days}$ are required to accumulate the thalweg strata reported here. This rejects the hypothesis that the thalweg strata record the gradual aggradation of the channel bed over its total occupation. For most rivers, occupation may last anywhere from years to thousands of years (Stouthamer and Berendsen, 2001; Slingerland and Smith, 2004). It is unlikely these channels were only occupied for 14.8 days. Instead, these strata may only represent the aggradation that occurred during the final episode of

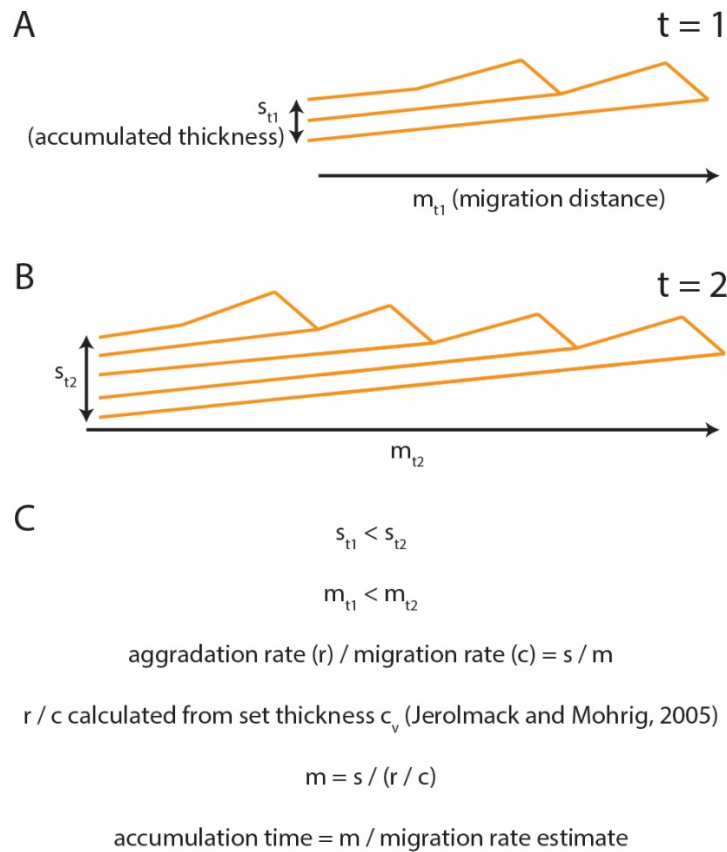


Figure 2.21 A diagram explaining the calculation of accumulation time of dune cosets with thickness s , assuming continuous transport. Dune cosets may be located on bars or the thalweg. Dune migration is towards the right. (A) At $t = 1$, dunes with a given ratio of aggradation rate (r) to migration rate (c) migrate a distance of m_{t1} , leaving a deposit of thickness s_{t1} . At $t = 2$, this process has continued with the same r and c . Dunes have migrated a farther distance, m_{t2} , accumulating a thicker coset package, s_{t2} . (C) Algebraic setup to solve for total accumulation time with an assumed dune migration rate.

deposition that preceded avulsion and channel abandonment. This episode is likely to coincide with the final flood prior to avulsion. This result suggests that the channel is in a state of bypass for most of its occupation. Had channel abandonment not prevented it, the aggradation recorded by each channel belt would likely have been completely reworked. This also suggests that floodplain deposits might more completely record successive

episodes of flood-stage deposition than channel fills, as presumably an episode of deposition is not immediately followed by reworking and removal. The complete reworking of the channel bed has, in fact, been observed in modern net-depositional rivers (Nittrouer et al., 2011a)

Alternatively, the aggradation of the thalweg may represent $14.8 \text{ days} \pm 1.4 \text{ day}$ of accumulation spread intermittently over a longer time period, as much as $740 \text{ days} \pm 70 \text{ days}$ if a commonly assumed intermittency, the fraction of time per year spent at bankfull flow, of 0.02 is used (Parker et al., 1998). However, there is no stratigraphic indicator that the accumulations within a single channel belt are the product of multiple small depositional episodes separated by hiatuses (e.g., aeolian reworking, Carling and Leclair, 2019). Accounting for this would require the assumptions that there was no reworking of the channel bed between depositional episodes (e.g., significant channel bed reworking shown in Nittrouer et al., 2011b; Shaw and Mohrig, 2014; Mason and Mohrig, in review), and that dune migration perfectly resumed right where the previous episode of sedimentation left off. It is more likely that such gradual bed aggradation would produce a scour-and-fill style architecture and a higher c_v of 0.88 ± 0.03 (e.g., Paola and Borgman, 1991; Bridge and Best, 1997; Bridge, 1997; Jerolmack and Mohrig, 2005; Cardenas et al., 2019). This is not to say that an intermittency of 0.02 is impossible or unlikely for these rivers; it simply cannot be constrained using only the accumulation rates of the final episode of sedimentation along a continuously reworked channel bed.

The lack of gradual channel-bed aggradation may also be recorded by the ratio of the total median channel-belt thickness ($2.80 \text{ m} \pm 0.27 \text{ m}$) to the average channel depth (1.28

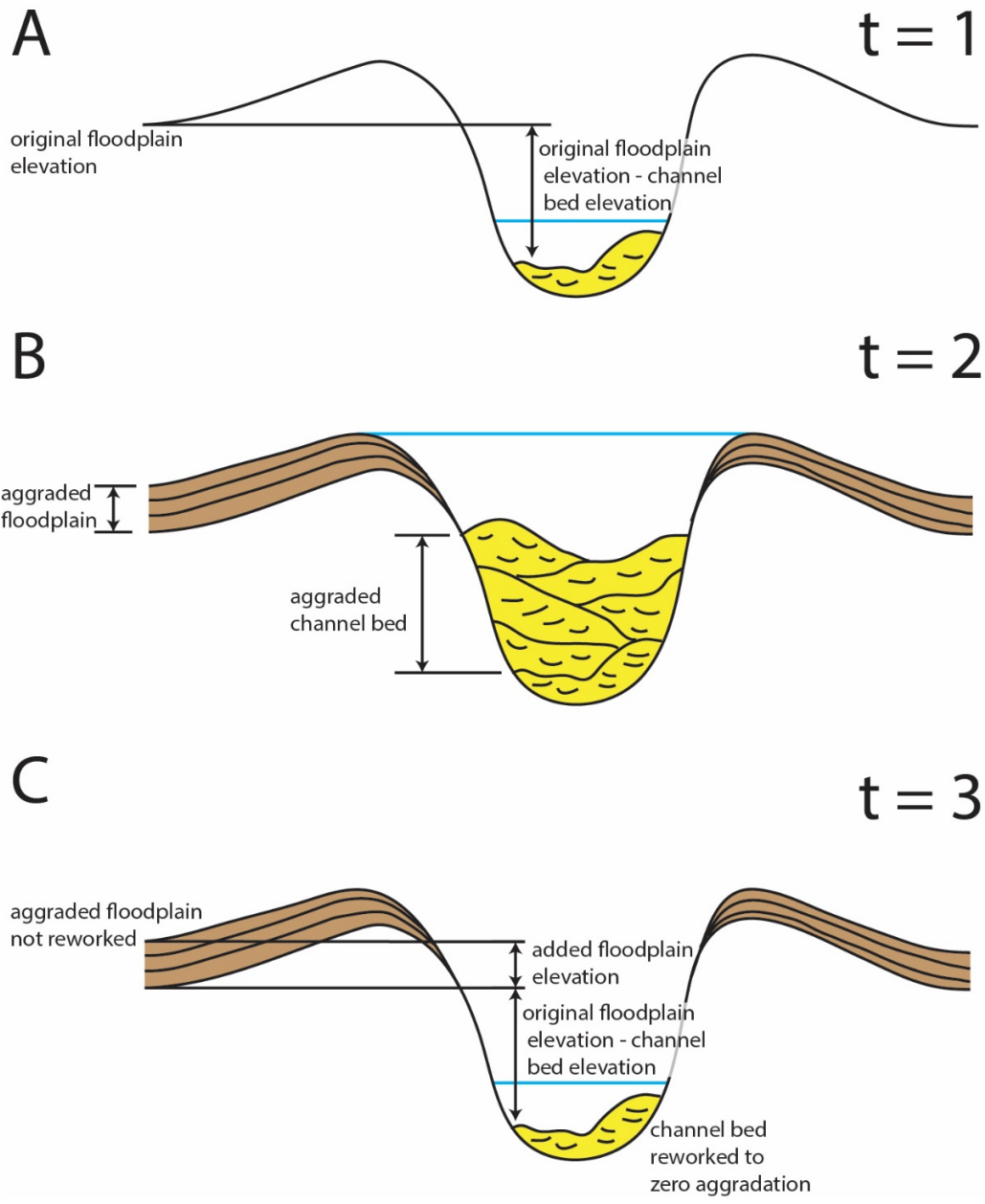


Figure 2.22

Figure 2.22 (continued from previous page) A diagram merging the observations of the usually bypass-state channel bed and the relatively high amount of channel-bed aggradation preceding avulsion, when compared to other fluvial strata (e.g., Mohrig et al., 2000). (A) at $t = 1$, the distance between the lowest part of the floodplain and the channel bed during low flow is defined. (B) At $t = 2$, the channel is in flood stage. The floodplain has aggraded less than the channel bed. Avulsion does not occur. (C) At $t = 3$, the channel bed has been reworked to the configuration of $t = 1$, maintaining its net-sediment bypass state. The floodplain has not been reworked. Thus, the vertical distance between the channel bed and the lowest part of the floodplain has increased. On average, more channel-bed aggradation will be required to set up an avulsion.

m \pm 0.05 m), 2.19 \pm 0.23. This ratio is higher than recorded in other systems (1.84 in the Guadalupe-Matarranya system, Spain; Mohrig et al., 2000). The higher value in the Cedar Mountain may represent this punctuated channel-bed aggradation, where most accumulated sediment in the channel is reworked to zero net accumulation shortly after, coupled with a contrasting steady, gradual levee and floodplain aggradation, assuming these overbank environments are less likely to be reworked to a state of zero net aggradation between floods. That is, in order for the channel bed to reach the threshold superelevation to avulse, more channel bed aggradation was required during the final depositional episode to catch up with steadily aggraded levees and floodplain (Fig. 2.22).

2.4.6 Comparison to other fluvial systems and strata

The Cedar Mountain rivers may represent an end-member behavior, opposite to a channel bed undergoing steady aggradation and frequent but partial reworking, such as described in Carling and Leclair (2019). In that work, an entrenched reach of the Luni River, India, is shown to repeatedly partially rework and scour its bed during floods, but optically-stimulated luminescence age dates show a trend of increasing age with depth, topping out at 1.9 ka (their Table 2). This is a record of slow, steady bed aggradation over the last 1.9 ka with each flood, rather than the rapid sedimentation frozen in place following channel abandonment in the Cedar Mountain. As another counter example, the Cretaceous McMurray Formation, seismically imaged in the subsurface of Alberta, Canada, has recorded multiple channel widths of lateral accretion and meander bend cutoffs within the channel belt, which has been demonstrated to drive the erosion of formative channel

elements (Durkin et al., 2018), as well alter the geometry of the channel belt relative to the formative river channel (their Fig. 12). Durkin et al. (2018) estimate a minimum of 4,000 years to produce the observed reworking. Indeed, heavily reworked examples of fluvial strata exist, and the given examples require contrasting processes to the Cedar Mountain ancient fluvial system. Their accumulations represent longer time scales, as well. River avulsions into local topographic lows formed between abandoned, raised channel beds has been shown to locally increase sedimentation rates and prevent reworking, leading to well-preserved channel belts at the km scale (Swartz et al., in review; Cardenas et al., in review). Given the total extent of the Cedar Mountain ridges and the relatively rapid sedimentation rates, this process may also be at work here.

2.5 CONCLUSIONS

The belts of the Cedar Mountain Formation represent rivers that avulsed frequently enough to limit lateral migration of any single channel. This is similar to the kinematics of megafan channels, which can avulse on the scale of years and don't generally migrate to any significant degree (e.g., Horton and DeCelles, 2001; Chakraborty et al., 2010), although the time required to aggrade the thalwegs required an environment capable of sustaining sediment-transporting flows for at least 16 days continuously. In addition to capturing what may be a common bankfull event, 41% of any belt represents a day's worth of free bar migration. This further supports the "strange ordinariness" (Paola et al., 2018) of much of the stratigraphic record, as well as the frequently observed phenomenon that most of the time represented in a stratigraphic section is recorded by erosional or hiatal

surfaces between punctuated depositional episodes, rather than the accumulations (Sadler, 1981; Miall, 2015; Sadler and Jerolmack, 2015; Paola et al., 2018). This methodology provides a framework for the quantitative analysis of other modern and ancient fluvial systems. The distribution of dune cross-set thicknesses within the context of bar topography is the dataset at the root of this analysis, and should be emphasized in future field campaigns, including the exhumed fluvial strata that will be examined during the 2020 Mars rover mission to Jezero crater (Goudge et al., 2018).

2.6 ACKNOWLEDGEMENTS

Hima Hassenruck-Gudipati, Woong Mo Koo, and David Brown are thanked for their field assistance. The staff of Green River State Park, Utah, were accommodating to our large group. This work has improved following discussions with members of the David Mohrig Research Group and the Quantitative Clastics Laboratory, as well as Zoltan Sylvester, Wonsuck Kim, Joel Johnson, Paola Passalacqua, Alistair Hayden, Mike Lamb, Jenn Pickering, and Tim Demko. Funding was provided by the University of Texas Jackson School of Geosciences, the University of Texas Graduate School, and the RioMAR Industry Consortium.

Chapter 3: Setting Up the Preservation of Fluvial Channel Belts

3.1 INTRODUCTION

Fluvial channel belts are commonly preserved over km to 10s of km in locations where such continuous preservation is not expected due to low subsidence rates (Paola et al., 2018). At the bedform scale, topography at scales larger than the bedform can drive relatively rapid sedimentation and can provide protection from later reworking, leading to well-preserved deposits (Reesink et al., 2015; Miall, 2015). For example, fully preserved fluvial dune “form-sets” are found at the downstream end of larger bar forms (Reesink et al., 2015). At larger scales, Paola et al. (2018) acknowledged the ‘strange ordinariness’ of much of the fluvial stratigraphic record, meaning these deposits represent apparently short durations at normal rather than extreme conditions. Is there a source of larger-scale topography capable of preserving fluvial channel-belts for km to 10s of km constructed under ordinary conditions? Incised valleys fill this role, but well-preserved channel belts are not limited to valley fills. Recently, drainage basins have been identified across the coastal plains of the US Gulf of Mexico and Atlantic Ocean (Willett et al., 2014; Swartz et al., in review). These basins provide up to 10s of m of relief for the potential preservation of channel-belt segments 10s of km in length (Fig. 3.1; Swartz et al., in review). Raised alluvial ridges, constructed by active coastal rivers, make up the drainage divides between these tributary basins (Fig. 3.1). Smaller-scale erosional tributary channel networks drain water and sediment from tributary basins into the gulf, thus limiting floodplain aggradation and creating additional erosional relief (Fig. 3.1; Swartz et al., in prep).

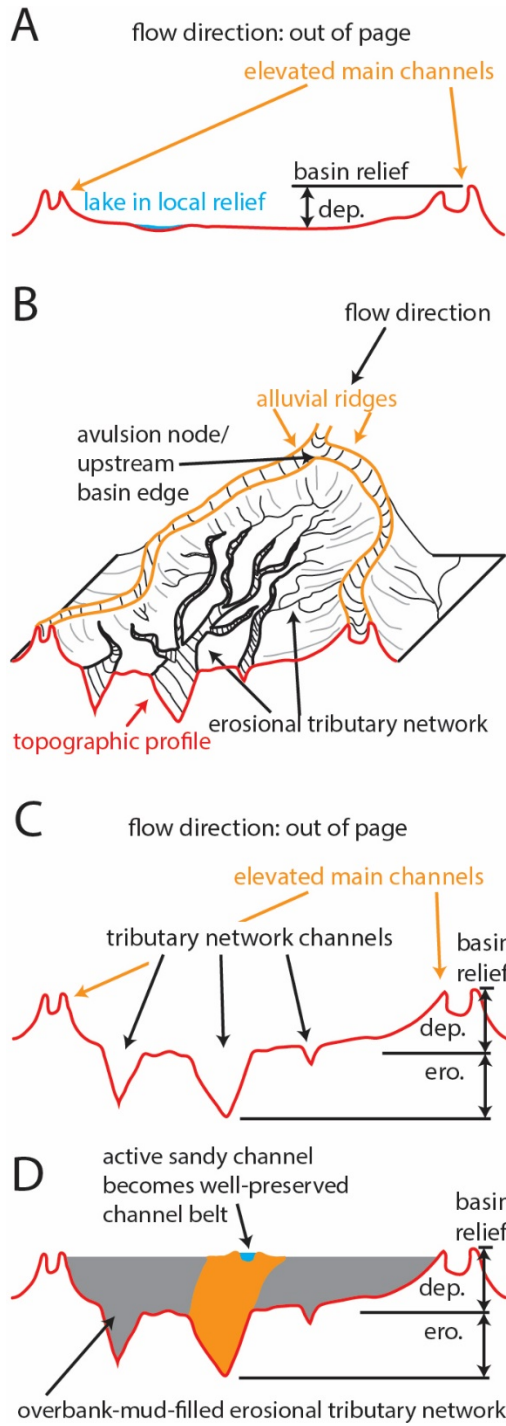


Figure 3.1

Figure 3.1 A: Schematic transect between two raised alluvial ridges without the development of an erosional tributary network. Relief only forms from the decrease in sedimentation away from the main channels. While some local relief can create lakes, the overall relief is less than in panels B and C. B: Three-dimensional illustration of an erosional tributary network developed within a basin confined and bounded by alluvial ridges (Swartz et al., in review). Alluvial ridges built by larger, sand-transporting channels (orange) define the basin boundaries. The erosional tributary network is drawn using black lines. The topographic profile at the edge of the diagram is shown with the red line, with the erosional channels generating v-shaped incisions. C: The red line showing relief in panels A and B. This relief is generated due to decreased sedimentation away from the channel (A), as well as the erosional tributary network channels (B). D: A sandy depositional channel has avulsed into the basin, where it has filled the basin with a sandy channel belt and muddy overbank deposits.

We hypothesize that the larger-scale primary depositional channels could avulse and re-route into adjacent tributary basins, where they could fill topographic levels below the reworking depths of primary fluvial activity (Fig. 3.1D). This hypothesis is tested by 3D seismic reflection volume mapping of fluvial channel belts preserved in the subsurface Gulf of Mexico offshore Brazos River, TX, USA. 3D seismic reflection volumes have been proven useful in reconstructing the kinematics of ancient fluvial systems (Wood, 2007; Hubbard et al., 2011; Armstrong et al., 2014; Jobe et al., 2016), and towards understanding preservation and re-working within channel belts (Durkin et al., 2018). In this study, the term “channel belt” defines the sum total of all channel-filling deposits left by a river, regardless of how much, or how little, lateral migration and aggradation was recorded (Blum and Törnqvist, 2000; Gibling, 2006; Jerolmack and Mohrig, 2007). A channelized feature lacking channel fill is not a channel belt.

3.2 METHODS

A 3D seismic reflection volume of the Brazos River delta was downloaded from the National Archive of Marine Seismic Surveys (NAMSS; volume B-18-93-TX). This data volume was collected in 1993 and covered an area of ~2,300 km² from 15 km to 50 km offshore Texas (Fig. 3.2), with lines spaced 20 m apart. This study was restricted to the relatively shallow subsurface, the first 1000 milliseconds of acoustic wave two-way-travel time (ms TWT), with 0 at sea level and values becoming more negative with increasing depth. This volume clearly imaged four clusters of channelized features with the best possible resolution afforded by the highest possible frequency content for the reflected

acoustic waves. Amplitude volumes from the NAMSS were opened in Petrel software to map the bottom surfaces of channelized features in cross-sectional views (Fig. 3.3A-E). The amplitude volumes were then processed into variance volumes, which placed strong returns where adjacent seismic lines were less similar, and weak returns where adjacent lines are more similar (Bahorich and Farmer, 1995). This can be considered a 3D volume of amplitude curvature, or edge detection, which has been demonstrated to accentuate channel-belt boundaries (Bahorich and Farmer, 1995; Liu and Marfurt, 2007; Armstrong, 2012). Furthermore, time slices from the variance volume were used to map channelized features and to define underlying surfaces interpreted as defining tributary basins. Ultimately these basal surfaces were mapped in the amplitude volume that provided the greatest vertical resolution (Fig. 3.3A-E). The basal surfaces of channelized features were mapped across the feature's lateral extent as observed in the time slice variance image, using truncated reflectors as a guide (Fig. 3.3B-C). Surfaces mapped in the along-belt direction (Fig. 3.3D-E) were then used to tie cross sections (Fig. 3.3B) to less obvious views (Fig. 3.3C). Next, surfaces interpolated between mapped horizons were converted to grids of points with XYZ coordinates, where a distribution of Z values (depth in units of ms TWT) was extracted from each surface to help quantify its stratigraphic position.

After cross-sectional mapping, selected variance time slices were exported from Petrel and into ArcGIS, in order to perform more robust planview mapping operations. The centerline length and average width of channel belts were calculated by first mapping the opposite long edges of each feature as a series of ~2 m spaced points with XY coordinates. A local measurement of width was made from each point along one edge to the nearest

point on the opposite edge using an automated script, and a centerline point was placed halfway between the two points. Width measurements were averaged for each feature, and the centerline length was calculated as the sum of the distances between successive centerline points.

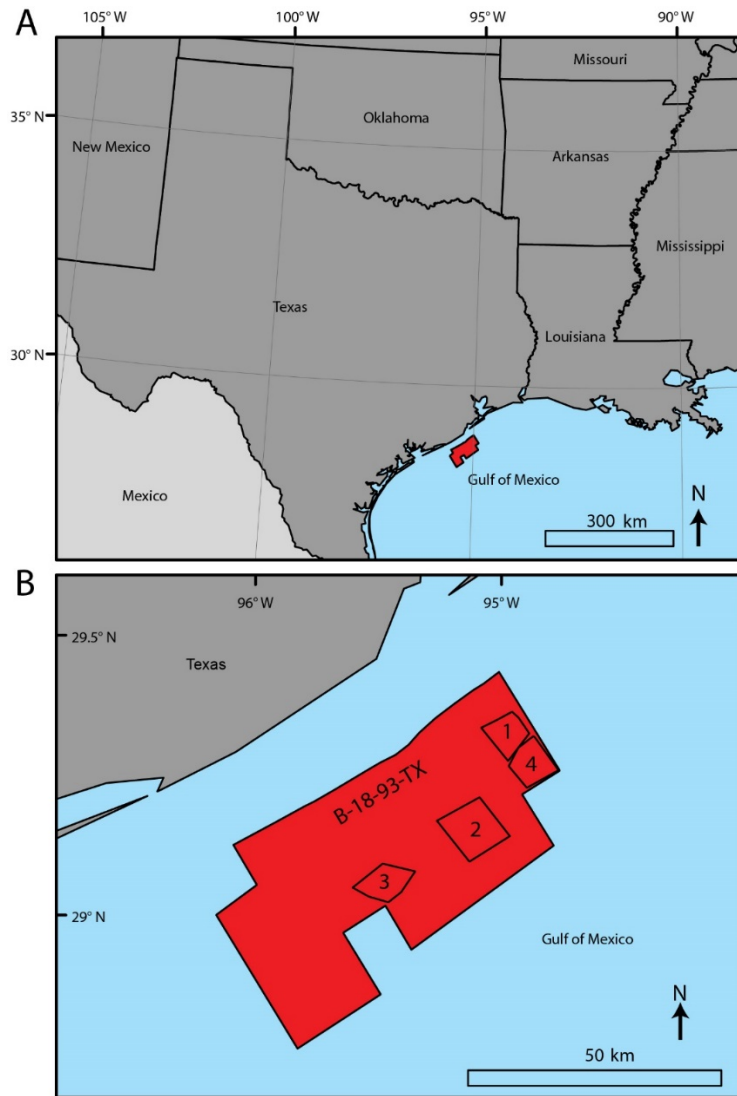


Figure 3.2 Location map for the offshore seismic survey B-18-93-TX. The spatial extent of the survey is mapped in red. B: Zoom in to the survey area, with the mapped extent of the four studied zones.

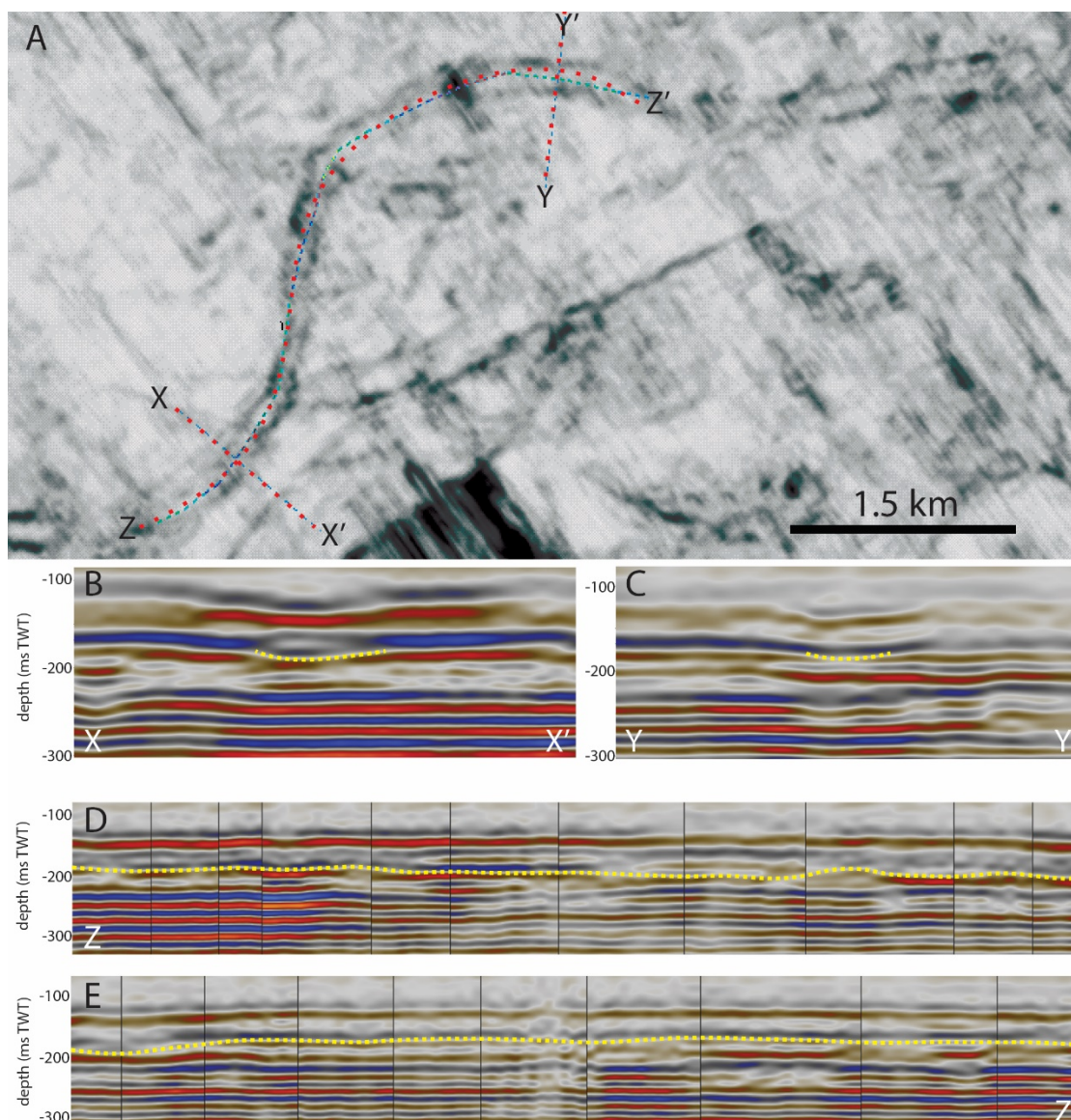


Figure 3.3 A: Variance time slice showing a fluvial channel belt from zone 2 (Fig. 3.2). Lines X-X' and Y-Y' show the locations of cross-belt sections in panels B and C. Line Z-Z' defines an approximate centerline section for the belt that is presented in panels D and E. B: Cross-section X-X', with a yellow line marking the belt base. Erosion by this surface clearly truncated reflectors to either side of the channel belt. C: Cross-section Y-Y' with a yellow line marking the interpreted base of the same belt. The amplitude contrast at the belt base is not as stark as in X-X'. D and E: Cross-section Z-Z' over two panels. The belt bottom mapped in this cross-section ties X-X', where the belt is clearly identified, to Y-Y', where it is less easily identified.

3.3 RESULTS

Two populations of channelized features were identified in each of the four survey zones (Fig. 3.2). The division between populations is clear upon visual inspection (Figs. 3.4A-L) and quantification (Table 3.1; Fig. 3.5A). Of the 156 mapped channelized features, 17 define a population of longer features, and the remaining 139 define a population of shorter features (Table 3.1). To test if the shorter channelized features define the bottom of an eroded tributary drainage basin filled by the longer channelized features, we observed the stratigraphic arrangement of long and short features using time slices at different depths (Fig. 3.4), histograms of ms TWT values (Fig. 3.5), 3-D renderings (Fig. 3.6), and depth profiles (Fig. 3.7). The 3-D renderings, depth profiles, and histograms both compare a “zone-scale basal surface” to the longer channelized features. The zone-scale basal surfaces were created in Petrel by interpolating a 3-D surface between the mapped bases of the shorter channelized features, limited to each zone’s extent (Fig. 3.1). There is a consistent stratigraphic arrangement of the long channelized features and the zone-scale basal surfaces in zones 1-3, with the shorter channelized features from 0 to 60 ms TWT beneath the longer channelized features (Figs. 3.4-3.7). There is no instance of a group of longer channelized features located beneath shorter features. Zone 4 also contains both types of channelized feature in a similar arrangement, but both exist within a larger topographic container not observed in zones 1-3 (Figs. 3.5 and 3.8). Rather, zone 4’s basal surface is instead defined by a larger-scale topographic container, which has a distinct distribution of depth values, including a range 3 times larger than the other zones (~300 ms TWT vs. 60-100 ms TWT; Fig. 3.5E) and a long tail towards shallower depths (Fig. 3.5E). In variance

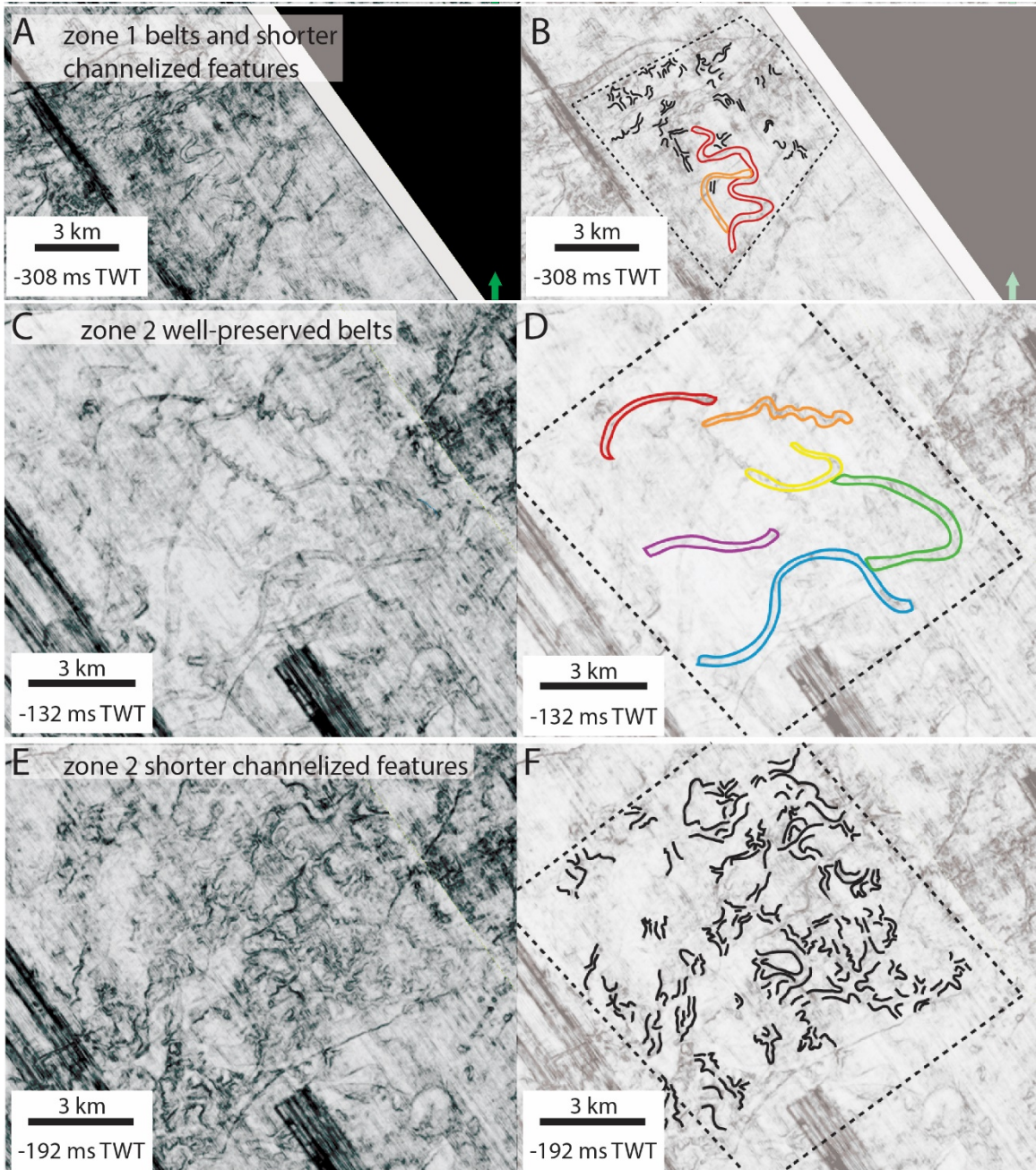


Figure 3.4A-F

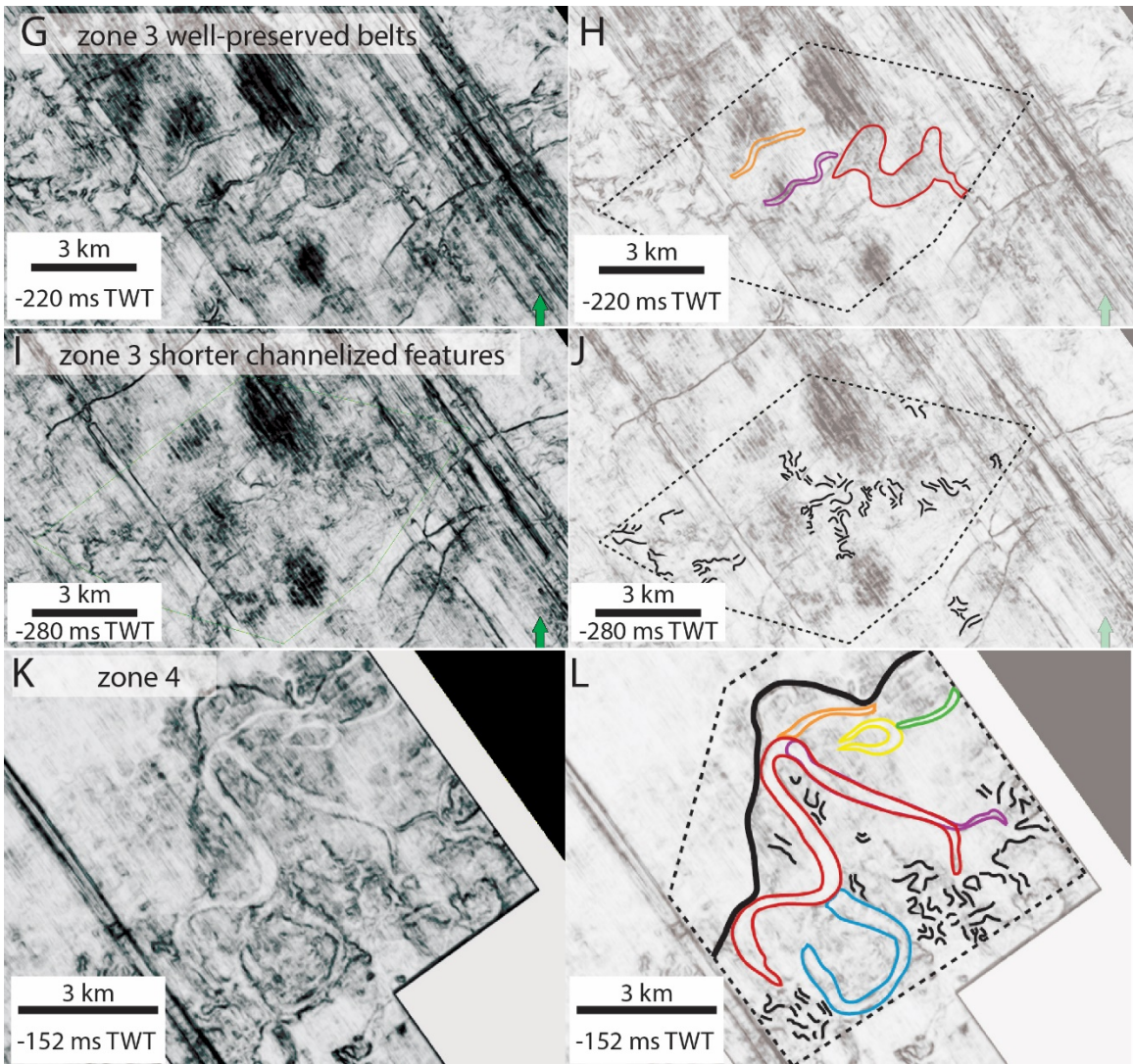


Figure 3.4G-I

Figure 3.4 Time slices from the variance volumes showing long channelized features (colored lines), short channelized features (black lines), and the mapped extent of zone-scale basal surfaces (dashed polygons). Increasingly negative values (ms TWT) represent increasing depth below the sea floor, with 0 ms TWT at sea level. The location of each zone is shown in Figure 3.2. A: Variance time slice of zone 1 at -308 ms TWT. B: Interpretation of panel A showing 2 distinct long channelized features, and several short channelized features. C: Time slice of zone 2 at -132 ms TWT. D: Interpretation of panel C showing 6 long channelized features. E: Time slice of zone 2 at -192 ms TWT. F: Interpretation of panel E, showing many short channelized features. G: Time slice of zone 3 at -220 ms TWT. H: Interpretation of panel H, showing 3 distinct long channelized features. I: Time slice of zone 3 at -280 ms TWT. J: Interpretation of panel I, showing several short channelized features. K: Time slice of zone 4 at -152 ms TWT. L: Interpretation of panel K, showing 6 distinct long channelized features and several short channelized features. The scalloped surface bounding the channelized features is mapped in a bold, solid black line.

	channelized feature	
	short (n = 139)	long (n = 17)
length		
mean (m) ± standard error (m)	368 ± 16	5,251 ± 729
minimum (m)	95	1,644
maximum (m)	1,043	13,074
standard deviation (m) ± standard error (m)	188 ± 11	3,005 ± 531
feature-averaged width		
mean (m) ± standard error (m)	155 ± 4	250 ± 39
minimum (m)	72	140
maximum (m)	276	831
standard deviation (m) ± standard error (m)	48 ± 3	159 ± 28

Table 3.1 – Geometry of the short and long channelized features.

time slices, this surface has a scalloped shape and acts as a western boundary to the zone 4 channel-belt cluster (Fig. 3.4).

3.4 DISCUSSION

The two populations of channelized features, distinguished by length (Fig. 3.5A; Table 3.1), record the kinematics and filling of their formative river channels (Gibling, 2006; Jerolmack and Mohrig, 2007). The longer features are interpreted as narrow channel belts. They are mappable for km because they have not been reworked following their deposition, and because they maintain an impedance contrast with the surrounding

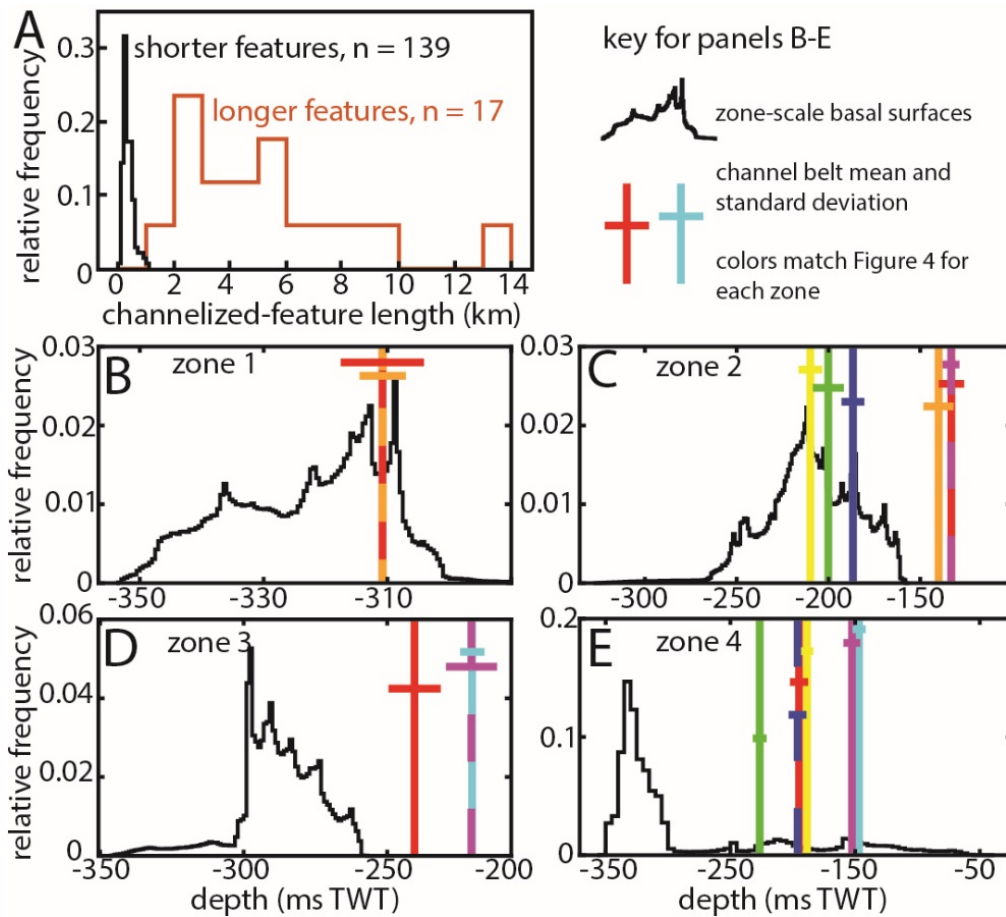


Figure 3.5 A: Histogram comparing the two distinct channel belt populations based on their length normalized to their mean width. The black line represents the length distribution of shorter channelized features (red line) above which the longer channelized features (black line) sit. B-D: Black line histograms showing the distribution of depths for zone-scale basal surfaces in each zone. Depth is measured in milliseconds of two-way-travel time, which has a value of zero at sea level, with larger negative values representing greater depths into the subsurface. Colored vertical lines are placed at the mean depths of each well-preserved channel belt, with the standard deviation around the mean represented by the cross. The average stratigraphic position of a channel belt is within 10s of ms TWT above the basal surfaces. Line colors match belt colors in Fig. 3.4. E: Same as panels B-D, but the zone-scale basal surface of zone 4 is an incised valley (Fig. 3.4L), with the floor represented by the mode of the distribution, and the valley wall represented by the long, shallowing tail of the distribution.

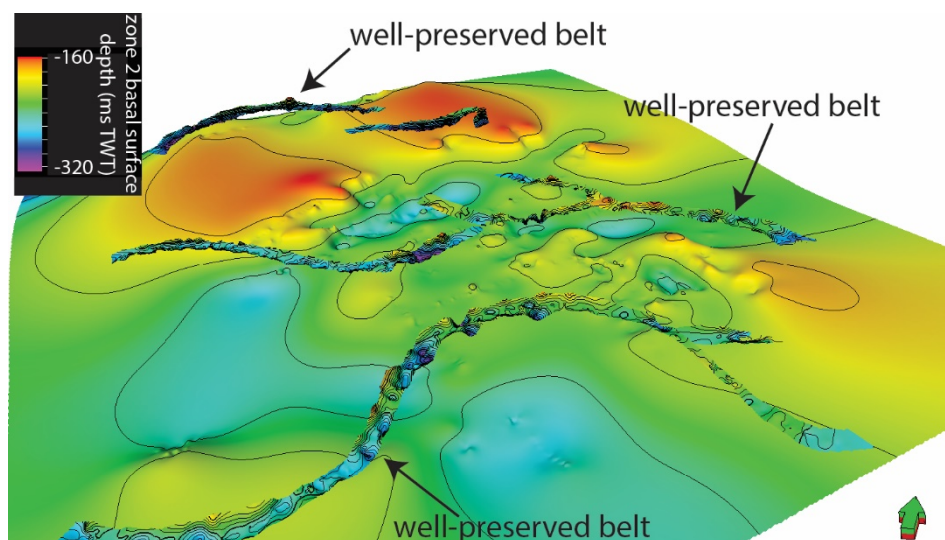


Figure 3.6 Oblique view of the well-preserved channel belts and the zone 2 basal surface (Fig. 3.4C-F). The zone-scale basal surface is color-coded by depth (see legend) with a contour interval of 50 ms TWT. Depth contours for the mapped, overlying channel belts do not match each other or the zone-scale basal surface.

sediment, likely due to a consistent sandy channel fill relative to adjacent muds. The shorter features lack this continuous impedance contrast (Fig. 3.4; Table 3.1), and thus are not interpreted as channel belts, but as erosional channels later filled by muds. The time slices (Fig. 3.4A-F), depth histograms (Figs. 3.5B-E), 3-D renderings (Fig. 3.6), and show that the zone-scale basal surfaces defined by the short erosional channels sit just 0-60 ms TWT below the long channel belts, or are slightly scoured by them. This arrangement is shown particularly clearly in the zone 2 depth profiles shown in Figure 3.7, and highlights the fact that this relationship is held across the entire length of a channel belt (Fig. 3.7C). These basal surfaces are interpreted to be the stratigraphic representations of a network of these erosional, mud-filled channels. The stratigraphic arrangement of these two sedimentologically contrasting deposits, with an erosional surface containing well-

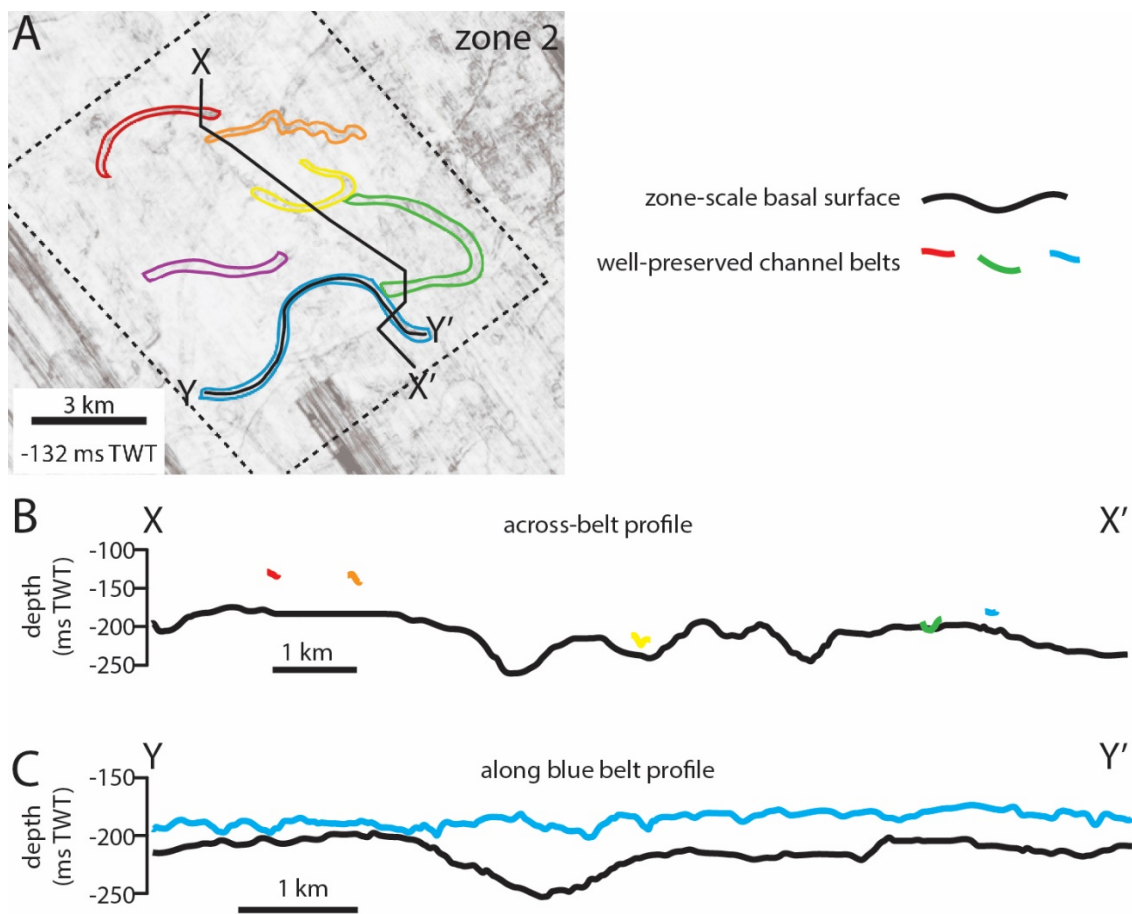


Figure 3.7 Variance time slice of zone 2 at -132 ms TWT showing the 6 long channelized features. Two cross-sections are labeled. X-X' runs roughly perpendicular to the channelized features, intersecting five of the six. Y-Y' runs along the blue channelized feature. B: Depth profiles along transect X-X' of the zone-scale basal surface (black line) and long channelized features (color lines, same colors as panel A). Belts sit less than 60 ms TWT above the zone-scale basal surface. Lateral distance is marked with a scale bar. C: Depth profile along transect Y-Y', which follows the blue channelized feature. The blue channelized feature is consistently within 10 to a few 10s of ms TWT above the zone-scale basal surface.

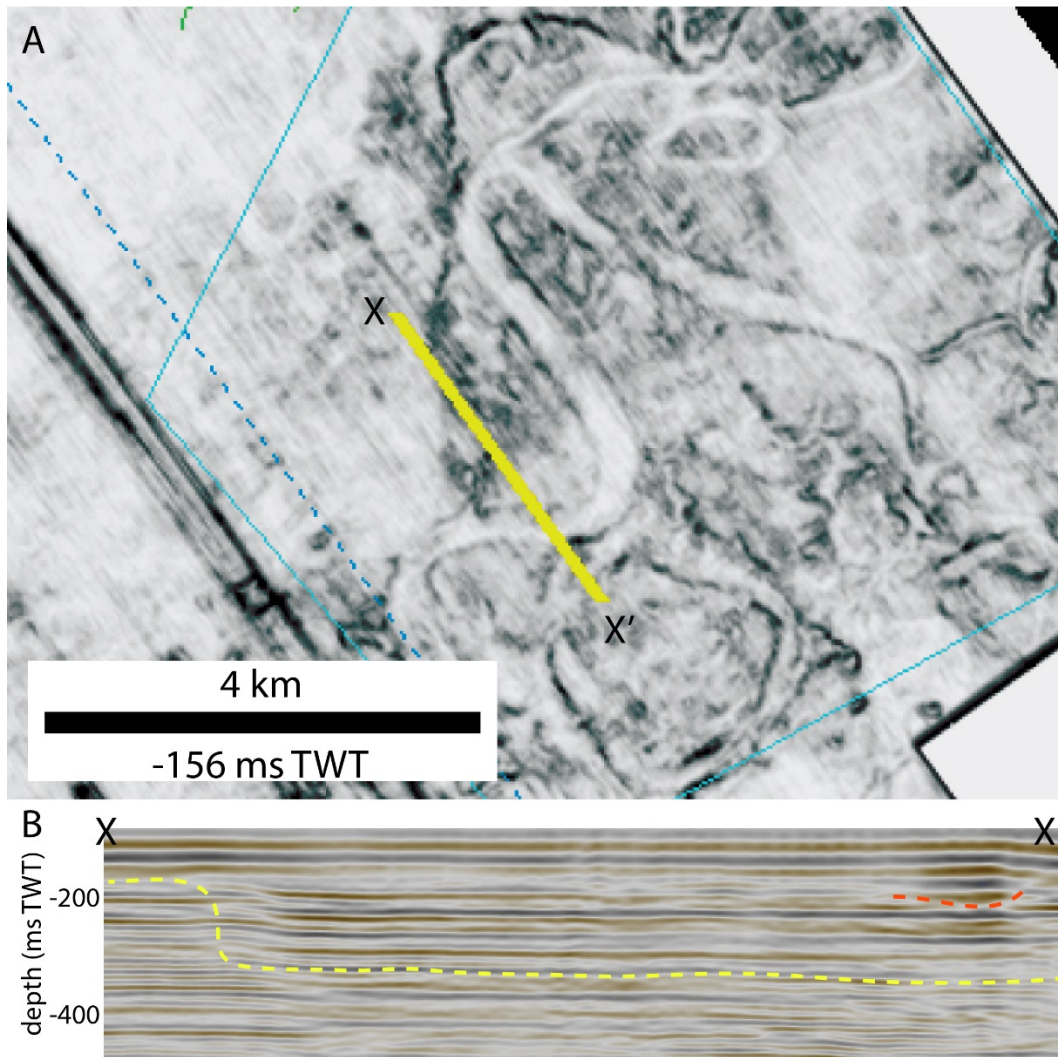


Figure 3.8 A: Variance time slice of zone 4 showing cross-section X-X', which cuts the valley wall. B: Cross-section X-X', with a yellow dashed line marking the interpreted valley floor, wall, and outside the valley on the basis of reflectors changing from conformable, to truncated, to conformable, respectively. The red channel belt is shown within the valley as well (Fig. 3.4L).

preserved channel belts, is consistent with the filling of erosional tributary drainages by avulsive, sandy rivers and associated overbank muds.

Hajek and Heller (2012) demonstrated that changes in the ratio of flow depth vs. floodplain aggradation rates can change the degree of channel-belt preservation observed

through time, where their numerical modeling and field example (the Castlegate Sandstone, Utah, USA) represent examples showing how the dominant control is change in flow depth, with steady accumulation rates. However, in this study, the apparent dependence of well-preserved belts on nearby (0-60 ms TWT) reworked surfaces instead favors a rapid change in local sedimentation rates triggered by sudden basin infilling. This preservation mechanism is largely independent of basin subsidence. Paola et al. (2018) recognized the discrepancy between channel belt preservation and subsidence rate in the Mississippi River delta. Belts from 4 to 30 km in length are preserved, even though the time required to create that space through subsidence is 10-50 times reasonable avulsion periods. Coastal tributary basins provide the relief necessary to preserve these belts, and provide a potential answer to one of the major questions asked by Paola et al. (2018): “What physical processes modulate local rates of deposition so as to produce high rates of deposition without high transport rates, leading to extraordinary preservation of ordinary events?” While it has been demonstrated that hierarchical topography can drive this variability in sedimentation at the bedform scale (Reesink et al., 2015; Cardenas et al., 2019), it is evidenced in this study to also be acting at the channel-belt scale. This is also significant in that a local topographic control was the immediate forcing upon these coastal fluvial systems, rather than a global control (i.e., relative sea level, subsidence). Deposition within these basins provides for local variability in basin-averaged sedimentation rates, a concept noted by Sadler and Jerolmack (2015).

Zone 4 is interpreted as a package of channel belts filling an incised valley based on the scalloped wall geometry (Fig. 3.4K-L) associated with truncated reflectors (Fig.

3.8), consistent with formation by outer-bank erosion by migrating rivers (e.g., Zaitlin et al., 1994; Armstrong, 2012; Cardenas et al., 2018) and the overall package thickness (Fig. 3.5E). The preservation of channel belts over several km within this valley is consistent with the demonstrated significance of hierarchical topography when setting up the preservation of fluvial channel belts. Although zones 1-3 make clear that an incised valley is not the only possible source of such topography, zone 4 provides an interesting contrast where the construction of the containing topography is controlled by external forcings (i.e., valley cutting and filling associated with relative sea-level change, Simms et al., 2007). In Figures 3.4K-L, poorly preserved belts are also observed within the valley, suggesting the possible development of coastal tributary basins within even larger-scale valleys.

3.5 CONCLUSIONS

The development and filling of coastal tributary basins, which are common geomorphic features across the modern US Gulf of Mexico coast, leaves well-preserved fluvial channel belts in the stratigraphic record of the Gulf of Mexico without the requirement of an incised valley, and significantly, in the absence of subsidence rates high enough to create channel-belt-scale relief on avulsion timescales (Paola et al., 2018). The development of these basins may also be an important control on channel-belt clustering (Hajek et al., 2010). We posit that, because such preservation has been observed in other parts of the world beyond the extent of incised valleys (e.g., Miall, 2006), these basins may have commonly helped preserve channel belts across Earth by acting as a higher hierarchical source of topography, leading to the ‘strange ordinariness’ of much of the

fluvial stratigraphic record (Paola et al., 2018). Well-preserved channel belts exhumed on Earth (Hayden et al., 2019; Cardenas et al., in review) and the surface of Mars (Burr et al., 2009; DiBiase et al., 2013; Kite et al., 2015; Davis et al., 2016; Cardenas et al., 2018; Hughes et al., 2019) may also represent the construction of these basins. Further work should investigate the consistency of the results presented here across the Gulf of Mexico, along other coasts both similar and dissimilar to the Gulf of Mexico in terms of dominant processes, and other alluvial systems where these tributary basins may develop between channels, such as foreland basin megafans/distributive fluvial systems (Horton and DeCelles, 2001; Owen et al., 2015). Additionally, the lengths of channel belts can be further developed as a constraint on the kinematics and filling of ancient channels, especially in seismic volumes or remote sensing datasets where belt thickness, an important recorded of channel kinematics (Gibling, 2006; Jerolmack and Mohrig, 2007) cannot be well constrained.

3.6 ACKNOWLEDGEMENTS

BTC thanks Zoltan Sylvester and Joel Johnson for helpful reviews of this manuscript. We thank the United States Geologic Survey for maintaining the National Archive of Marine Seismic Surveys at <http://walrus.wr.usgs.gov/namss/>. BTC acknowledges funding from the The University of Texas at Austin Graduate School, the Jackson School of Geosciences, and the RioMAR Industry Consortium.

¹Chapter 4: Autogenic processes and allogenic forcings preserved in aeolian strata

4.1 INTRODUCTION

Aeolian dune fields develop over time as a result of autogenic processes that occur in a set of environmental (allogenic) boundary conditions. Autogenic processes inherent to a field of migrating dunes include dune interactions (Werner, 1995; Coleman and Melville, 1996; Ewing and Kocurek, 2010a; Kocurek et al., 2010; Gao et al., 2015a), dune deformation with migration (Pedersen et al., 2015; Swanson et al., 2016), and dune scour of the substrate (Paola and Borgman, 1991; Bridge and Best, 1997). Common allogenic boundary conditions for aeolian systems include the presence or absence of a near-surface water table (Crabaugh and Kocurek, 1993; Kocurek and Havholm, 1993), direction and magnitude of sediment-transporting winds (Rubin, 1987; Rubin and Hunter, 1987; Ping et al., 2014; Swanson et al., 2017), sediment availability (Courrech du Pont et al., 2014; Gao et al., 2015b), and geometry of the sediment source and basin (Ewing and Kocurek, 2010b).

The general trend in dune-field development is for many, small, closely spaced dunes to coalesce into fewer, larger, widely spaced dunes over time and across space through constructive dune interactions (Ewing and Kocurek, 2010a; Eastwood et al., 2012; Gao et al., 2015a; Day and Kocurek, 2018). Aeolian strata record these interaction

¹This chapter is based on a prior publication:

Cardenas, B.T., Kocurek, G., Mohrig, D., Swanson, T., Hughes, C.M., and Brothers, S.C., 2019, Autogenic processes and allogenic forcings preserved in set-scale aeolian stratigraphy II: The scour-and-fill dominated Jurassic Page Sandstone, Arizona, USA: *Journal of Sedimentary Research*, accepted.

Cardenas led the field excursions to collect data, analyzed all data, wrote the manuscript, and created figures. Kocurek and Mohrig helped with manuscript edits. Swanson's numerical model was used with his assistance. Hughes and Brothers helped with collection of field data and on-site interpretations.

kinematics (Brothers et al., 2017; Day and Kocurek, 2017), and may potentially preserve strata associated with any phase of this development. Conversely, the presence or absence of preserved accumulations associated with different developmental stages are useful for interpreting the allogenic and autogenic forces that led to its accumulation and preservation (Kocurek and Day, 2018). The discussion of autogenic processes and allogenic forcings recorded in the sedimentary record has been focused primarily on fluvial and deep-sea environments (e.g., Castelltort and Van Den Drieschhe, 2003; Kim et al., 2006; Stouthamer and Berendsen, 2007; Paola et al., 2009; Jerolmack and Paola, 2010; Wang et al., 2011; Hajek and Straub, 2017; Paola et al., 2018). The aeolian stratigraphic record is only rarely studied under this framework (e.g., Day and Kocurek, 2017; Kocurek and Day, 2018). However, quantitative analysis of aeolian strata, as we show here and in a companion paper (Swanson et al., accepted), can contribute a lot to this fundamental aspect of sedimentary geology.

In a companion paper (Swanson et al., accepted), numerical modeling of aeolian dune-field development shows that the growth phase of a dune field is consistently associated with the reworking of older deposits. This reworking is due to the increase in depth and depth variability of scouring in dune troughs associated with autogenic dune growth. The resulting strata are relatively discontinuous and composed of the fills of a sequence of deepest scours to move through a particular location. This scour-and fill architecture records the autogenically dominated phase of dune-field development. We examined the Jurassic Page Sandstone near Page, Arizona, USA (Figs. 4.1A, 4.2), with detailed field mapping and topographic measurements. Sedimentary structures, stratal

architecture, apparent relief on bounding surfaces, and quantitative analysis of set-thickness distributions are used to test the hypothesis that the Page sets of cross strata are dominated by a scour-and-fill architecture constructed by relatively large, mature dunes.

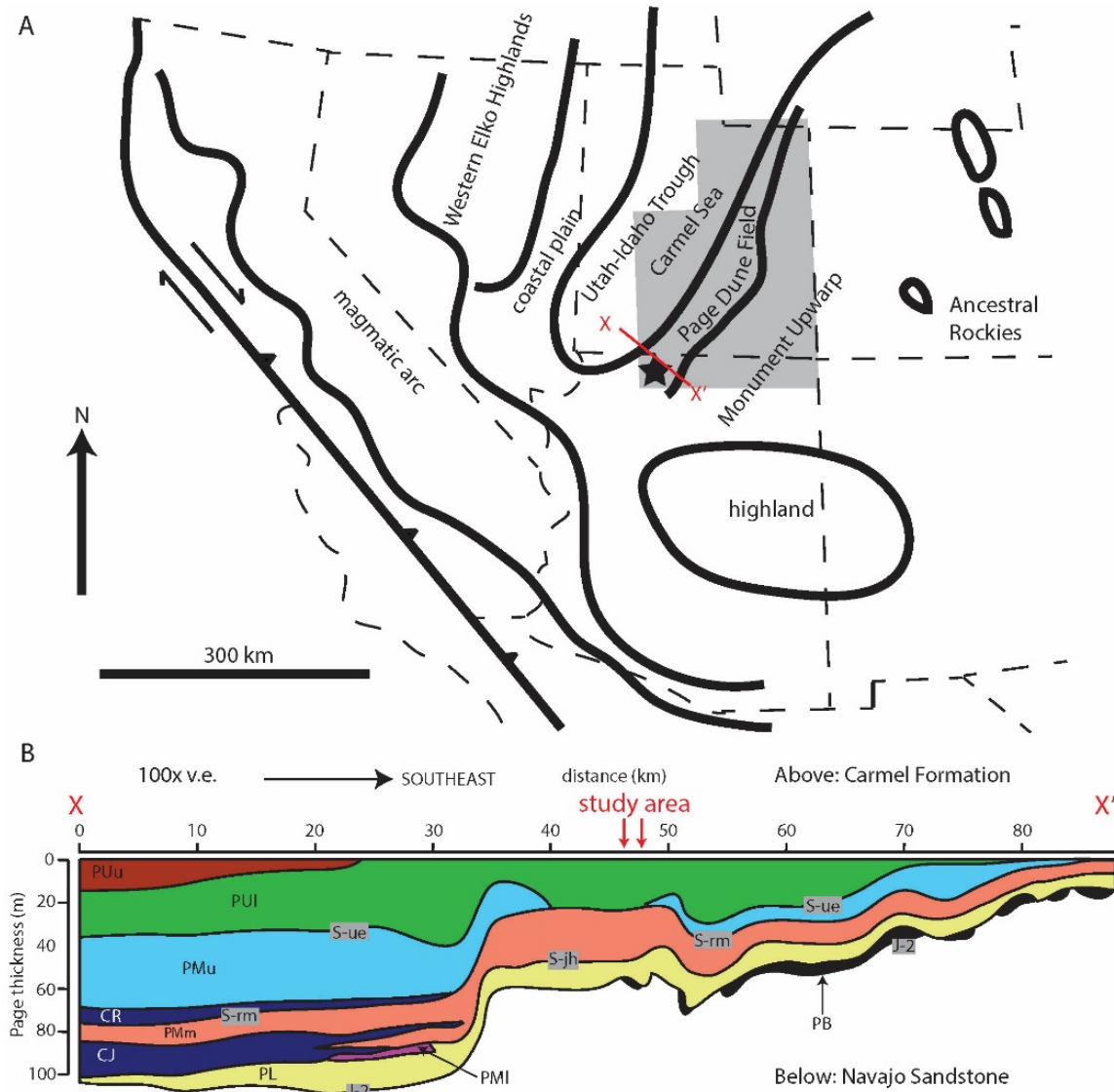


Figure 4.1

Figure 4.1 A: Paleogeography of the Western Interior during the Middle Jurassic. The Page dune fields extended along the Carmel coastline, and were not present or were not preserved eastward over the Monument Upwarp. The gray box indicates the extent of Page and Carmel mapped by Havholm et al. (1993), Jones and Blakey (1993) and Blakey et al. (1996). The black star marks the location of Page, Arizona, and the outcrops discussed in this study. The red line X-X' shows the location of the cross-section in panel B. Modified after Havholm et al. (1993) and Peterson (1994). B: NW-SE cross-section X-X' showing the architecture of the Page Sandstone over more than 80 km. Figure 4.1B is generalized after (Havholm et al., 1993, their Fig. 4D), but the cross-section has been hung from the Page/Carmel contact instead of the S-rm surface as in Havholm et al. (1993). Red arrows define the area of this study along the formation-scale cross-section. Overall, the cross-section shows the thinning of the Carmel/Page stratigraphic unit from the basin onto the flanks of the Monument Upwarp. Major formation-scale bounding surfaces separating informal units used by Havholm et al. (1993) are given. Page basal deposits (PB) and lower Page (PL) lie on the J-2 surface and are upward bounded by the S-jh surface. Westward the S-jh surface is overlain by a lower tongue of the Judd Hollow Member (CJ) of the Carmel Formation. Combined, the basal deposits and lower Page are the Harris Wash Member of Blakey et al., (1996). The middle Page (PM) or the Thousand Pockets Member of Blakey et al., (1996) is divided into lower (PMl), middle (PMm) and upper (PMu). PMl is bounded by a surface that is overlain by a higher, lesser tongue of the Judd Hollow. PMm is bounded by the S-rm surface, which is overlain westward by an upper tongue of the Judd Hollow (CR). PMu is bounded by the S-ue surface. Not shown in this cross-section, elsewhere westward the S-ue surface is overlain by the Crystal Creek Member of the Carmel. The upper Page (PUl and PUu, or the leche-e member of Blakey et al., 1996) consists of compound cross-strata not addressed in this study. The upper Page was completely transgressed and is overlain by younger members of the Carmel.

Moreover, these later-phase dunes cannibalized most strata that may have accumulated during earlier phases of dune-field development and even scoured into underlying strata from previous constructional events. In spite of this scouring, the deposits of two early dune fields with their distinct cross-strata were found preserved in local, pre-existing topographic lows. We demonstrate that antecedent topography and the depth to water table were subordinate allogenic controls on the overall stratigraphic architecture of the Page Sandstone. Interpretations were aided by the numerical model of the companion paper (Swanson et al., accepted), which couples dune morphodynamics, stratigraphy, and allogenic boundary conditions. The modeling work presented here is the product of some unique parameters not explored in the companion paper.

4.1.1 Geologic context and previous work

Jurassic aeolian formations of the Colorado Plateau are among the most studied aeolian sandstones in the world (Blakey et al., 1983, 1988; Rodríguez-López et al., 2014), and literature discussing the Page Sandstone is extensive. The Page Sandstone preserves a time series of NE-SW-trending dune fields situated between the Monument Upwarp and the Carmel inland sea (Blakey et al., 1988; Riggs and Blakey, 1993; Peterson, 1994) (Fig. 4.1A) during the middle Jurassic, 171.5 Ma to 169.5 Ma (Blakey and Parnell, 1995; Dickinson et al., 2010). The Carmel Formation preserves a record of shallow marine, sabkha, and fluvial settings that intertongue with aeolian Page accumulations across a belt ~ 75 km wide that runs parallel to the paleocoastline (Havholm et al., 1993; Blakey et al., 1996; Taggart et al., 2010). Intertonguing of the Carmel coastal complex with the western

part of the Page Sandstone has been interpreted to represent the interplay between tectonic subsidence in the Utah-Idaho trough, and changes in sediment supply and sea level (Blakey et al., 1996).

The Page Sandstone is separated from the underlying Navajo Sandstone by the J-2 surface, one of six regional unconformities formed across the greater Colorado Plateau during the Jurassic (Pipiringos and O’Sullivan, 1978). The J-2 surface near Page,

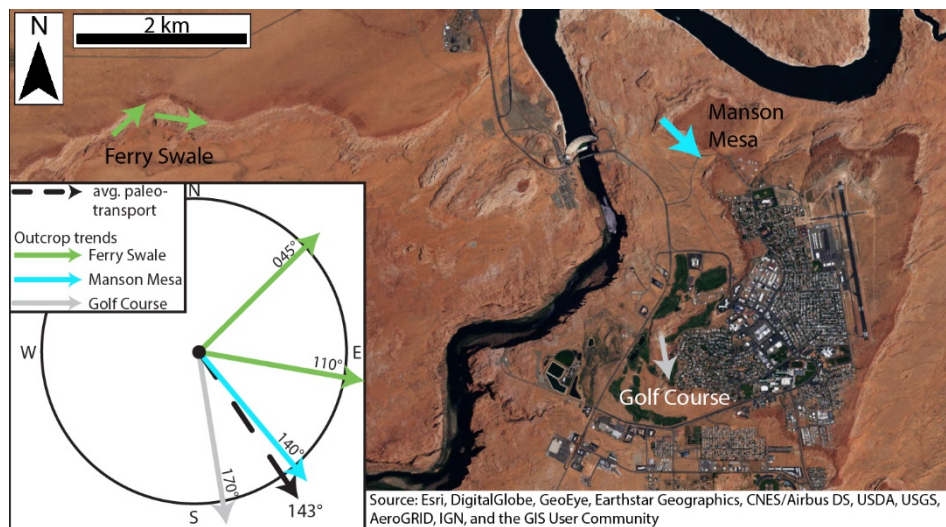


Figure 4.2 Study area near Page, Arizona, marked by the black star in Figure 4.1A. The three outcrops are labeled as Ferry Swale, Manson Mesa, and Golf Course. The associated arrows (green, teal, and white) give the general trends of the outcrop walls, as well as the trends used to create the cross-sections (Figs. 4.4-4.5 and A.1-A.3). In the bottom left corner, the trends of those walls are compared to the average paleo-transport direction within the Page (black dashed arrow; $n = 90$). The western wall of the Ferry Swale outcrop is perpendicular to the average paleo-transport direction, the eastern wall of the Ferry Swale outcrop is oblique, and the Manson Mesa and Golf Course outcrops are near parallel to paleo-transport.

Arizona, is characterized by large polygonal fractures, diagenetic chert nodules, and meters of erosional relief (Pipiringos and O’Sullivan, 1978; Kocurek and Hunter, 1986; Swezey,

1991; Kocurek et al., 1991). The Page is overlain by the Carmel Formation, representing eastward migration of the Carmel fluvial and coastal complex (Blakey et al., 1996).

Previous work has produced hundreds of correlated vertical sections across the entirety of the Page Sandstone (Havholm, 1991; Kocurek et al., 1991; Havholm et al., 1993; Jones and Blakey, 1993; Havholm and Kocurek, 1994; Blakey et al., 1996). The Page has been informally divided into a basal, lower, middle, and upper unit by Havholm et al. (1993), and these divisions correlate with formal stratigraphic names used by Blakey et al. (1996) (Fig. 4.1B). The informal units were defined using formation-scale, erosional bounding surfaces. These surfaces are characterized by polygonal fractures, interpreted as having developed in evaporite-cemented sand, and/or overlying wavy bedding interpreted as sabkha deposits (Kocurek and Hunter, 1986; Havholm et al., 1993; Havholm and Kocurek, 1994). Together these features have been used as proxies for the paleo-water table (i.e., “Stokes surfaces” of Fryberger et al., 1988; “super surfaces” of Kocurek, 1988). Each of these surfaces can be traced westward to a point where they are overlain by transgressive tongues of Carmel strata (Havholm et al., 1993; Havholm and Kocurek, 1994; Blakey et al., 1996) (Fig. 4.1B). Because these transgressive tongues represent relative high stands of the Carmel sea and their correlative inland surfaces are marked by features associated with the water table, the formation-scale surfaces are interpreted to define the elevation of the coastal water table, which rose in response to the adjacent sea-level rise (Havholm and Kocurek, 1994; Blakey et al., 1996; Kocurek et al., 2001). The surfaces themselves are interpreted as having been formed by deflation down to the water table during relative high stands in sea level when sediment availability was limited. Conversely,

the Page dune systems are thought to have developed during low stands in sea level that afforded greater availability to coastal sand. Each package of Page strata bounded by the interpreted deflationary surfaces is therefore inferred to represent an aeolian sand body accumulated during a low stand and preserved as a consequence of a rising continental water table that protected it from wind-blown deflation. The thickness of any preserved accumulation reflects the cumulative effects of subsidence and relative sea-level rise, as reflected in the continental water-table paleo-elevation (Havholm and Kocurek, 1994; Blakey et al., 1996).

There is now consensus that episodic change in paleo-water table elevation represented a changing allogenic boundary condition of the Page dune fields (Havholm et al., 1993). What is not fully known, however, are the signatures of autogenic processes versus allogenic forcings recorded by the stacked sets of cross-strata housed between the major transgressive surfaces. Its well-documented paleo-environmental context, together with the excellent 3-D exposures accessible around Page, Arizona, make the Page Sandstone an ideal unit for the study of the autogenic processes and allogenic forcings encoded in aeolian stratigraphy.

4.1.2 Aeolian stratification types

Aeolian cross-strata are composed of grainfall, grainflow, and wind-ripple deposits (Hunter, 1977). Grainfall deposits accumulate when a significant fraction of saltating grains bypass the dune brink and rain down onto the lee faces of dunes. Grainfall deposits are typically thickest immediately downwind from the brink, and they thin with distance

down the lee face. Because of this thickness distribution, the uppermost lee slope progressively steepens until the angle of initial yield is reached, triggering an avalanche, or grainflow (Allen, 1970a; Hunter, 1977; Kocurek and Dott, 1981; McDonald and Anderson, 1995; Nield et al., 2017) that redistributes sediment down the lee face of the dune. Grainflows and their deposits occur primarily along parts of the lee face aligned close to perpendicular to the sediment-transporting wind direction (Eastwood et al., 2012). Both grainflow and grainfall deposits are commonly reworked by wind-ripples that migrate along lee-face segments obliquely oriented to the regional wind direction (Eastwood et al., 2012) and in the process generate wind-ripple laminae (Hunter, 1977).

Aeolian cross-strata are commonly composed of alternating packages of grainflow deposits and wind-ripple laminae, representing seasonal changes in wind direction and/or changes in dune shape and crest orientation (Hunter and Rubin, 1983). Because aeolian sets of cross-strata typically represent only the basal parts of dune lee faces, grainfall deposits are less frequently preserved in sets representing large dunes (Kocurek and Dott, 1981). Grainfall deposits are, however, common in cross-strata representing small dunes, where the grainfall apron extends to the bases of dunes (Kocurek and Dott, 1981).

4.1.3 Aeolian set architecture

The architecture of aeolian sets of cross-strata present between outcrop-scale bounding surfaces preserve a record of dune-field kinematics. Schematic illustrations of set architectures are shown in Figures 4.3A-C (based on diagrams from Allen, 1970b; Rubin and Hunter, 1982). In cases where trains of migrating dunes climb over the accumulations

of downwind dunes, set boundaries are expected to originate from a lower, outcrop-scale bounding surface and climb at some measurable angle (Fig. 4.3A). In cases where sets are migrating down into and in the process filling pre-existing topographic lows, the architecture is defined by set boundaries that originate from an upper, outcrop-scale bounding surface and descend, ultimately downlapping onto a lower, outcrop-scale bounding surface that hosts the antecedent topographic low (Fig. 4.3B). Finally, in cases

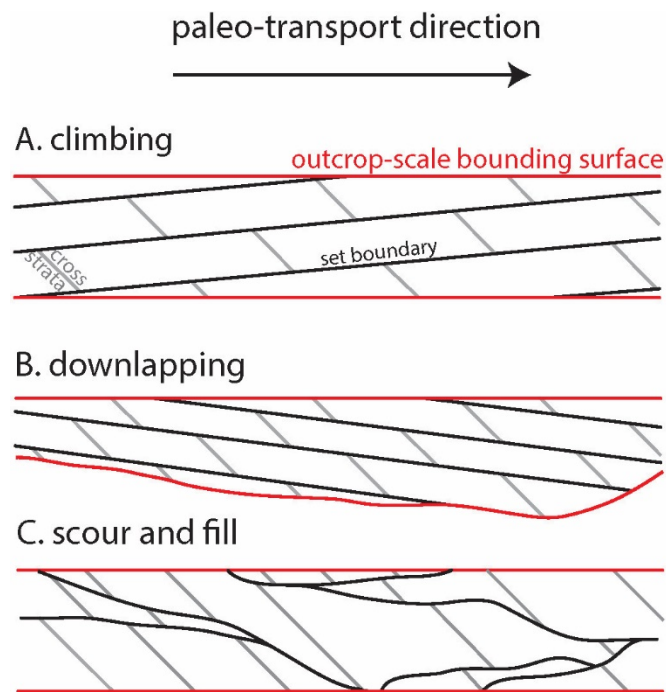


Figure 4.3 Schematic showing (A.) climb, (B.) downlap, and (C.) scour-and-fill architectures of aeolian cross-sets. The black arrow at the top indicates paleo-transport is from left to right in each case. Cross-strata, set boundaries, and outcrop-scale bounding surfaces are all indicated and consistent between diagrams. A moderate vertical exaggeration is used to accentuate boundary dips. Schematics based on illustrations from Allen (1970a) and Rubin and Hunter (1982).

where variable depth of trough scouring creates space that is later filled by smaller dunes in the train, sets boundaries persist for limited distances before being cut out by other set boundaries rather than by outcrop-scale bounding surfaces (Fig. 4.3C).

The architecture or geometries of set boundaries are not the only data type used here to reconstruct the filling history. Distributions on set thickness also contain information on how the stratification formed (Paola and Borgman, 1991; Bridge, 1997; Bridge and Best, 1997; Jerolmack and Mohrig, 2005; Ganti et al., 2013). In particular, distributions of cross-strata produced by the scour-and-fill process (Fig. 4.3C) record an asymptotically high value for the coefficient of variation (standard deviation divided by the mean) of set thicknesses, while sets produced during net bed aggradation (both the climbing and downlapping cases in Figs. 4.3A, B) have distinctly smaller values for the coefficient of variation associated with set-thickness distributions (Jerolmack and Mohrig, 2005).

4.2 METHODS

4.2.1 Field Work

Three outcrops in and near Page, Arizona, were selected based upon their accessibility and orientation relative to the paleo-transport direction determined from a measured distribution of cross-strata dip directions (Fig. 4.2). The Ferry Swale outcrop was split into two sections, one segment oriented perpendicular to the general dune migration direction and the other oblique to the dune migration direction. The Manson Mesa and Golf Course sections were oriented roughly parallel to the transport direction. Cross-strata set

boundaries and outcrop-scale bounding surfaces were surveyed using a total station at each outcrop location. A coordinate was recorded at each base station using GPS so that all surveyed points could be converted to UTM coordinates. Each outcrop-scale erosional surface was then correlated with vertical sections from Havholm (1991). In addition to mapping surfaces, 90 measurements of foreset dip direction were taken using a Brunton compass and averaged with the Circular Statistics Toolbox in MATLAB (Berens, 2009). Thicknesses of 124 cycles of wind-ripple and stacked grainflow strata were collected from cross-strata. All of these measurements were collected from the basal Page (PB), lower Page (PL), and middle middle Page (PMm) intervals of the Page Sandstone (Fig. 4.1B). For simplicity, we will refer to the middle middle Page as the middle Page. These divisions make up the strata bounded by the underlying J-2 and overlying S-rm surfaces (Fig. 4.1B). The upper Page, unit PUI of Figure 4.1, is composed of sets of compound-dune cross-strata that are distinctively different from those of the underlying units and are not part of this study.

4.2.2 Data processing

Combining field maps with GPS datums and annotated total-station points, a digital GIS project including all of the outcrop locations was constructed. Continuous topographic surfaces were interpolated from point data defining each outcrop-scale bounding surface and cross-strata set boundary using a Kriging method that completely preserves input data. The spatial resolution for resulting digital elevation models (DEMs) at Manson Mesa, the Golf Course, and Ferry Swale was 0.55 m, 0.65 m, and 2 m, respectively.

Using the GIS, vertical stratigraphic sections were constructed at 20 m intervals across each outcrop. The 3-D mapping data allowed surfaces in each cross section to be accurately correlated. Measurements of set thickness and outcrop-scale bounding-surface relief were made from the generated cross sections. Set geometry and its relationship to the nearest bounding surface were also categorized from the cross sections (Fig. 4.3).

4.2.3 Numerical modeling

Swanson et al. (accepted) numerically model the production of cross strata by coupling bed topography with bed shear stress and sediment transport for long trains of aeolian dunes. Using this model, synthetic stratigraphy hosting several outcrop-scale bounding surfaces has been created in a 2-D panel. Observations from scenarios producing this synthetic stratigraphy are compared to outcrop interpretations (model parameters in Table A.1.) To create the synthetic Page stratigraphy, a dune field and its accumulations are developed for a set period of time during which an initial rough surface develops into small, early-phase dunes, which develop into larger, more mature dunes. Following that time, the up-wind sediment supply is cut off and erosion is limited to an elevation above the initial surface, causing a relatively flat outcrop-scale bounding surface to develop where the dune field had been. Re-establishment of the upwind sand supply promoted development of another dune field and its accumulations on top of this outcrop-scale bounding surface. In total, four episodes of aeolian accumulation are modeled in this scenario. This particular set of boundary conditions was set up to answer Page-specific

questions not addressed in the companion paper (Swanson et al., accepted), demonstrating the flexibility of the numerical model.

4.3 RESULTS

4.3.1 Outcrop-scale architecture

At the three outcrops (Figs. 4.4, 4.5, A.1-A.3) the Page Sandstone is composed of packages of aeolian cross-strata partitioned by the formation-scale surfaces of Havholm et al. (1993). In the studied interval spanning from the J-2 to the S-rm surfaces (Fig. 4.1), the Page ranges from 25 to 45 m and is composed largely of meter-scale beds of cross strata in the lower and middle Page (Fig. 4.6A), with local preservation of thinner sets in the basal Page (Figs. 4.7A, 4.8A-D). The lower Page consists of a single coset that either sits above the basal Page or directly on the J-2 surface. It is observed primarily at the Ferry Swale outcrop (Figs. 4.4, 4.5, A.1), with minimal exposure at Manson Mesa (Fig. A.2) and no exposure at Golf Course (Fig. A.3). In addition to the formation-scale surfaces that define the informal Page units, Havholm et al. (1993) identified less-continuous surfaces that are typically truncated laterally. For this study, the term “outcrop-scale bounding surface” refers to both the formation-scale and less-continuous super surfaces identified by Havholm et al. (1993).

4.3.2 Outcrop-scale bounding surfaces

Figures 4.4, 4.5, and A.1-A.3 present the structure of the outcrop-scale bounding surfaces surveyed at the three outcrop locations (Fig. 4.2). The J-2 surface is characterized by wedge-shaped fractures into the underlying Navajo Formation, pebble-size, diagenetic

chert nodules replacing evaporites in the uppermost Navajo strata, and up to 10 m of local erosional relief (e.g., Ferry Swale; Fig. A.1). The outcrop-scale bounding surfaces in the lower and middle Page also preserve erosional relief that varies between 1.2 m and 13.5 m (Fig. 4.9A). On both walls of the Ferry Swale outcrop (Figs. 4.4, 4.5), this relief has a scalloped geometry. Horizontal distances from the adjacent high points on either side of a scallop were measured on the western, perpendicular-to-transport wall (Fig. 4.4). The widths of sets filling these scallops were measured on the same wall as the horizontal distance between pinchouts. Scallop widths ($n = 23$) have a mean value of 72 m and a standard deviation of 34 m. Sets filling these scallops ($n = 33$) have a similar mean width of 64 m and a greater standard deviation of 81 m. Outcrop-scale bounding surfaces are commonly associated with two unique deposit types. Wavy-laminated sandstones with variable thicknesses ranging up to 0.4 m occur discontinuously along outcrop-scale bounding surfaces in the lower and middle Page (Figs. 4.10A-D). In the basal Page, the wavy-laminated sandstones were identified both overlying the J-2 surface and in between aeolian cross-sets, and these strata are generally thicker and more continuous than in the higher Page units. As a whole, the red, wavy-laminated strata have been interpreted as sabkha deposits that formed along surfaces deflated to the near-surface water table (Havholm et al., 1993; Havholm and Kocurek, 1994). The second deposit type associated primarily with outcrop-scale bounding surfaces are prominent, wedge-shaped fracture fills. In exposures that provide cross-sectional views, the fractures crosscut sets of cross-stratified sandstone (Figs. 4.11A-C). These fractures narrow downward, although not always in a linear fashion. In plan view, the fracture fills take a more polygonal shape (Fig.

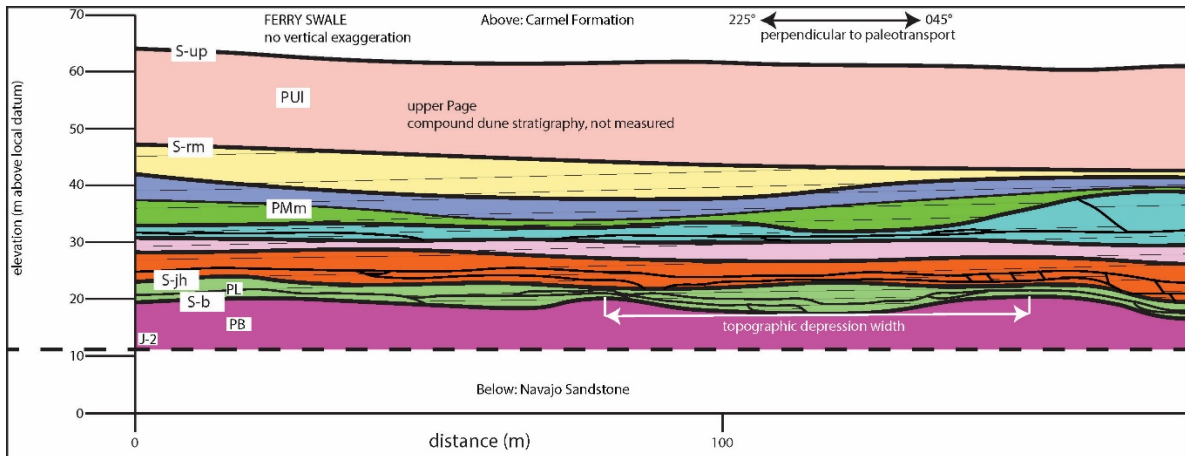


Figure 4.4 Excerpt of the perpendicular-to-transport wall of the Ferry Swale cross-section (Fig. A.1). Location shown in Figure 4.2. There is no vertical exaggeration. Outcrop-scale bounding surfaces are represented by bold black lines separating outcrop-scale packages of cross-strata of different colors. Black lines within outcrop-scale packages represent cross-set bounding surfaces. Dipping gray lines represent the apparent dip direction of the mean Page transport direction. Colors are used to identify packages of cross-strata separated by outcrop-scale surfaces, and the colors do not necessarily represent correlations between outcrops. The major surfaces are S-up, S-rm, S-jh, and S-b from Havholm et al. (1993). Informal Page units are composed of one to several outcrop-scale packages separated by the outcrop-scale surfaces, and are labeled as in Havholm et al., (1993): PB (basal Page), PL (lower Page), PMm (middle middle Page), and PUI (lower upper Page). The PUI, colored peach, is composed of compound dune deposits, and not studied here. The basal Page (PB) is preserved above the J-2 at this location, and pinches out toward the east (Fig. 4.5). It is not uncommon for an outcrop-scale package to be composed of one to a few sets, and to vary in number of sets and set thickness laterally. Outcrop-scale bounding surfaces have meters of relief at this location. The width of a scallop in outcrop-scale bounding surface relief is demonstrated with white double-headed arrow.

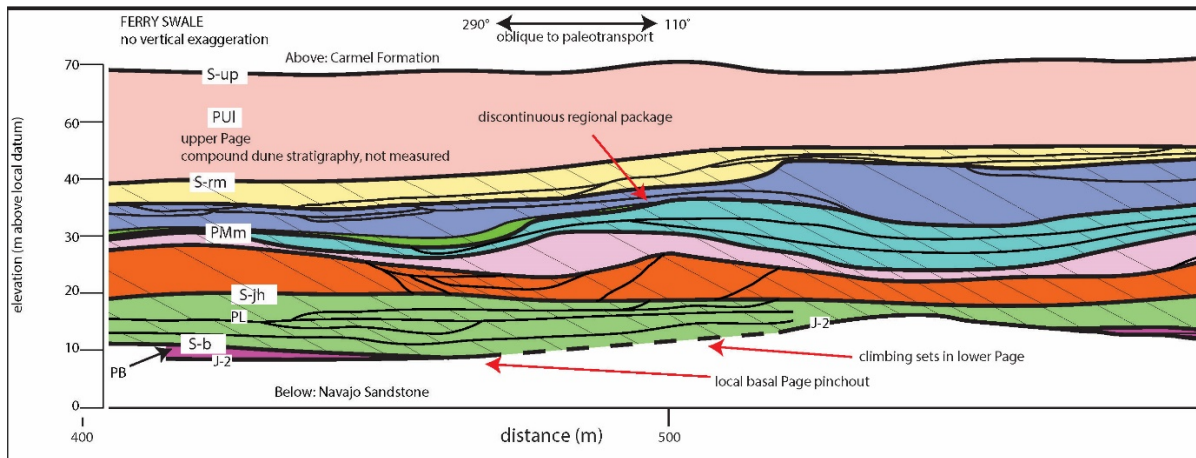


Figure 4.5 Excerpt of the near oblique-to-transport wall of the Ferry Swale cross-section (Fig. A.1). Location shown in Figure 4.2. Symboly is the same as in Figure 4.4. Toward the western portion of this section, the basal Page (PB) pinches out along the rising J-2 surface. East of that point, the lower Page sits directly upon the J-2 surface. The location of amalgamation between two outcrop-scale packages is shown with a red arrow. Note the scalloped shape of the outcrop-scale surfaces and the variability in set thickness and discontinuity of sets.

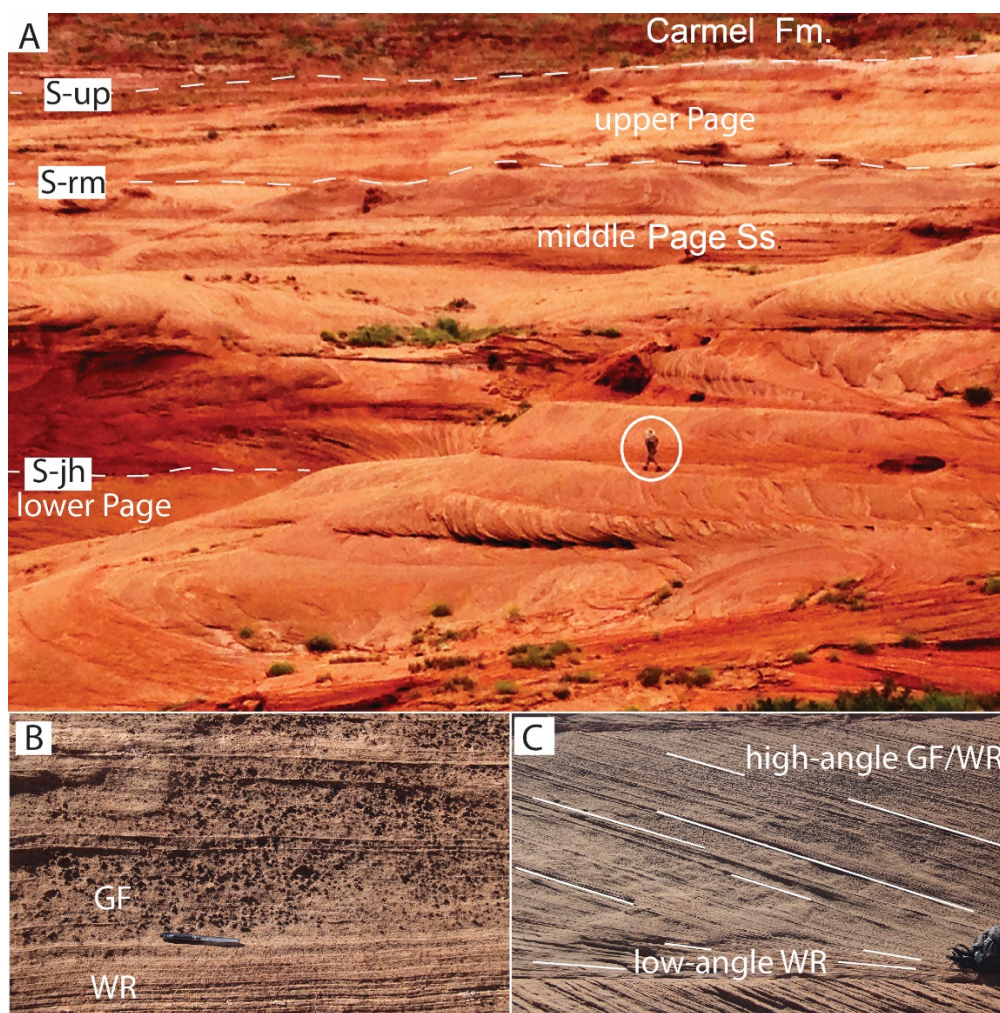


Figure 4.6 A: Typical cross-strata composing the lower and middle Page Sandstone. Major regional bounding surfaces are marked, as is the Carmel Formation. Person for scale is circled. Photograph from the Ferry Swale outcrop. Contrast is stretched to highlight set boundaries and cross-strata in the foreground. B: Planform view of typical arrangement of stratification types in sets of the lower and middle Page. Amalgamated grainflow strata (GF) alternate with wind-ripple laminations (WR). Individual grainflow deposits in these packages are generally not identifiable. Rough texture is from concretions frequently associated with the grainflow strata, but not the wind-ripple laminations. Pen for scale. C: High-angle cross-strata composed of alternating textured grainflow strata and wind-ripple laminations transitioning into low-angle wind-ripple strata near the lower bounding surface. Selected cross-strata are mapped in white to highlight this transition. Backpack for scale.

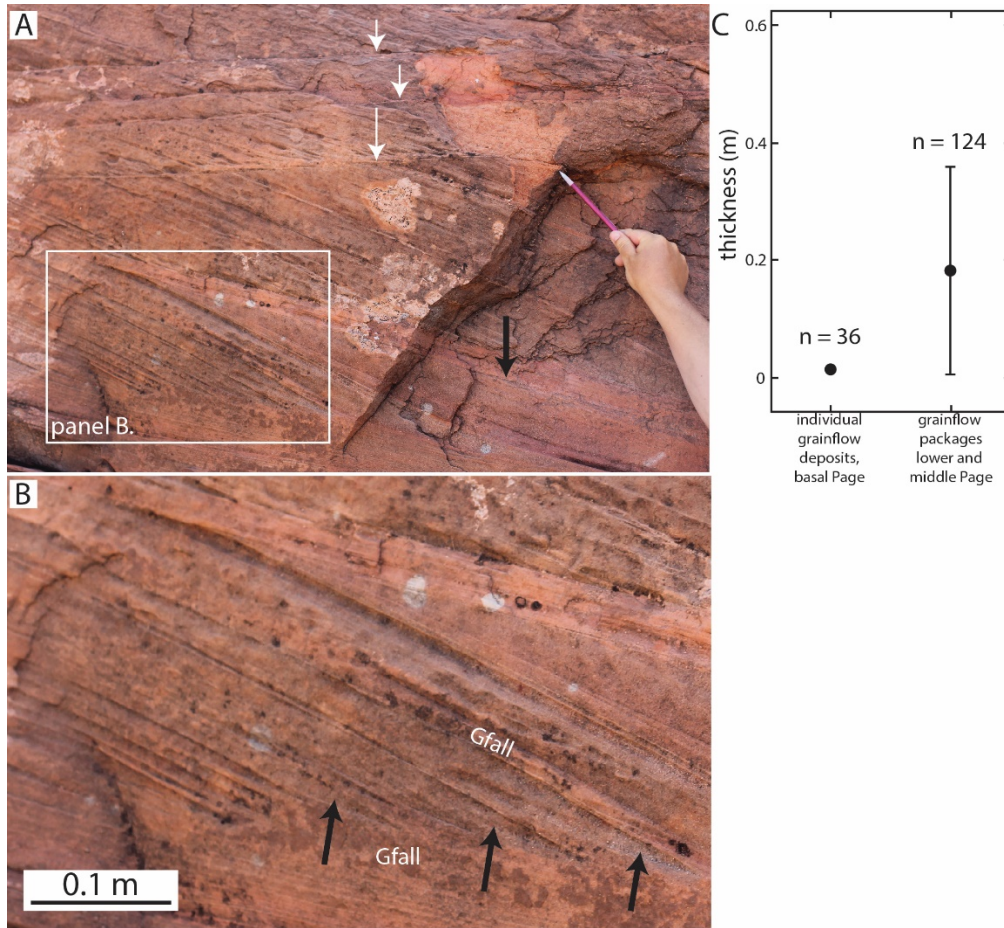


Figure 4.7 A: Close-up of the basal Page sets of cross-strata at the Golf Course outcrop. White arrows point to set bounding surfaces. The black arrow points to a reactivation surface within the set, representing a period of lee face erosion bound by packages representing lee face deposition. The deposit is composed of sets averaging 0.16 m in thickness with individual grainflow deposits separated by thin, tabular beds interpreted as grainfall deposits. The location of panel B is shown with the white box. Pencil for scale. B: A zoom in to part of panel A. Unlike the lower and middle Page sets, individual grainflow deposits are identifiable. Black arrows point to the bottoms of grainflow deposits featuring the characteristic blade shape. Finer-grained grainfall deposits are labeled between and at the base of grainflows, and help distinguish the coarser-grained grainflow deposits. C: Plot comparing the means (circles) and the standard deviations (bars) of thicknesses of individual grainflow deposits in the basal Page to grainflow packages in the lower and middle Page. The standard deviation of individual grainflow deposits in the basal Page is below the size of the circle.

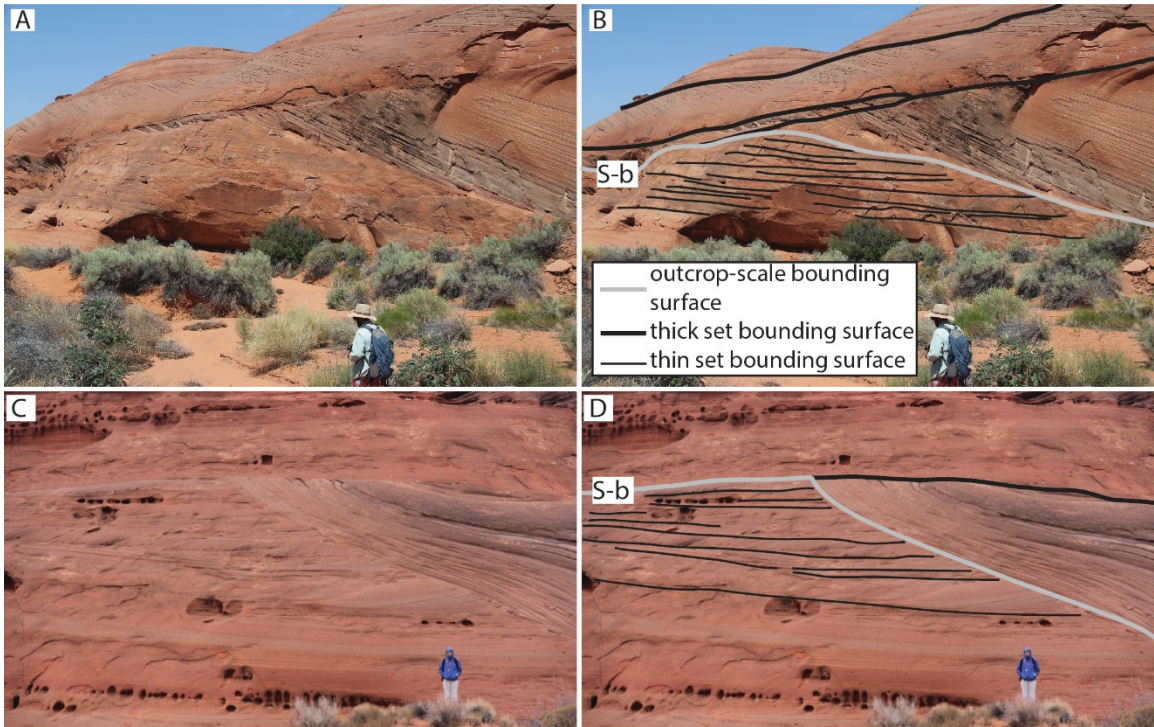


Figure 4.8 A: This location is ~100 m north of the Golf Course outcrop. About 5 m of vertical section composed of stacked, relatively thin sets interpreted as basal Page (Fig. 4.7A-B) truncated by the scour associated with the lower Page. B: Interpreted photograph with the S-b outcrop-scale bounding surface, bounding surfaces of large sets of cross-strata, and bounding surfaces of thin sets of cross-strata mapped. Basal Page is an interpretation, as there is no local exposure of J-2 relief. C: Ferry Swale outcrop. Stacked sets of thin basal Page cross-strata truncated by a scour into the S-b during a later episode of sedimentation. This location is above a 10 m depression in J-2 relief (location in Fig. A.1). D: Selected bounding surfaces superimposed onto the photograph. Key is the same as in panel B.

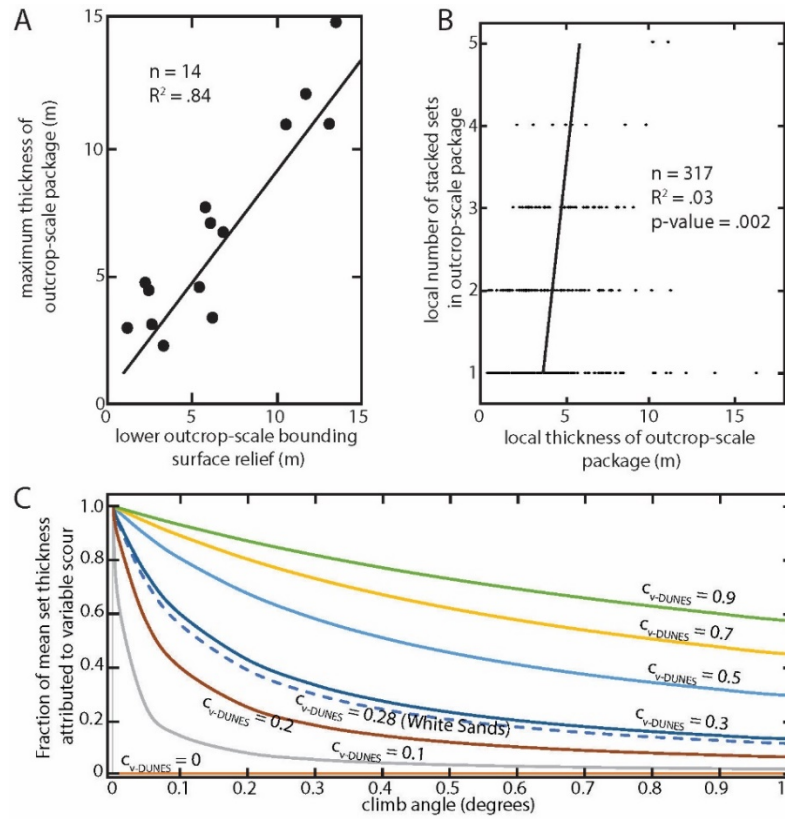


Figure 4.9 A quantification of set architecture composing outcrop-scale packages. A: Total relief along an outcrop-scale bounding surface plotted against the maximum thickness of the outcrop-scale package above the measured surface. The linear fit is significant with a positive slope of 0.87, indicating that basal relief controls the preserved thickness of the package. B: The number of sets bound by adjacent outcrop-scale bounding surfaces at a given location plotted against the thickness of the package at that same location. The best-fit linear trend is not significant, indicating that the number of sets does not control the package thickness. C: Climb angle plotted against the contribution of variable scour to the mean set thickness based on the coefficient of variation of dune height ($c_{v-DUNES}$). Colored lines represent dune height coefficients of variation. At low climb angles, variation in dune height and the subsequent variation in dune scour depths are a dominant control on mean set thickness. An increase in climb angle and/or a decrease in the standard deviation of dune sizes decreases the effect of variable scour on mean set thickness. The fraction of set thicknesses attributed to variable scour depth is calculated for White Sands based on information in Baitis et al., (2014). Calculated from Bridge and Best (1997) using mean height and celerity values of dunes at White Sands (Baitis et al., 2014).

4.11A). Sandstone fill within the fractures is vertically laminated or structureless (Figs. 4.11B, C). The tops of the wedges end against outcrop-scale bounding surfaces. These sandstone wedges have been interpreted as sand-filled, evaporite-cemented thermal contraction polygonal fractures (Kocurek and Hunter, 1986).

4.3.3 Cross-set architecture

The outcrop-scale bounding surfaces truncate and bound packages of cross-stratified beds, referred to hereafter as “outcrop-scale packages.” In these packages, individual sets of cross-strata are defined by upper and lower set boundaries that are less continuous than the outcrop-scale surfaces. The architecture of outcrop-scale packages varies between the basal, lower, and middle Page.

4.3.3.1 Basal Page architecture

The thin sets of cross-stratified sandstone (Fig. 4.7A, B) are relatively uncommon and limited to the basal Page at the outcrops studied. Set thicknesses range from 0.03 to 0.45 m with a mean of 0.16 m and a standard deviation of 0.10 m (Figs. 4.12A, B; n = 80). Individual grainflow deposits are well defined by their characteristic blade shape and are separated by millimeters-thick grainfall deposits (Fig. 4.7B). Alternating grainflow and grainfall deposits characterize the cross-stratification in these sets. The mean grainflow deposit thickness is 18 mm with a standard deviation of 9 mm (Fig. 4.7C; n = 36).

In contrast to the lower and middle Page, the sets of the basal Page are stacked tens of sets high to form packages several meters thick. This architecture occurs at Ferry Swale

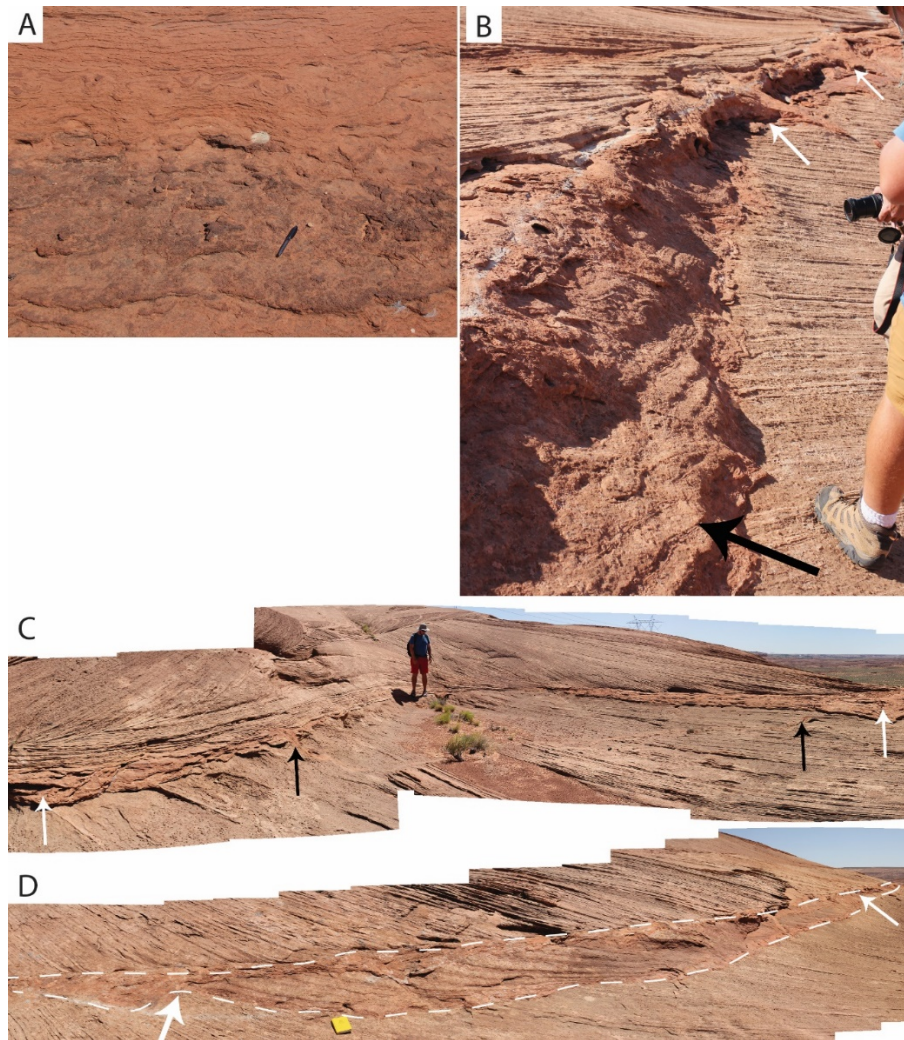


Figure 4.10 A: Wavy-laminated to contorted sandstone beds interpreted as sabkha deposits. Pen for scale. B: Black arrow points to a thick sabkha deposit along an outcrop-scale bounding surface separating sets of cross-strata. Associated polygonal fractures are visible in the background (white arrows). C: An outcrop-scale bounding surface with variably-thick sabkha deposits. White arrows show the locations with the thickest sabkha deposits. Thickness thins to zero at the person. Black arrows point to polygonal fractures associated with the outcrop-scale bounding surface. From the Ferry Swale outcrop, D: An outcrop-scale bounding surface with a laterally-discontinuous set of cross-strata incorporated into a sabkha deposit (outlined in dashed white lines). White arrows point to the ends of the set of cross-strata. This is an unusual outcrop, and only observed at this location at the Ferry Swale outcrop. Yellow field book for scale.

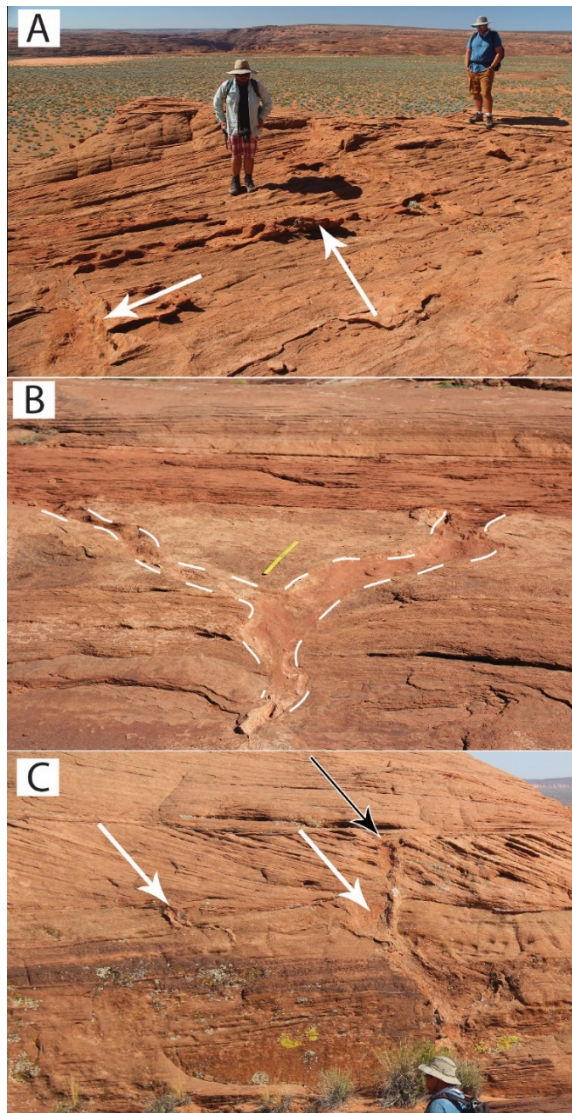


Figure 4.11 Variability of sandstone wedges. A: Topographically-inverted polygonal fractures (white arrows) displaying as raised polygons along a planform exposure of an outcrop-scale bounding surface. B: Two negative relief sandstone wedges intersecting on a shallowly-dipping surface. Wedges are outlined with dashed white lines. Meter stick for scale. C: Sandstone wedges associated with two separate outcrop-scale bounding surfaces at the Ferry Swale outcrop (the two laterally amalgamating surfaces pointed out in Fig. 4.5). The black arrow marks the origin of a sandstone wedge at the higher outcrop-scale bounding surface, which cuts beyond the lower outcrop-scale bounding surface. The white arrows mark the origin of sandstone wedges at the lower outcrop-scale bounding surface.

and north of the Golf Course outcrop (Figs. 4.8A-D, 4.13). At the Ferry Swale outcrop, these thin sets are located filling a local J-2 depression (Fig. A.1 shows full J-2 topography at Ferry Swale). North of the Golf Course outcrop, basal Page sets probably also fill a depression on the J-2 surface, but the contact with the Navajo is not exposed. At both locations, these packages of stacked, thin sets are laterally scoured and filled by thicker sets of the lower Page (Figs. 4.8A-D, 4.13). The stacked, thin sets of the basal Page are the focus of our comparison between the basal Page and the lower and middle Page. Parts of the basal Page consisting of alternating sabkha and cross-set deposits (Havholm et al., 1993) were not analyzed here.

4.3.3.2 Lower and middle Page architecture

The predominant facies composing the lower and middle Page at all three sites (Fig. 4.2) are thick sets of cross-stratified sandstones (Fig. 4.6A) consisting of stacked grainflow strata separated by intervals of wind-ripple laminae (Fig. 4.6B). Individual grainflow deposits could not be distinguished, but rather amalgamations of many grainflow deposits were observed. Where grainflow cross-strata do not extend to the base of the set, lower-angle wind-ripple strata were found (Fig. 4.6C). The lower Page has a mean set thickness of 1.61 m and a standard deviation of 0.79 m ($n = 59$; Fig. 4.12A, C). Sets of cross-strata from the middle Page are on average 2.44 m thick, and occasionally exceed 10 m. The standard deviation of set thicknesses is 2.20 m ($n = 402$; Fig. 4.12A, D). In both the lower and middle Page, the thickness of individual sets is laterally variable at the outcrop scale

(Figs. 4.4, 4.5), because sets are typically truncated by adjacent sets of cross-strata, limiting their lateral continuity (Fig. 4.14A, B). The thicknesses of amalgamated grainflow deposits were measured from several sets of these cross-strata (e.g., Fig. 4.6B), and range from 0.01 to 1.30 m with a mean and standard deviation both equal to 0.19 m ($n = 124$; Fig. 4.7D). Ninety measurements of foreset dip direction were taken from this facies and serve as a proxy measurement of paleo-transport direction. The mean of these measurements is 143° with a standard deviation of 42° .

The number of sets stacked between outcrop-scale surfaces at any vertical section of the lower and middle Page ranges from 1 to 5 (Figs. 4.4, 4.5, A.1-A.3). There is not a strong correlation between the number of stacked sets and section thickness (Fig. 4.9B). There is, however, a strong correlation between the thickness of an outcrop-scale package and the total relief associated with the lower outcrop-scale bounding surface (Fig. 4.9A); the line fitted to these data has a slope of 0.87.

Using the cross sections created for each outcrop (Figs. 4.4, 4.5, A.1-A.3), each coset from the lower and middle Page was placed into one of the architectural categories defined in Figure 4.3. These categories describe parallel-to-transport set architectures, so sets in the perpendicular-to-transport wall of Ferry Swale are not addressed here. The oblique-to-transport wall of Ferry Swale was assumed to exhibit these characteristics well enough that those sets are included in the count. Discontinuous, truncated sets fitting the scour-and-fill architecture occur most frequently, although all architectural categories are identified in outcrop (Fig. 4.15). We note that five of the nine climbing sets (Fig. 4.3A) are

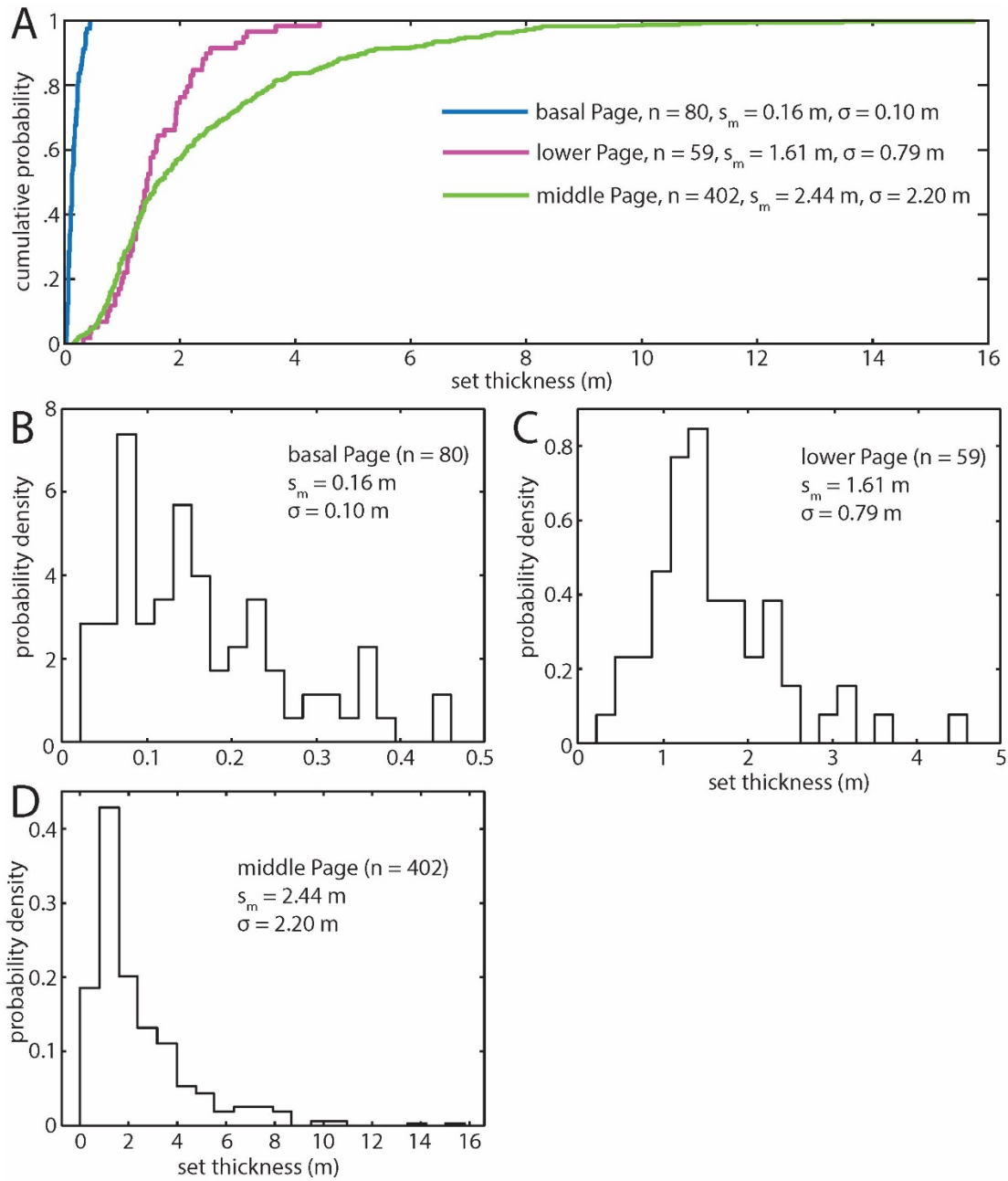


Figure 4.12 A: Comparison of the cumulative distribution functions (CDFs) of the basal, lower, and middle Page set thicknesses, along with statistical moments. Basal sets are much thinner, and middle Page sets cover a much wider range than the lower and basal Page. B-D: Probability density histograms showing set thickness distributions of the basal (B), lower (C), and middle (D) Page.

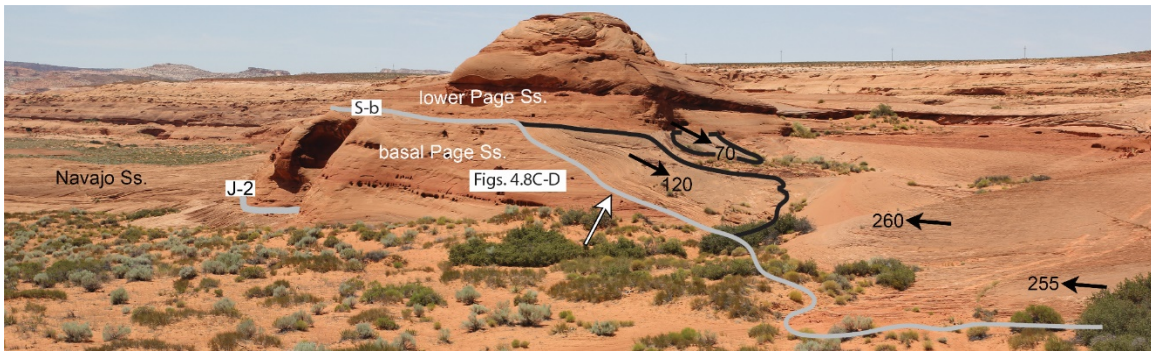


Figure 4.13 Location featuring a topographic depression in the J-2 surface at Ferry Swale, and a subsequent partial scouring of early-phase basal Page accumulations (Fig. A.1). The J-2 is mapped with a thick grey line, separating the Navajo from the basal Page. Scour surfaces bounding thick grainflow deposits are mapped with black lines. Black arrows show cross-strata dip directions. The stacked thin sets shown in Figures 4.8C-D are labeled, and are truncated by a scour into the S-b surface dipping towards 120°, shown by the white arrow. Adjacent grainflow strata dip toward 70°. Wind-ripple strata dip towards 260° and 255°, nearly 180° different than the grainflow strata and over 100° different from the regional average transport direction. The center location is interpreted as the deepest portion of a lower Page scour into the S-b surface that partially cannibalized early-phase basal Page.

located within the lower Page where the lower Page sits directly above the J-2 surface (Fig. 4.5).

4.3.4 Results of numerical modeling

Several observations provided by results from the numerical model are particularly relevant for interpreting the Page strata (Fig. 4.16). Firstly, the four episodes of aeolian accumulation modeled in this scenario produce four distinct packages of cross-sets separated by domain (outcrop)-scale bounding surfaces. Secondly, the relief along the modeled outcrop-scale bounding surfaces develops coevally via dune scouring with the

development of the dune field during each phase of aeolian sedimentation. Thirdly, this relief is filled with the accumulations of the relatively late-phase dunes associated with the creation of the scour relief. Fourthly, except for antecedent topographic lows sequestering accumulations beneath the trough-scouring depths of late-stage dunes, there is almost no preservation of strata representing the early phases of the dune fields.

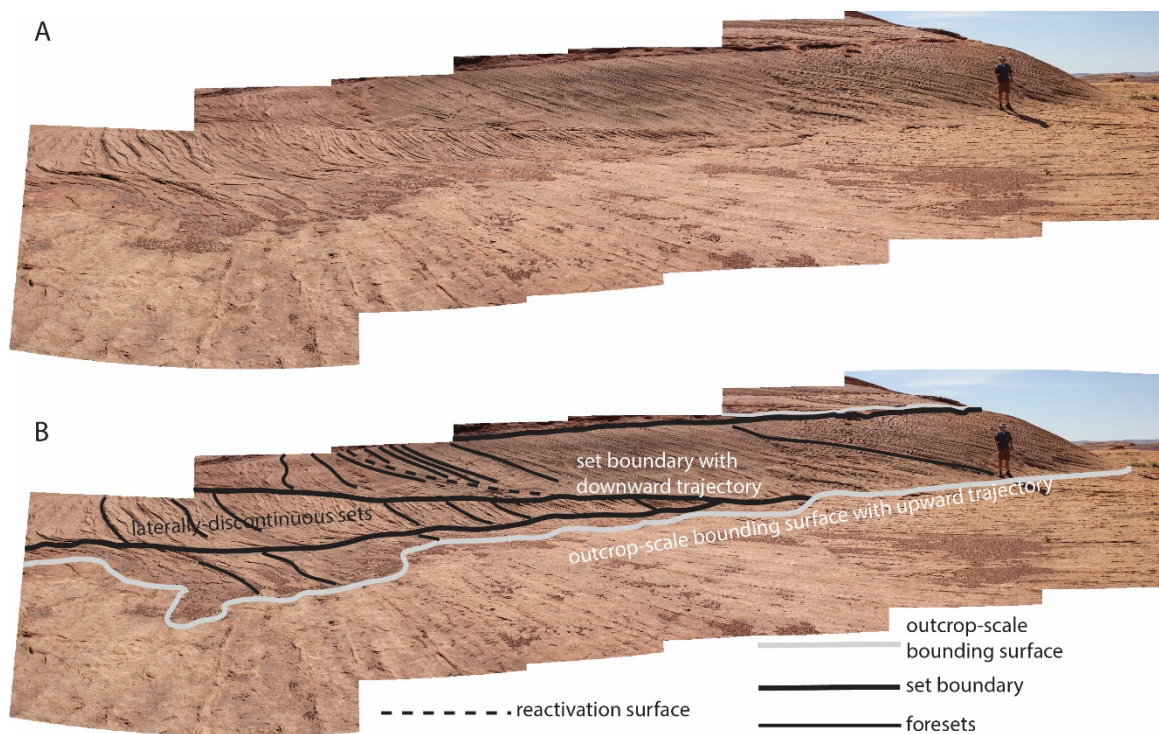


Figure 4.14 A: A set of cross-strata of the middle Page with a lower bounding surface with a downward trajectory, truncating two lower sets of cross-strata within the same outcrop-scale package. B: Interpreted panorama with mapped outcrop-scale bounding surfaces, set bounding surfaces, and a reactivation surface, which represent a period of lee face erosion between periods of lee face deposition. A thin set runs just below the upper outcrop-scale bounding surface. This serves as an example of a scour-and-fill geometry, variable set thickness, and an entire outcrop-scale package defined by only 2-4 stacked sets.

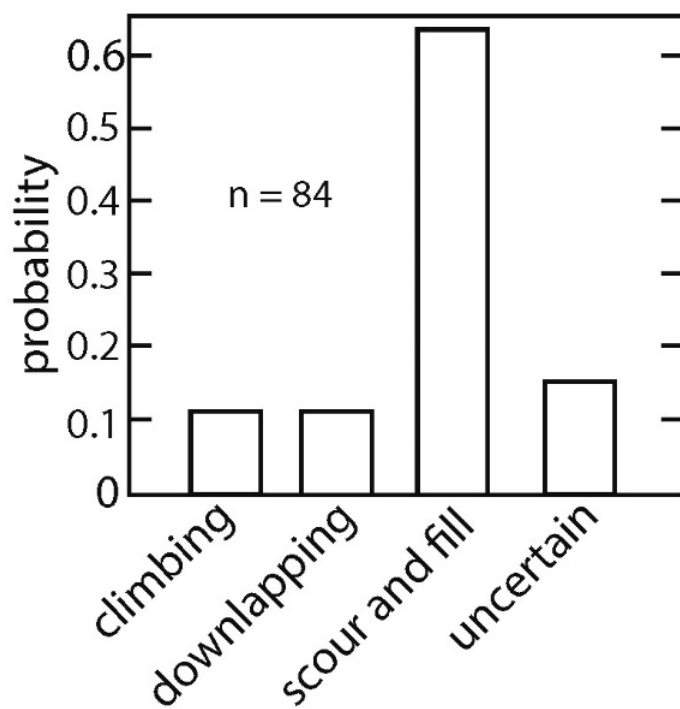


Figure 4.15 Histogram showing the occurrence of architecture types in the Page Sandstone (Fig. 4.3). The most frequently observed geometry is scour-and-fill. This analysis does not include the western wall of Ferry Swale (Fig. 4.4) because it is perpendicular to transport direction and does not fit the models in Figure 4.3.

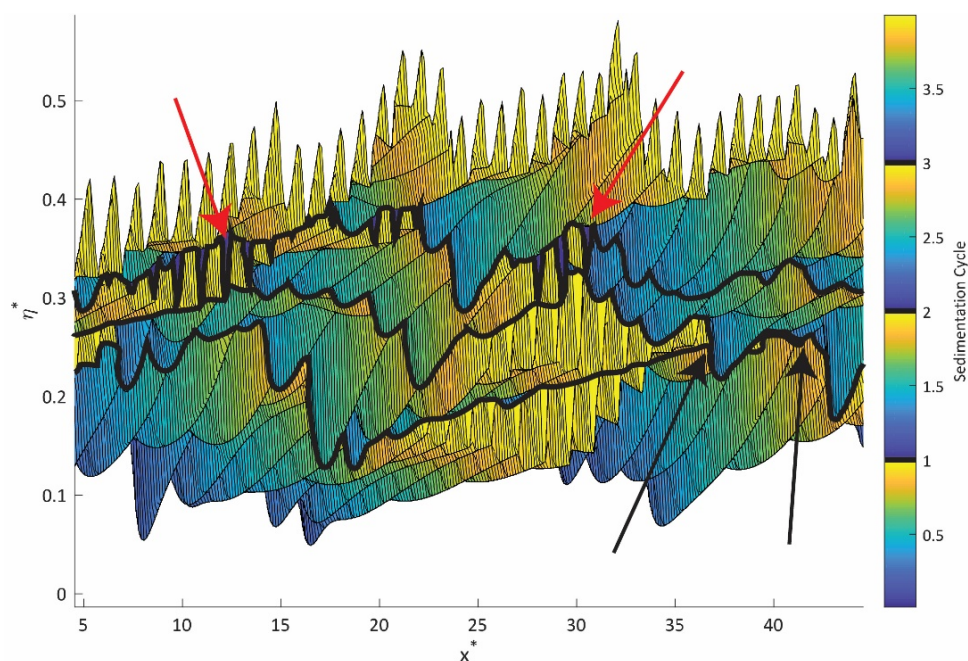


Figure 4.16 Synthetic stratigraphy of Page-type scour-and-fill aeolian accumulation from the model of this paper's companion (Swanson et al., accepted) (model parameters listed in Table A.1). Distance and height are expressed in dimensionless values scaled by equilibrium dune wavelength (x-axis) and equilibrium dune height (y-axis). Three water-table highstands are modeled by creating flat, erosional surfaces at progressively higher elevations between episodes of aeolian sedimentation. Following each water-table highstand, a new iteration of the dune field develops. The boldest black domain-scale lines identify three outcrop-scale bounding surfaces associated with the highstands. The next thickest black lines represent set bounding surfaces. Thin black lines represent the cross-strata. Colors within each outcrop-scale package represent the relative accumulation time of the deposit, with dark blue representing earliest-phase accumulation and light yellow representing latest-phase accumulation. Scours tend to preserve strata associated with the cutting dunes and cannibalize early-phase dune field accumulations, hence the absence of significant dark blue accumulations. Red arrows point to examples of a topographically-low dark blue regions representing the earliest-phase fill of antecedent topography. Conceptually, these locations function as an analog to the fill of antecedent J-2 topography by sets accumulated during early phases of the dune field (Figs. 4.8A-D). In the modeled scenarios, the scour of these accumulations is most frequently performed during later phases of the same sedimentation cycle. Black arrows point to the local amalgamation of two domain-scale bounding surfaces.

4.4 DISCUSSION

4.4.1 Interpretation of cross-strata

The thin sets of cross-strata of the basal Page are interpreted to represent dunes significantly smaller than those that gave rise to the sets of the lower and middle Page. The thin (mean = 0.16 m, n = 80) sets of the basal Page are characterized by thin grainflow strata (Fig. 4.7C; mean = 17.6 mm, n = 37) separated by grainfall deposits (Fig. 4.7B). Although the relationship between grainflow deposit thickness and dune height may be modified by factors other than dune height (McDonald and Anderson, 1995; Nickling et al., 2002; Nield et al., 2017; Cornwall et al., 2018), consistently thin grainflow strata are characteristic of small dunes. Moreover, the common presence of grainfall deposits between grainflow strata indicates smaller dunes where grainfall deposits of observable thickness extended to the base of the set (Hunter, 1977; Kocurek and Dott, 1981).

Several observations indicate that the lower and middle Page sets are the deposits of much larger dunes. Firstly, these sets are on average an order of magnitude thicker (Fig. 4.12A-D; lower Page mean = 1.61 m, n = 59, middle Page mean = 2.44 m, n = 401) than those of the basal Page (0.16 m, n = 80). While we acknowledge that relationships between dune height and set thickness is complicated by dune deformation and kinematics (e.g., Ganti et al., 2013), numerical modeling that accounts for both has shown a correlation between set thickness and dune height (Jerolmack and Mohrig, 2005). Secondly, the absence of grainfall deposits in the lower and middle Page sets (Fig. 4.6B, C) is suggestive of larger dunes where significant grainfall seldom reaches basal lee faces (Hunter, 1977; Kocurek and Dott, 1981). Thirdly, the sets of the lower and middle Page show alternating

grainflow and wind-ripple strata (Fig. 4.6B, C), as described in detail in Kocurek et al. (1991). This alternation of stratification types is commonly interpreted as seasonal cycles reflecting varying wind directions (Hunter and Rubin, 1983). Large dunes formed with an abundant sand supply are oriented to the gross bedform-normal transport direction over a year (e.g., Rubin and Hunter, 1987; Swanson et al., 2016), such that not all seasonal winds are transverse to the long-term crestline orientation. Repetitive packaging characteristic of multiple transporting wind directions is absent in sets of the basal Page, which is interpreted to represent dunes small enough to completely reorient their crests with each seasonal change in the wind regime (e.g., bedform response time is shorter than wind-direction cycles; Rubin and Hunter, 1987; Ewing et al., 2015). Of course, this comparison assumes that wind regimes were similar over the basal, lower, and middle Page dune fields, and that antecedent topography on the J-2 surface did not significantly steer winds.

Dune fields begin as collections of protodunes that interact during migration and grow into larger dunes (e.g., Werner, 1995; Ewing and Kocurek, 2010a; Swanson et al., 2017). Therefore, the relatively small dunes associated with the deposition of the basal Page sets are interpreted to represent an earlier phase of dune-field development when compared to the dune fields that produced the larger sets of the lower and middle Page. Significantly, there are no preserved strata from a comparably early phase of dune-field development in the lower and middle Page. This is consistent with modeling results from Swanson et al. (accepted) which predict the complete reworking of early-phase strata. An exception to this rule is early-phase strata sequestered in antecedent depressions (Fig. 4.16).

4.4.2 Stratigraphic architecture and outcrop-scale bounding-surface topography

4.4.2.1 Architecture preserved in antecedent J-2 topography

The J-2 regional surface represents regional erosion (Pipiringos and O'Sullivan, 1978), and the relief on this surface in the Page area is not interpreted to be a product of dune scouring linked to the troughs of migrating Page dunes. Rather, J-2 topography is interpreted as antecedent to the development of the Page depositional system. Depressions along this surface had a measurable effect upon the architecture of the Page Sandstone by providing local accommodation space for sabkha deposits, packages of wind-ripple strata (Kocurek et al., 1991; Havholm et al., 1993), and local, shallow-pond deposits (Swezey, 1991). Antecedent J-2 depressions of up to 10 m are also filled by stacks of thin cross-sets of the basal Page (Figs. 4.8A-D). These deposits are thought to have aggraded there owing to local wind deceleration moving into the depression. At a location where the lower Page sits directly above the J-2 surface, the lower Page is observed to thin towards an antecedent topographic high, where it is composed of three to five stacked sets (Figs. 4.5, A.1). Although these lower Page sets do not represent sedimentation by an early dune phase, we hypothesize that J-2 topography nonetheless controlled accumulation of the lower Page, as it did the basal Page. This hypothesis is quantitatively tested later in the discussion section.

The antecedent relief of the J-2 surface prevented full reworking of the early-phase dune strata by later, deep-scouring larger dunes (Figs. 4.8A-D), as predicted by the numerical model (Fig. 4.16). Even so, packages of thin sets were partially scoured during reactivations of the Page dune fields and later filled by thicker sets of cross-strata. At Ferry Swale, scouring into the basal Page (Figs. 4.8C, D) formed a large depression that was later

filled by strata from at least two sides (Fig. 4.13). Near the Golf Course outcrop, several meters of stacked, thin sets of the basal Page were laterally truncated by a thick set of lower Page (Fig. 4.8A, B). Although this section of basal Page was probably also formed in a J-2 depression, the J-2 surface is locally covered. Aggradation of early phases of Page dune fields may have occurred beyond any localized J-2 depressions, but ultimately, as dunes grew in size, these accumulations would have been completely cannibalized (Swanson et al., accepted).

4.4.2.2 Scour-and-fill architecture and coeval development of relief on outcrop-scale bounding surfaces

Several lines of evidence support a scour-and-fill-type architecture (Fig. 4.3C) for the middle Page, including set geometry, set dimensions, outcrop-scale bounding-surface topography, and the distribution of set thicknesses. The most common set geometry is the scour-and-fill type (Fig. 4.15). This is confirmed with the lack of a predictive relationship between local outcrop-scale package thickness and the number of stacked sets (Fig. 4.9B). A better correlation is expected in an aggradational scenario (Fig. 4.3A, B). In the perpendicular-to-transport exposure at Ferry Swale (Fig. 4.4), the similarity in width of both topographic scallops along outcrop-scale bounding surfaces (mean = 72 m, σ = 34 m) and the sets of cross-strata that fill these scallops (mean = 64 m, σ = 81 m) is significant. It suggests that the topographic scallops and the sets filling the scallops were associated with migration of the same dune, or at least associated with dunes of the same size and of the same late phase of dune-field development. This scour-and-fill architecture stands in sharp

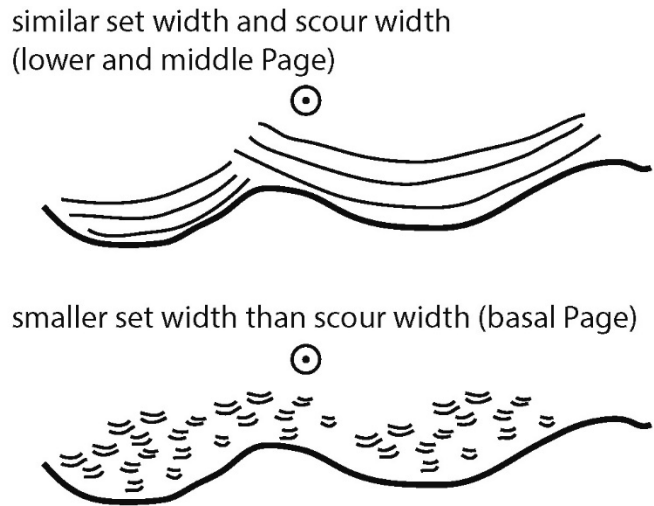


Figure 4.17 Schematic diagram showing the relationship between the scale of scour troughs (thicker lines) and the scale of filling sets (thinner lines). In the lower and middle Page, where scours are coeval with dune migration, set width and scour width are similar. In the basal Page, where scours are antecedent to the dune field, the scales are not similar. The circles with center dots show that both diagrams show perpendicular-to-transport views.

contrast to the thin aeolian dune sets (average thickness = 0.16 m) filling deep antecedent J-2 erosional relief (10 m; Fig. 4.17).

Although seen in outcrop as continuous surfaces with erosional relief, the outcrop-scale bounding surfaces can be defined as a lateral continuum of distinct scallops (Figs. 4.4, 4.5). As such, these surfaces are viewed as compound erosional surfaces interpreted to have formed with the passage of many dunes with varying scour depth. Moreover, consistent with the numerical model (Fig. 4.16), the ultimate relief on the surface would reflect the passage of the largest dunes with the deepest scours. Continued reworking of the substrate is observed in theoretical and experimental work with zero net bed aggradation (Paola and Borgman, 1991; Bridge, 1997; Bridge and Best, 1997), and is consistent with the local truncation of sections of basal Page (Figs. 4.8A-D, 4.13), the

discontinuous preservation of sabkha deposits along outcrop-scale bounding surfaces (Figs. 4.10A-D), and the lateral truncation of outcrop-scale packages by subsequent scour (Fig. 4.5). Havholm et al. (1993) show, at the regional scale, the scour of the entire upper middle Page (PMu) along the regional traverse (Fig. 4.1B), and deep scours have been described elsewhere for the Page (Blakey, 1988). For the latter examples, scour associated with the passage of trains of large dunes is not unreasonable, but other deflationary processes cannot be discounted.

The corollary to the interpretation of dune-scoured bounding surfaces is that antecedent topography and autogenically formed dune scour topography can be distinguished from one another. Relief autogenically formed from variability in scour depths typically cannibalizes early-phase accumulations (Swanson et al., accepted), and scour widths scale well with the widths of the filling sets (Fig. 4.17). The scour of the basal surface coeval with dune migration is consistent with the scour-and-fill architecture of the cross-sets themselves, as well as with earlier interpretations regarding the formation of erosional outcrop-scale bounding surface relief (Havholm and Kocurek, 1994).

4.4.3 Dune-Field Kinematics from Set-Thickness Distributions

Set thickness and set architecture are a function of climb angle and variability in scour depth (Fig. 4.9C; Paola and Borgman, 1991; Bridge and Best, 1997). The dominance of scour-and-fill set architecture and scoured outcrop-scale bounding surfaces throughout the middle Page Sandstone suggests very low climb angles such that the succession of deepest trough-scouring depths are the predominant control on set thickness (Fig. 4.9C;

Paola and Borgman, 1991; Bridge and Best, 1997). This interpretation can be tested using relationships first established in Paola and Borgman (1991) and further generalized by Bridge and Best (1997) and Leclair et al. (1997). Mean set thickness, s_m , is a function of climb angle (δ), dune spacing (l), mean dune height (h_m), and the standard deviation of dune heights (h_σ^2):

$$s_m = l \tan(\delta) + 0.8225 (h_\sigma^2/h_m) \quad (1)$$

In Equation 1, $l \tan(\delta)$ describes the part of mean set thickness due to climb (Allen, 1970b; Rubin and Hunter, 1982) and its associated net bed aggradation. The second term, $0.8225 (h_\sigma^2/h_m)$, describes the part of mean set thickness produced by variability in dune size and thus, variability in scour depth as predicted by Paola and Borgman (1991). In the case of zero aggradation ($\delta = 0$), s_m is only a function of variability in dune size:

$$s_m = 0.8225 (h_\sigma^2/h_m) \quad (2)$$

Both Paola and Borgman (1991) and Bridge and Best (1997) note that with a climb angle of zero and gamma-distributed bedform heights, the standard deviation of set thicknesses (s_σ) is:

$$s_\sigma = 0.725 (h_\sigma^2/h_m) \quad (3)$$

Equations 2 and 3 can both be rearranged to solve for h_{sd}^2/h_m , yielding

$$s_\sigma / s_m = c_{v\text{-SETS}} = 0.88 \quad (4)$$

where $c_{v\text{-SETS}}$ is the coefficient of variation for an exponential distribution of set thicknesses. Because we have connected the dominance of scour-and-fill style sedimentation with a lack of significant aggradation using other arguments, the hypothesis

is that Equation 4 should hold true for the lower and middle Page Sandstone assuming that Page trough elevations were gamma distributed. It should be noted that Equation 4 is particularly useful in analyses of paleo-systems because it only requires measurements of set thicknesses that can be directly acquired in the field.

Using 402 measurements of thickness for sets of cross-strata preserved in the middle Page yield an $s_m = 2.44$ m and $s_\sigma = 2.20$ m (Fig. 4.12). Their c_{v-SETS} is 0.90, which is very close to the predicted 0.88 value of Equation 4. Importantly, the measured value is slightly greater than the predicted value, and within the bounds of a system dominated by variable trough depths (0.88 ± 0.3 ; Bridge, 1997). Numerical experiments by Jerolmack and Mohrig (2005) revealed that a c_{v-SETS} of 0.90 was associated with a climb angle of less than one-thousandth of a degree, essentially zero. Jerolmack and Mohrig (2005) also found that the incorporation of significant climb acted to reduce the c_{v-SETS} value down to a point where it could be as small as $c_{v-DUNES}$, the coefficient of variation of formative dune heights (h_σ/h_m). In contrast to the middle Page, the stacked sets of the basal Page have an $s_m = 0.16$ m and $s_\sigma = 0.10$ m, yielding a c_{v-SETS} of 0.64. This value is consistent numerical experiments that had a climb angle of 0.5 to 1° (Jerolmack and Mohrig, 2005). The lower Page, which also sits directly above the J-2 in some locations (Fig. 4.5) has a $s_m = 1.61$ m and $s_\sigma = 0.79$, with a $c_{v-SETS} = 0.49$. This c_v has been found to be associated with climb angles that have ranged between 1 to 6° (Jerolmack and Mohrig, 2005).

The theory of Paola and Borgman (1991), which has been subsequently built on by Bridge and Best (1997) and many others, takes as fact that the distribution of scouring topography can be accurately characterized using a two-parameter gamma distribution.

While this distribution has been shown to hold for a variety of fields of bedform topography (e.g., Paola and Borgman, 1991; van der Mark et al., 2008; Ganti et al., 2013), it is important to evaluate the likelihood of it being an accurate descriptor for the ancient Page system. Fortunately, the preserved strata directly provide data necessary to test the applicability of the stratification theory. Jerolmack and Mohrig (2005) demonstrated that as climb increases, the distribution of set thicknesses moved away from an exponential distribution characterizing set production by scouring only to unimodal, positively skewed gamma distributions with shapes inherited from the height distributions of the formative dunes. We can therefore use the structure of the set distributions themselves both to test the applicability of the modified theory and to test of the question of scour-and-fill versus aggradation. We have used the χ^2 goodness-of-fit tests at a .05 significance level to test the best-fit exponential and two-parameter gamma distribution for the distribution of sets from the basal, lower, and middle Page. The data can be visually compared to fitted curves as cumulative distribution functions (CDFs) and probability distribution functions (PDFs) in Figures 4.18A and B. The basal Page is rejected as exponential ($p = 0.02$), but the gamma fit is not rejected ($p = 0.21$). Similarly, the lower Page is rejected as exponential ($p < 0.001$), but the gamma fit is not rejected ($p = 0.34$). Both of these results are consistent with sets being generated under the presence of net bed aggradation, which we have shown can be attributed to the filling of antecedent J-2 topography with basal (Fig. 4.8A-D) and lower Page strata (Figs. 4.5 and A.1). In contrast, the best-fit exponential function is not rejected for the middle Page sets ($p = 0.49$), and, in fact, the exponential and gamma distributions are visually very similar, because at higher values for c_{V-SETS} the two-parameter gamma

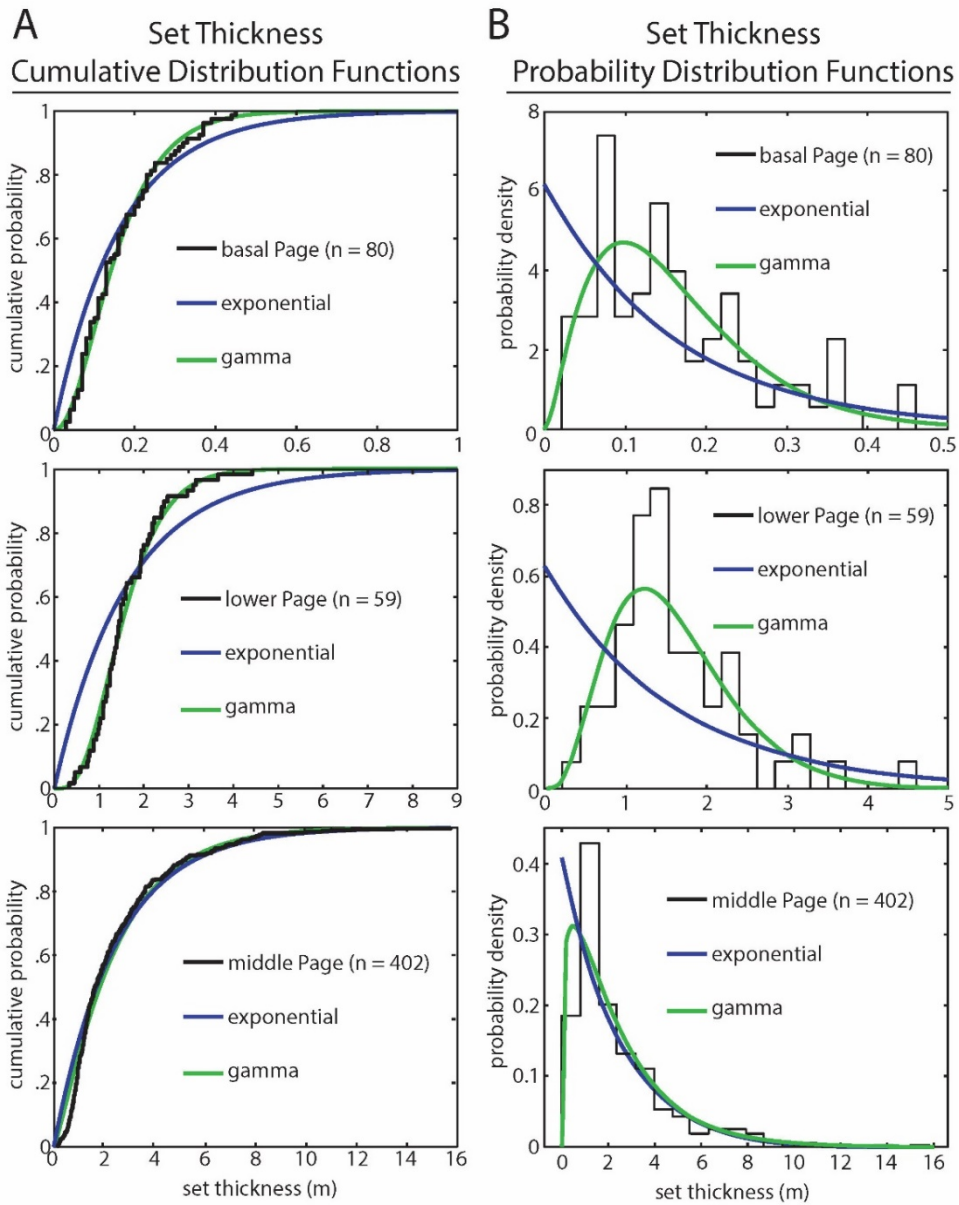


Figure 4.18 Comparisons of the basal Page, lower Page, and middle Page set thickness cumulative distribution functions (A) and probability density functions (B) to best-fit exponential and gamma curves. The disagreement of basal and lower Page exponential fits is indicative of significant dune climbing and aggradation. The agreement of the middle Page with an exponential fit, and the similarity of the fitted exponential and gamma curves, is consistent with a no-aggradation scenario. The underrepresentation of thinner sets in the middle Page is likely a measurement bias.

distribution yields an exponential shape. This exponential fit is taken as confirmation for the absence of climb in the middle Page, and the production of stratigraphy through successive scouring of the bed by migrating dunes.

To further demonstrate the universality of set thickness statistics in analyses of aeolian strata, the method was applied to set-thickness measurements from the nearby Jurassic Entrada Sandstone, a type example of an aggradational dune field with measurable positive climb angles (Crabaugh and Kocurek, 1993; Kocurek and Day, 2018). Thicknesses of 37 Entrada sets were taken from two vertical sections from Figure 2 of Kocurek and Day (2017), one characterized by downlapping sets filling a depression, and the other by climbing sets. For the Entrada, $s_m = 2.10$ m, $s_\sigma = 0.96$ m, and $c_{v-SETS} = 0.46$. This ratio value suggests sufficient aggradation such that c_{v-SETS} more closely reflects $c_{v-DUNES}$ (Jerolmack and Mohrig, 2005) rather than Equation 4. This is again supported by the statistical rejection of an exponential fit ($p < 0.001$) and the non-rejection of a gamma fit ($p = 0.16$). Indeed, Kocurek and Day (2017) interpret the Entrada strata as including a component of allogenic forced bed aggradation.

4.4.4 Reconstruction of the middle Page dune fields

Reasonable approximations of a gamma distribution of bedform heights of the middle Page can be calculated using set-thickness measurements and a few simple assumptions about the formative dune field. The two parameters defining a gamma distribution, α and β , are functions of the mean (h_m) and standard deviation (h_σ) of the population, in this case dune heights:

$$\alpha = h_m^2/h_\sigma^2 \quad (5)$$

$$\beta = h_\sigma^2/h_m \quad (6)$$

The numerical experiments of Jerolmack and Mohrig (2005) show that, in the zero bed aggradation case,

$$h_m = s_m/0.4 \quad (7)$$

Although h_σ is not directly measurable with the available data, it can be estimated using assumptions about the coefficient of variation of middle Page dune heights ($c_{v-DUNES}$):

$$h_\sigma = c_{v-DUNES} * h_m \quad (8)$$

We generate three distributions of middle Page dune heights using low, medium, and high estimates of the middle Page $c_{v-DUNES}$ informed by modern dune fields. White Sands dune field has a $c_{v-DUNES}$ of 0.28 (Baitis et al., 2014). Using Shuttle Radar Topography Mission elevation data (image number N32W116), we calculate a $c_{v-DUNES}$ at Algodones dune field, California, of 0.45 ($n = 52$), and use this as a middle value. A high-end estimate is constructed with $c_{v-DUNES} = 0.60$, a value observed in fluvial dune fields (e.g., Trinity River, Texas: $c_{v-DUNES} = 0.68$: Mason and Mohrig in review).

The three gamma curves are compared to the exponential set-thickness curve in Figure 4.19. Note that the low- $c_{v-DUNES}$ scenario rapidly approaches a probability density of 0 at 12 m, while the other distributions have longer tails. The low $c_{v-DUNES}$ scenario is unlikely to create dunes higher than the thickest observed sets. The near-surface water table at White Sands (Kocurek et al., 2007) is likely preventing significant dune scour, thus limiting dune heights and $c_{v-DUNES}$. We hypothesize that a low $c_{v-DUNES}$ is a common dune-field response to a near-surface water table. Assuming this hypothesis to be correct, the

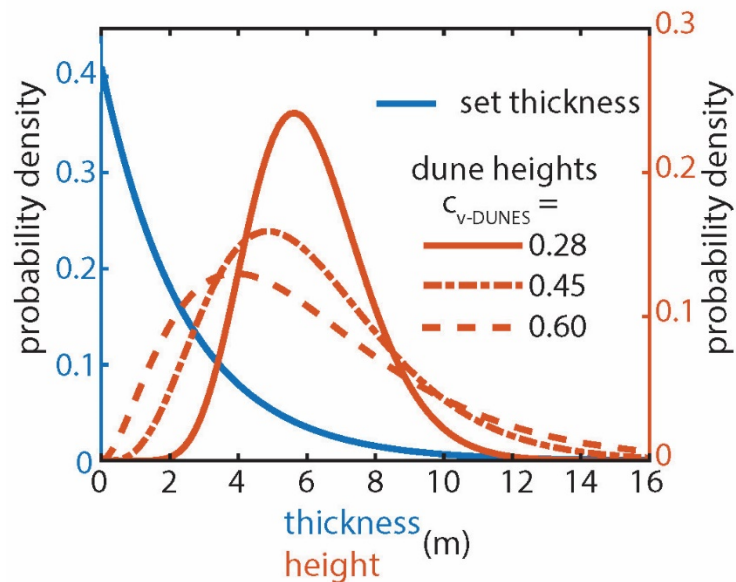


Figure 4.19 Probability density functions (PDFs) comparing the statistically-significant exponential fit to middle Page set thicknesses, and three gamma curves show the distribution of middle Page dune heights assuming $c_{v-DUNES}$ equal to 0.28, 0.45, and 0.60. The $c_{v-DUNES} = 0.28$ scenario approaches zero with the set thickness function, indicating that this hypothesized distribution of dune heights is unlikely to have formed dunes tall enough to create the thickest Page sets.

inconsistencies between the low- $c_{v-DUNES}$ model and the observed set thicknesses are additional evidence of a lack of a near-surface water table in the middle Page dune fields.

4.4.5 Role of Autogenic vs. Allogenic Controls on the Page Preserved Record

Autogenic processes of dune scour-and-fill alone will not result in the preservation of stacked multiple dune constructional periods that represent the Page Sandstone. Indeed, without any additional forcing, the Page dune fields would be represented by an erosional surface and strata preserved just within depressions along the J-2 surface, as the analysis above shows that there was no significant climb during these periods. In agreement with

previous work (Havholm and Kocurek, 1994; Blakey et al., 1996) and model results (Fig. 4.16), preservation of Page accumulations is best attributed to allogenic forcing, which consisted of an episodic, but net progressive, rise of the continental water table as a function of sea level in the adjacent Carmel. The preserved accumulations capture those parts of the scour fill that were incorporated within the rising water table. Where scours were deeper, thicker sections were preserved (Fig. 4.9A). Field evidence argues that high stands of the Carmel sea were characterized inland not only by a limit to deflation of the aeolian accumulations, but also a diminished sand supply such that dune fields were replaced by extensive polygonally fractured surfaces and sabkha deposition (Figs. 4.10A-C, 4.11A-C). Later aeolian constructional periods during falling sea level and low stands were characterized by an influx of additional sand but also by scour into the surface, producing the compound erosional outcrop-scale surfaces.

Broadly speaking, the preservation of any non-scour-and-fill-type architecture, as well as the stacking on multiple discrete scour-and-fill packages, represents an allogenic forcing overcoming the autogenic, signal-shredding tendencies of the ancient Page dune fields. This is consistent with much of the current theory regarding the recording of environmental signals in stratigraphy (Castelltort and Van Den Drieschhe 2003; Jerolmack and Paola 2010; Ganti et al. 2014; Romans et al. 2016; Paola et al. 2018), and framing future observations of aeolian stratigraphy in this manner will be informative of ancient environmental conditions on Earth and other planetary bodies with aeolian stratigraphic records, particularly Mars (e.g., Grotzinger et al. 2005; Milliken et al. 2014; Brothers et al.

2018; Banham et al. 2018; Day and Catling 2018; Anderson et al. 2018; Day and Catling 2019).

4.5 CONCLUSIONS

The Page Sandstone preserves a record of allogenic boundary conditions episodically or locally overcoming an autogenic tendency of the Page dune fields to shred their earlier accumulations. These processes are unraveled from Page strata largely through the analysis of cross-set thickness distributions coupled with geologic context, and interpretations are tested against results from the numerical model presented completely in the companion paper (Swanson et al., accepted). The methods used here to quantify the set architecture of the Page Sandstone are universal, and can be applied to any other aeolian sandstone where there is interest in understanding the formative environmental conditions of the associated ancient dune field. In addition to outcrops of sandstone on Earth, aeolian sandstones on Mars could be characterized by similar methods using rover and remote-sensing data. Interpretations of the unique influences on the development of other types of strata, such as fluvial or carbonate grainstone cross sets, will benefit from this type of analysis as well.

4.6 ACKNOWLEDGEMENTS

We would like to thank Associate Editor John Gillies, Co-Editor Peter Burgess, John Southard, Ryan Ewing, and an anonymous reviewer for their detailed feedback, which has greatly improved this manuscript. Melissa Lester's work in facilitating these reviews is appreciated. We also thank Dan T.S.M. Aylward for his assistance in the field. John

Spence at the Glen Canyon Dam National Park Service and Jake Hunter at Lake Powell National Golf Course were very helpful in facilitating outcrop access. We also thank Joe Levy for the use of his field equipment, and the David Mohrig Research Group and Shell Clastics Research Group for discussions and feedback throughout the evolution of this project. This work was supported by Shell International Exploration and Production Inc., the RioMAR Industry Consortium, and the University of Texas Jackson School of Geosciences. This chapter is based on a manuscript that has been accepted to the Journal of Sedimentary Research as of June 19, 2019.

Chapter 5: Conclusions

The work in this dissertation seeks to understand the accumulation and preservation of the fluvial and aeolian rock records. Although the three contributions vary by depositional system and study scale, the driving questions are consistent throughout. What elements of the depositional system have accumulated here? How well are these elements preserved? How much time is represented, and how much is missing? In all three chapters, answering these questions comes down to the reconstruction of paleo-topography.

In Chapter 2, fluvial channel belts of the Cedar Mountain Formation showed that bar topography controlled the accumulation of dune strata, which in turn drove bar migration. At an average of 41% total channel-belt thickness, these bar and dune strata composed a significant portion of these channel belts. Topography is also the source of the transport anomaly, a measurement which allowed us to test the preservation of river-channel planform geometry. The preservation of bar topography was the product of rapid avulsions, and the successive re-occupations indicated the abandoned channels were underfilled, and still a significant source of relief on the floodplain. Chapter 3 examined the significance of larger-scale relief built between alluvial ridges that developed erosional drainage networks. Channel belts contained within this relief could be mapped continuously for kilometers due to this relief. The aeolian Page Sandstone discussed in Chapter 4 responds to antecedent topography. Early-phase dune-field strata filled local relief in the basal unconformity, but were scoured away in all other locations. Later-phase strata in direct contact with the basal unconformity accumulated more rapidly than all of the following dune field strata, which had set-thickness distributions and architectures characteristic of bypass dune fields. Without an external or internal source of larger-scale topography, these bypass dune field strata only represented the fill of their own deepest scours. Clearly, the reconstruction of paleo-topography is a major component of

understanding the accumulation and preservation of clastic strata, independent of the studied depositional settings and spatial scales.

In Chapters 2 and 4, system-scale interpretations are built up from the most localized, fundamental measurement one might make of a sedimentary rock: cross-set thickness. The statistical moments and distributions of cross-set thicknesses can be used to quantifiably reconstruct sediment accumulation and bedform motion, with the added benefit of statistical hypothesis testing, yet anything more than a mean is rarely reported, and these means tend to be used more descriptively. Detailed reports of these measurements would serve the community well as quantification becomes more important in field geology. In search of a similar fundamental measurement for fluvial deposits imaged in 3-D seismic reflection volumes, Chapter 3 describes the analysis of channel-belt lengths normalized by average width. The analysis leads to a successful reconstruction of the evolution of the depositional system through time, and will hopefully prove useful as more of these seismic reflection volumes enter public domain.

Future work might include the application of the cross-set analysis to different depositional systems, such as deep water or carbonates. Ultimately, the motion of bedforms and accumulation of sediment is controlled by larger-scale processes, either internal or external, which are likely to be unique in different settings. Any analysis applied to those systems will be informative of those unique controls. As high-resolution remote-sensing and rover data continue to return from Mars, we have the opportunity to quantitatively reconstruct the controls on sedimentary systems on another planet, under a completely unique set of boundary conditions. The continued use of seismic volumes as process sedimentology datasets at the regional scale will also require continued development and experimentation. *Landscapes on the Edge*, a 2010 report published by the National

Research Council, recognizes that these volumes “have hardly been tapped” (p. 39) as sources for understanding the evolution of Earth’s surface, and I think their value is clear.

Finally, the work here relates the sedimentary rock record to geomorphic evolution under some set of boundary conditions. In the ancient, we see the record and must infer the boundary conditions. In the modern, we know boundary conditions at Earth’s surface are changing, and must work the problem in reverse. Work like this will, I like to think, be helpful in predicting the resultant geomorphic change in places where people live. This dissertation was, after all, typed at Earth’s surface.

Appendix

Figure A.1 See supplemental file. Complete cross-section of the Ferry Swale outcrop, including a change in outcrop orientation (location shown in Fig. 4.2). The following page shows this figure at full resolution. There is no vertical exaggeration. Outcrop-scale bounding surfaces are represented by bold black lines separating outcrop-scale packages of cross-strata of different colors. The major surfaces among those are labeled S-up, S-rm, S-jh, and S-b (Havholm et al., 1993). Thinner black lines within outcrop-scale packages represent cross-set boundaries. Dipping gray lines represent the apparent dip direction of the mean Page paleotransport direction. The colors used to separate outcrop-scale packages do not represent correlations between outcrop-scale packages shown in Figures A.2 or A.3. Informal Page units are composed of one to several outcrop-scale packages separated by the outcrop-scale surfaces, and are labeled as in Havholm et al. (1993): PB (Basal Page), PL (lower Page), PMm (middle middle Page), and PUI (lower upper Page). The PUI, colored peach, is composed of compound dune deposits, and not studied here. Part of the basal Page exposed to the west of the panel and not analyzed here is composed of alternating sabkha and cross-sets. This package of PB is locally preserved above the J-2, and pinches out towards the east. A section of PB exposed towards the east contains the thin, stacked sets shown in Figures 4.8C-D and 4.13. It is not uncommon for an outcrop-scale package to be composed of one to a few sets; the pink outcrop-scale package is used as an example. Outcrop-scale bounding surfaces have meters of relief at this location. The width of a scallop in outcrop-scale bounding surface relief is demonstrated with white text and a white double-headed arrow. The outcrop-scale relief of the J-2 surface is shown. The J-2 is at its highest elevation at the westernmost part of the panel, and at its lowest exposed elevation beneath the thin, stacked sets. The locations of Figures 4.4 and 4.5 from the main text are shown.

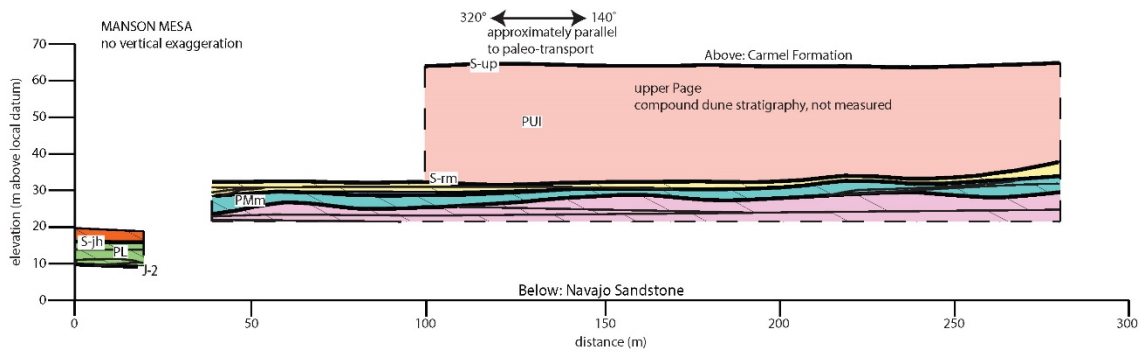


Figure A.2 Projected cross-section of the parallel-to-transport Manson Mesa outcrop (location shown in Fig. 4.2). Symbology is the same as in Figure A.1. Sets are more laterally continuous at this location, and there is less relief along outcrop-scale surfaces than at Ferry Swale. Exposures of lower Page and S-jh at the left of the panel become vertical towards the right, and eventually are buried, and as such are not continuously surveyed.

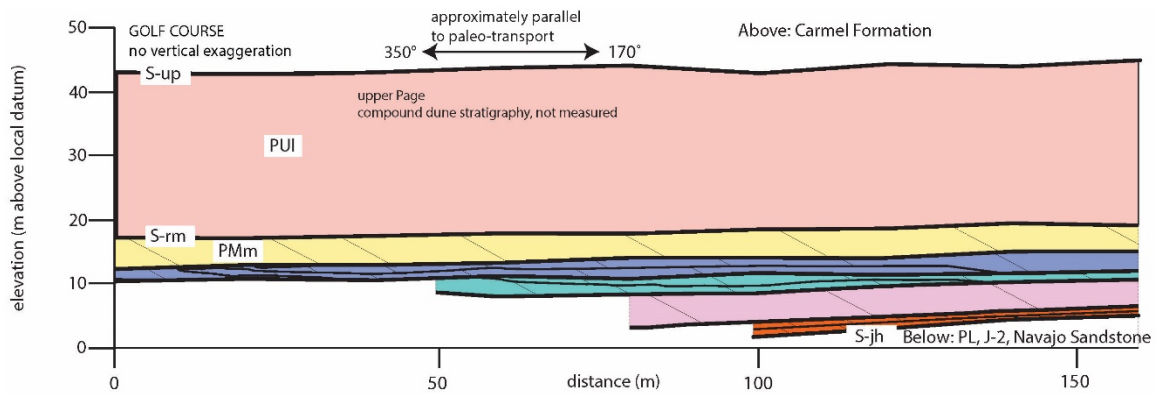


Figure A.3 Projected vertical section of the parallel-to-transport Golf Course outcrop (location shown in Fig. 4.2). Symbology is the same as in Figure A.1. Like the Manson Mesa outcrop, sets are more continuous and there is less relief along outcrop-scale surfaces compared to Ferry Swale. The vertical wall exposing a package of thin sets is 150 meters north of this location (Fig. 4.8A-B).

Table A.1 Parameters used in the numerical model (Fig. 4.16). Parameters are discussed in detail in a companion paper (Swanson et al., accepted). Units are arbitrary.

Parameter	Value	Description
A	0.1	Flow blocking parameter
B	3	Flow shoaling parameter
m	1	Meyer-Peter and Müller coefficient
n	1.5	Meyer-Peter and Müller coefficient
E	20	Avalanching coefficient
D	0.2	Diffusivity
p	0.4	Bed porosity
τ_a	0.3	Ambient shear stress
r_a	$1E - 4$	Bed aggradation
Δt	1	Model timestep
Δx	10	Node spacing
Δwt	.5	Vertical distance ascended by water table following each deposode

References

- Allen, J.R.L., 1970a, The avalanching of granular solids on dune and similar slopes: *The Journal of Geology*, 78, 326-351.
- Allen, J.R.L., 1970b, A quantitative model of climbing ripples and their cross-laminated deposits: *Sedimentology*, 14, 5–26.
- Allen, J.R.L., 1983, Studies in fluvial sedimentation: bars, bar-complexes and sandstone sheets (low-sinuosity braided streams) in the Brownstones (L. Devonian), Welsh Borders: *Sedimentary Geology*, 33, 237–293.
- Almeida, R.P., Freitas, B.T., Turra, B.B., Figueiredo, F.T., Marconato, A., and Janikian, L., 2016, Reconstructing fluvial bar surfaces from compound cross-strata and the interpretation of bar accretion direction in large river deposits: *Sedimentology*, 63, 609–628.
- Anderson, R.B., Edgar, L.A., Rubin, D.M., Lewis, K.W., and Newman, C., 2018, Complex bedding geometry in the upper portion of Aeolis Mons, Gale Crater, Mars: *Icarus*, 314, 246-264.
- Armstrong, C., 2012, 3D seismic geomorphology and stratigraphy of the Late Miocene to Pliocene Mississippi River delta: fluvial systems and dynamics: Master's Thesis, University of Texas at Austin, Austin, TX, 119 p.
- Armstrong, C., Mohrig, D., Hess, T., George, T., and Straug, K.M., 2014, Influence of growth faults on coastal fluvial systems: examples from the late Miocene to recent Mississippi River Delta: *Sedimentary Geology*, 301, 120-132.

- Bahorich, M., and Farmer, S., 1995, 3-D seismic discontinuity for faults and stratigraphic features: The coherence cube: *The Leading Edge*, v. 14, p. 1021-1098.
- Baitis, E., Kocurek, G., Smith, V., Mohrig, D., Ewing, R.C., and Peyret, A.-P. B., 2014, Definition and origin of the dune-field pattern at White Sands, New Mexico: *Aeolian Research*, 15, 269–287.
- Banham, S.G., Gupta, S., Rubin, D.M., Watkins, J.A., Sumner, D.Y., Edgett, K.S., Grotzinger, J.P., Lewis, K.W., Edgar, L.A., Stack-Morgan, K.M., Barnes, R., Bell III, J.F., Day, M.D., Ewing, R.C., Lapotre, M.G.A., Stein, N.T., Rivera-Hernandez, F., and Vasavada, A.R., 2018, Ancient Martian aeolian processes and palaeomorphology reconstructed from the Stimson formation on the lower slope of Aeolis Mons, Gale crater, Mars: *Sedimentology*, 65, 993-1042.
- Berens, P., 2009, CircStat: A MATLAB Toolbox for Circular Statistics: *Journal of Statistical Software*, 31, 1-21.
- Blakey, R.C., 1988, Superscoops: their significance as elements of eolian architecture: *Geology*, 16, 483-487.
- Blakey, R.C., and Parnell, R.A., 1995, Middle Jurassic magmatism: The volcanic record in the eolian Page Sandstone and related Carmel Formation, Colorado Plateau. *In* Miller, D.M., and Busby, C., eds., *Jurassic Magmatism and Tectonics of the North American Cordillera*: Geological Society of America, Special Papers 299, 393–412.
- Blakey, R.C., Havholm, K.G., and Jones, L.S., 1996, Stratigraphic analysis of eolian interactions with marine and fluvial deposits, Middle Jurassic Page Sandstone and

- Carmel Formation, Colorado Plateau, USA: *Journal of Sedimentary Research*, 66, 324-342.
- Blakey, R.C., Peterson, F., and Kocurek, G., 1988, Synthesis of late Paleozoic and Mesozoic eolian deposits of the Western Interior of the United States: *Sedimentary Geology*, 56, 3–125.
- Blakey, R.C., Peterson, F., Caputo, M.V., Geesaman, R.C., and Voorhees, B.J., 1983, Paleogeography of Middle Jurassic continental, shoreline, and shallow marine sedimentation, southern Utah, *in* Dunne, G.C., and McDougall, K.A., eds., *Mesozoic Paleogeography of the Western United States – II*: SEPM, Rocky Mountain Section 71, 77–100.
- Blum, M.D., and Törnqvist, T.E., 2005, Fluvial responses to climate and sea-level change: a review and look forward: *Sedimentology*, v. 47, p. 2-48.
- Bridge, J., 1997, Thickness of sets of cross strata and planar strata as a function of formative bed-wave geometry and migration, and aggradation rate: *Geology*, 25, 971-974.
- Bridge, J., and Best, J., 1997, Preservation of planar laminae due to migration of low-relief bed waves over aggrading upper-stage plane beds: comparison of experimental data with theory: *Sedimentology*, 44, 253–262.
- Brothers, S.C., Kocurek, G., and Holt, J.W., 2018, Sequence architecture of the cavi unit, Chasma Boreale, Mars: *Icarus*, 308, 42-60.
- Brothers, S.C., Kocurek, G., Brothers, T.C., and Buynevich, I.V., 2017, Stratigraphic architecture resulting from dune interactions: White Sands Dune Field, New Mexico: *Sedimentology*, 64, 686-713.

- Burr, D.M., Enga, M.-T., Williams, R.M., Zimelman, J.R., Howard, A.D., and Brennand, T.A., 2009, Pervasive aqueous paleoflow features in the Aeoliz/Zephyria Plana region, Mars: *Icarus*, 200, 52-76.
- Cardenas, B.T., Kocurek, G., Mohrig, D., Swanson, T., Hughes, C.M., and Brothers, S.C., accepted, Preservation of autogenic processes and allogenic forcings within set-scale aeolian architecture II: the scour-and-fill dominated Jurassic Page Sandstone, Arizona, USA: *Journal of Sedimentary Research*.
- Cardenas, B.T., Mohrig, D., and Goudge, T.A., 2018, Fluvial stratigraphy of valley fills at Aeolis Dorsa, Mars: Evidence for base-level fluctuations controlled by a downstream water body: *Geological Society of America Bulletin*, 130, 484-498.
- Cardenas, B.T., Mohrig, D., Hughes, C.M., Goudge, T.A., Levy, J.S., Swanson, T., Mason, J., and Zhao, F., in review, The anatomy of exhumed river-channel belts. *Sedimentology*.
- Cardenas, B.T., Swartz, J.M., Mohrig, D., Prokocki, E.W. Setting up the preservation of fluvial channel belts. *Geology*, in review.
- Carling, P.A., and Leclair, S.F., 2019, Alluvial stratification styles in a large, flash-flood influenced dryland river: The Luni River, Thar Desert, north-west India: *Sedimentology*, 66, 102-128.
- Castelltort, S., and Van Den Driessche, J., 2003, How plausible are high-frequency sediment supply-driven cycles in the stratigraphic record?: *Sedimentary Geology*, 157, 3-13.

- Chakraborty, T., Kar, R., Ghosh, P., and Basu, S. (2010) Kosi megafan: Historical records, geomorphology and the recent avulsion of the Kosi River. *Quaternary International*, 227, 143-160.
- Chamberlin, E.P., and Hajek, E.A., 2015, Interpreting paleo-avulsion dynamics from multistory sand bodies: *Journal of Sedimentary Research*, 85, 82–94.
- Chamberlin, E.P., and Hajek, E.A., 2019, Using bar preservation to constrain reworking in channel-dominated fluvial stratigraphy: *Geology*, 47, 531-534.
- Coleman, S.E., and Melville, B.W., 1996, Initiation of bed forms on a flat sand bed: *Journal of Hydraulic Engineering*, 122, 301-310.
- Cornwall, C., Jackson, D.W.T., Bourke, M.C., and Cooper, J.A. G., 2018, Morphometric analysis of slipface processes of an aeolian dune: Implications for grain-flow dynamics: *Sedimentology*, 65, 2034-2054.
- Courrech du Pont, S., Narteau, C., and Gao, X., 2014, Two modes for dune orientation: *Geology*, 42, 743-746.
- Crabaugh, M., and Kocurek, G., 1993, Entrada Sandstone: an example of a wet aeolian system, *in* Pye, K., ed., *The Dynamics and Environmental Context of Aeolian Sedimentary Systems*: Geological Society of London, Special Publications 72, 103–126
- Cuevas Martínez, J.L., Cabrera Pérez, L., Marcuello, A., Arbués Cazo, P., Marzo Carpio, M., and Bellmunt, F., 2010, Exhumed channel sandstone networks within fluvial fan deposits from the Oligo-Miocene Caspe Formation, South-east Ebro Basin (North-east Spain): *Sedimentology*, 57, 162–189.

- Currie, B.S., 1998, Upper Jurassic-Lower Cretaceous Morrison and Cedar Mountain Formations, Ne Utah-Nw Colordao: Relationships between Nonmarine Deposition and Early Cordilleran Foreland-Basin Development: *Journal of Sedimentary Research*, 68, 632-652.
- Davis, J.M., Balme, M., Grindrod, P.M., Williams, R.M.E., and Gupta, S., 2016, Extensive Noachian fluvial systems in Arabia Terra: implications for early Martian climate: *Geology*, 44, 847-850.
- Day, M.D., and Catling, D.C., 2018, Dune casts preserved by partial burial: The first identification of ghost dune pits on Mars: *Journal of Geophysical Research: Planets*, 123, 1431-1448.
- Day, M.D., and Catling, D.C., 2019, Potential aeolian deposition of intra-crater layering: A case study of Henry crater, Mars: *Geological Society of America Bulletin*, in press.
- Day, M.D., and Kocurek, G., 2017, Aeolian dune interactions preserved in the ancient rock record: *Sedimentary Geology*, 358, 187-196.
- Day, M.D., and Kocurek, G., 2018, Pattern similarity across planetary dune fields: *Geology*, 46, 999-1002.
- DeCelles, P.G., Langford, R.P., and Schwartz, R.K., 1983, Two New Methods of Paleocurrent Determination from Trough Cross-Stratification: *Journal of Sedimentary Research*, 53, 629-642.
- DiBiase, R.A., Limaye, A.B., Scheingross, J.S., Fischer, W.W., and Lamb, M.P., 2013, Deltaic deposits at Aeolis Dorsa: Sedimentary evidence for a standing body of

- water on the northern plain of Mars: *Journal of Geophysical Research: Planets*, 118, 1285-1302.
- Dickinson, W.R., Stair, K.N., Gehrels, G.E., Peters, L., Kowallis, B.J., Blakey, R.C., Amar, J.R., and Greenhalgh, B.W., 2010, U-Pb and $^{40}\text{Ar}/^{39}\text{Ar}$ Ages for a tephra lens in the Middle Jurassic Page Sandstone: First direct isotopic dating of a Mesozoic eolianite on the Colorado Plateau: *The Journal of Geology*, 118, 215–221.
- Dietrich, W.E., and Smith, J.D., 1984, Bed load transport in a river meander: *Water Resources Research*, 20, 1355-1380.
- Dott, R.H., Jr., 1973, Paleocurrent Analysis of Trough Cross Stratification: *Journal of Sedimentary Research*, 43, 779-783.
- Durkin, P.R., Hubbard, S.M., Holbrook, J., and Boyd, R., 2018, Evolution of fluvial meander-belt deposits and implications for the completeness of the stratigraphic record: *Geological Society of America Bulletin*, 130, 721-739.
- Eastwood, E.N., Kocurek, G., Mohrig, D., and Swanson, T., 2012, Methodology for reconstructing wind direction, wind speed and duration of wind events from aeolian cross-strata: *Journal of Geophysical Research: Earth Surface*, 117, F03035.
- Edmonds, D.A., Hajek, E.A., Downton, N., and Bryk, A.B., 2016, Avulsion flow-path selection on rivers in foreland basins: *Geology*, 44, 695–698.
- Edwards, M.B., Eriksson, K.A., and Kier, R.S., 1983, Paleochannel geometry and flow patterns determined from exhumed Permian point bars in north-central Texas: *Journal of Sedimentary Research*, 53, 1261-1270.

- Ewing, R.C., and Kocurek, G., 2010a, Aeolian dune-field pattern boundary conditions: *Geomorphology*, 114, 175–187.
- Ewing, R.C., and Kocurek, G., 2010b, Aeolian dune interactions and dune-field pattern formation: White Sands Dune Field, New Mexico: *Sedimentology*, 57, 1199-1219.
- Ewing, R.C., McDonald, G.D., and Hayes, A.G., 2015, Multi-spatial analysis of aeolian dune-field patterns: *Geomorphology*, 240, 44–53.
- Friend, P.F., Slater, M.J., and Williams, R.C., 1979, Vertical and lateral building of river sandstone bodies, Ebro Basin, Spain: *Journal of the Geological Society*, 136, 39–46.
- Fryberger, S.G., Schenk, C.J., and Krystinik, L.F., 1988, Stokes surfaces and the effects of near-surface groundwater-table on aeolian deposition: *Sedimentology*, 35, 21-41.
- Ganti, V., Lamb, M.P., and McElroy, B., 2014, Quantitative bounds on morphodynamics and implications for reading the sedimentary record: *Nature Communications*, 5, 3298.
- Ganti, V., Paola, C., and Fofoula-Georgiou, E., 2013, Kinematic controls on the geometry of the preserved cross sets: *Journal of Geophysical Research: Earth Surface*, 118, 1296-1307.
- Gao, X., Narteau, C., and Rozier, O., 2015a, Development and steady states of transverse dunes: A numerical analysis of dune pattern coarsening and giant dunes: *Journal of Geophysical Research: Earth Surface*, v. 120, no. 2015JF003549.
- Gao, X., Narteau, C., Rozier, O., and Courrech du Pont, S., 2015b, Phase diagrams of dune shape and orientation depending on sand availability: *Scientific Reports*, 5, 14677.

- Garrison, J.R., Brinkman, D., Nichols, D.J., Layer, P., Burge, D., and Thayn, D., 2007, A multidisciplinary study of the Lower Cretaceous Cedar Mountain Formation, Mussentuchit Wash, Utah: a determination of the paleoenvironment and paleoecology of the *Eolambia caroljonesa* dinosaur quarry: *Cretaceous Research*, 28, 461–494.
- Gibling, M.R., 2006, Width and thickness of fluvial channel bodies and valley fills in the geological record: a literature compilation and classification: *Journal of Sedimentary Research*, 76, 731–770.
- Goudge, T.A., Mohrig, D., Cardenas, B.T., Hughes, C.M., and Fassett, C.I., 2018, Stratigraphy and paleohydrology of delta channel deposits, Jezero crater, Mars: *Icarus*, 301, 58–75.
- Grotzinger, J.P., Arvidson, R.E., Bell III, J.F., Calvin, W., Clark, B.C., Fike, D.A., Golombek, M., Greeley, R., Haldemann, A., Herkenhoff, K.E., Jolliff, B.L., Knoll, A.H., Malin, M., McLennan, S.M., Parker, T., Soderblom, L., Sohl-Dickstein, J.N., Squyres, S.W., Tosca, N.J., and Watters, W.A., 2005, Stratigraphy and sedimentology of a dry to wet eolian depositional system, Burns formation, Meridiani Planum, Mars: *Earth and Planetary Science Letters*, 240, 11-72.
- Hajek, E.A., and Heller, P.L., 2012, Flow-depth scaling in alluvial architecture and nonmarine sequence stratigraphy: example from the Castlegate Sandstone, Central Utah, U.S.A.: *Journal of Sedimentary Research*, 82, 121-130.
- Hajek, E.A., and Straub, K.M., 2017, Autogenic sedimentation in clastic stratigraphy: *Annual Review of Earth and Planetary Sciences*, 45, 681-709.

- Hajek, E.A., Heller, P.L., and Sheets, B.A., 2010, Significance of channel-belt clustering in alluvial basins: *Geology*, v. 38, p. 535-538.
- Havholm, K.G., 1991, Eolian event stratigraphy: theory, and application to the middle Jurassic Page Sandstone, Colorado Plateau, U.S.A.: Unpublished Ph.D. Dissertation, University of Texas at Austin, Austin, 181 p.
- Havholm, K.G., and Kocurek, G., 1994, Factors controlling aeolian sequence stratigraphy: clues from super bounding surface features in the Middle Jurassic Page Sandstone: *Sedimentology*, 41, 913-934.
- Havholm, K.G., Blakey, R.C., Capps, M., Jones, L.S., King, D.D., and Kocurek, G., 1993. Aeolian genetic stratigraphy: an example from the Middle Jurassic Page sandstone, Colorado Plateau, *in* Pye, K., and Lancaster, N., eds., *Aeolian Sediments: Ancient and Modern*: International Association of Sedimentologists, Special Publication 16, 87–107.
- Hayden, A.T., Lamb, M.P., Fischer, W.W., Ewing, R.C., McElroy, B.J., and Williams, R.M.E., 2019, Formation of sinuous ridges by inversion of river-channel belts in Utah, USA, with implications for Mars: *Icarus*, 332, 92-110.
- Heller, P.L., and Paola, C., 1996, Downstream changes in alluvial architecture: an exploration of controls on channel-stacking patterns: *Journal of Sedimentary Research*, 66, 297-306.
- Hooke, J.M., and Yorke, L. (2011) Channel bar dynamics on multi-decadal timescales in an active meandering bar. *Earth Surface Processes and Landforms*, 36, 1910-1928.

- Hubbard, S.M., Smith, D.G., Nielsen, H., Leckie, D.A., Fustic, M., Spencer, R.J., and Bloom, L., 2011, Seismic geomorphology and sedimentology of a tidally influenced river deposit, Lower Cretaceous Athabasca oil sands, Alberta, Canada: American Association of Petroleum Geologists Bulletin, 95, 1123-1145.
- Hughes, C.M., Cardenas, B.T., Goudge, T.A., and Mohrig, D., 2019, Deltaic deposits indicative of a paleo-coastline at Aeolis Dorsa, Mars: Icarus, 317, 442-453.
- Hunter, R.E., 1977, Basic types of stratification in small eolian dunes: Sedimentology, 24, 361-387.
- Hunter, R.E., and Rubin, D.M., 1983, Interpreting cyclic crossbedding, with an example from the Navajo Sandstone, in Brookfield, M.E., and Ahlbrandt, T.S., eds., Eolian Sediments and Processes: Amsterdam, Elsevier, 429-454.
- Ikeda, H., 1989, Sedimentary controls on channel migration and origin of point bars in sand-bedded meandering rivers. In S. Ikeda and G. Parker (Eds.), River Meandering: Water Resources Monograph, 12, 51-68. American Geophysical Union: Washington, D.C.
- Ikeda, S., Parker, G., and Sawai, K., 1981, Bend theory of river meanders. Part 1. Linear development: Journal of Fluid Mechanics, 112, 363-377.
- Jerolmack, D.J., and Mohrig, D., 2005, Frozen dynamics of migrating bedforms: Geology, 33, 57-60.
- Jerolmack, D.J., and Mohrig, D., 2007, Conditions for branching in depositional rivers: Geology, 35, 463-466.

- Jerolmack, D.J., and Paola, C., 2010, Shredding of environmental signals by sediment transport: *Geophysical Research Letters*, 37, L19401.
- Jobe, Z.R., Howes, N.C., and Auchter, N.C., 2016, Comparing submarine and fluvial channel kinematics: Implications for stratigraphic architecture: *Geology*, 44, 931-934.
- Jones, H.L., and Hajek, E.A., 2007, Characterizing avulsion stratigraphy in ancient alluvial deposits: *Sedimentary Geology*, 202, 124-137.
- Jones, L.S., and Blakey, R.C., 1993, Erosional remnants and adjacent unconformities along an eolian-marine boundary of the Page Sandstone and Carmel Formation, Middle Jurassic, South-Central Utah: *Journal of Sedimentary Petrology*, 63, 852-859.
- Kim, W., Paola, C., Swenson, J.B., and Voller, V.R., 2006, Shoreline response to autogenic processes of sediment storage and release in the fluvial system: *Journal of Geophysical Research: Earth Surface*, 111, F04013.
- Kite, E.S., Howard, A.D., Lucas, A.S., Armstrong, J.C., Aharonson, O., and Lamb, M.P., 2015, Stratigraphy of Aeolis Dorsa, Mars: Stratigraphic context of the great river deposits: *Icarus*, 253, 223-242.
- Kocurek, G., 1981, Significance of interdune deposits and bounding surfaces in aeolian dune sands: *Sedimentology*, 28, 753-780.
- Kocurek, G., 1988, First-order and super bounding surfaces in eolian sequences— Bounding surfaces revisited: *Sedimentary Geology*, 56, 193–206.

- Kocurek, G., and Day, M.D., 2018, What is preserved in the aeolian rock record? A Jurassic Entrada Sandstone case study at the Utah–Arizona border: *Sedimentology*, 65, 1301-1321.
- Kocurek, G., and Dott, R.H., Jr., 1981, Distinctions and uses of stratification types in the interpretation of eolian sand: *Journal of Sedimentary Petrology*, 51, 579–595.
- Kocurek, G., and Havholm, K.G., 1993, Eolian sequence stratigraphy—A Conceptual framework: Chapter 16: Recent Developments in Siliciclastic Sequence Stratigraphy, *in* Weimer, P., and Posamentier, H., eds., M58: Siliciclastic Sequence Stratigraphy: Recent Developments and Applications: American Association of Petroleum Geologists, Memoirs 58, 393-409.
- Kocurek, G., and Hunter, R.E., 1986, Origin of polygonal fractures in sand, uppermost Navajo and Page sandstones, Page, Arizona: *Journal of Sedimentary Research*, 56, 895–904.
- Kocurek, G., Carr, M., Ewing, R., Havholm, K.G., Nagar, Y.C., and Singhvi, A.K., 2007, White Sands Dune Field, New Mexico: Age, dune dynamics and recent accumulations: *Sedimentary Geology*, 197, 313-331.
- Kocurek, G., Ewing, R.C., and Mohrig, D., 2010, How do bedform patterns arise? New views on the role of bedform interactions within a set of boundary conditions: *Earth Surface Processes and Landforms*, 35, 51–63.
- Kocurek, G., Knight, J., and Havholm, K., 1991, Outcrop and semi-regional three-dimensional architecture and reconstruction of a portion of the eolian Page

- Sandstone (Jurassic): *in* Miall, A.D., and Tyler, N., eds., SEPM, Concepts in Sedimentology and Paleontology 3, 25-43.
- Kocurek, G., Robinson, N.I., and Sharp Jr., J.M., 2001, The response of the water table in coastal aeolian systems to changes in sea level: *Sedimentary Geology*, 139, 1-13.
- Kowallis, B.J., Heaton, J.S., and Bringham, K. (1986) Fission-track dating of volcanically derived sedimentary rocks. *Geology*, 14, 19-22.
- Lazarus, E.D., and Constantine, J.A. (2013) Generic theory for channel sinuosity. *Proceedings of the National Academy of Sciences*, 110, 8447-8452.
- Leclair, S.F., Bridge, J.S., and Wang, F., 1997, Preservation of cross-strata due to migration of subaqueous dunes over aggrading and non-aggrading beds: comparison of experimental data with theory: *Geoscience Canada*, 24, 55-66.
- Liu, J., and Marfurt, K.J., 2007, Instantaneous spectral attributes to detect channels: *Geophysics*, v. 72, p. 23-31.
- Mahon, R.C., and McElroy, B., 2018, Indirect estimation of bedload flux from modern sand-bed rivers and ancient fluvial strata: *Geology*, 46, 579-582.
- Maizels, J., 1990, Raised channel systems as indicators of palaeohydrologic change: a case study from Oman: *Palaeogeography, Palaeoclimatology, Palaeoecology*, 76, 241–277.
- Maizels, J., and McBean, C., 1990, Cenozoic alluvial fan systems of interior Oman: palaeoenvironmental reconstruction based on discrimination of palaeochannels using remotely sensed data: Geological Society, London, Special Publications, 49, 565–582.

- Maizels, J.K., 1987, Plio-Pleistocene raised channel systems of the western Sharqiya (Wahiba), Oman: Geological Society, London, Special Publications, 35, 31–50.
- Mason, J., and Mohrig, D., submitted, Scroll bars are inner bank levees along bends in meandering rivers.
- Mason, J., and Mohrig, D., 2018, Using time-lapse lidar to quantify river bend evolution on the meandering coastal Trinity River, Texas, USA: *Journal of Geophysical Research: Earth Surface*, 123, 1133-1144.
- Mason, J., and Mohrig, D., in review, Bedform groups during flood on the Trinity River – a new scale of self-organization in river bottom topography.
- McDonald, R.R., and Anderson, R.S., 1995, Experimental verification of aeolian saltation and lee side deposition models: *Sedimentology*, 42, 39-56.
- McKee, E.D., and Weir, G.W., 1953, Terminology for stratification and cross-stratification in sedimentary rocks: *Geological Society of America Bulletin*, 64, 381–390.
- Miall, A.D., 1985, Architectural-element analysis: a new method of facies analysis applied to fluvial deposits: *SEPM Special Publication-Recognition of Fluvial Depositional Systems and Their Resource Potential*, 19, 33-81.
- Miall, A.D., 1988, Architectural elements and bounding surfaces in fluvial deposits: anatomy of the Kayenta formation (lower Jurassic), Southwest Colorado: *Sedimentary Geology*, 55, 233–262.
- Miall, A.D., 2002, Architecture and sequence stratigraphy of Pleistocene fluvial systems in the Malay basin, based on seismic time-slice analysis: *American Association of Petroleum Geologists Bulletin*, 86, 1201-1216.

- Miall, A.D., 2015, Updating uniformitarianism: stratigraphy as just a set of ‘frozen accidents’: Geological Society, London, Special Publications, 404, 11-36.
- Milliken, R.E., Ewing, R.C., Fischer, W.W., and Hurowitz, J., 2014, Wind-blown sandstones cemented by sulfate and clay minerals in Gale Crater, Mars: Geophysical Research Letters, 41, 1149-1154.
- Mohrig, D., and Smith, J.D., 1996, Predicting the migration rates of subaqueous dunes: Water Resources Research, 32, 3207-3217.
- Mohrig, D., Heller, P.L., Paola, C., and Lyons, W.J., 2000, Interpreting avulsion process from ancient alluvial sequences: Guadalupe-Matarranya system (northern Spain) and Wasatch Formation (western Colorado): Geological Society of America Bulletin, 112, 1787–1803.
- Nickling, W.G., McKenna Neuman, C., and Lancaster, N., 2002, Grainfall processes in the lee of transverse dunes, Silver Peak, Nevada: Sedimentology, 49, 191-209.
- Nield, J.M., Wiggs, G.F.S., Baddock, M.C., and Hipondoka, M.H.T., 2017, Coupling leeside grainfall to avalanche characteristics in aeolian dune dynamics: Geology, 45, 271-274.
- Nittrouer, J.A., Mohrig, D., Allison, M.A., and Peyret, A.-P. B., 2011a, The lowermost Mississippi River: a mixed bedrock-alluvial channel: Sedimentology, 58, 1914-1934.
- Nittrouer, J.A., Mohrig, D., and Allison, M., 2011b, Punctuated sand transport in the lowermost Mississippi River: Journal of Geophysical Research: Earth Surface, 116, F04025.

- Nuse, B., 2015, Flow processes and sedimentation in a low-sinuosity high net-sand content fluvial channel belt: 3D outcrop study of the Cedar Mountain Formation, Utah: Unpublished MS Thesis, Colorado School of Mines.
- Owen, A., Nichols, G.J., Hartley, A.J., Weissmann, G.S., and Scuderi, L.A., 2015, Quantification of a distributive fluvial system: The Salt Wash DFS of the Morrison Formation, SW U.S.A.: *Journal of Sedimentary Research*, 85, 544-561.
- Paola, C., and Borgman, L., 1991, Reconstructing random topography from preserved stratification: *Sedimentology*, 38, 553–565.
- Paola, C., Ganti, V., Mohrig, D., Runkel, A.C., and Straub, K.M., 2018, Time not our time: Physical controls on the preservation and measurement of geologic time: *Annual Review of Earth and Planetary Sciences*, 46, 409-438.
- Paola, C., Straub, K., Mohrig, D., and Reinhardt, L., 2009, The “unreasonable effectiveness” of stratigraphic and geomorphic experiments: *Earth-Science Reviews*, 97, 1-43.
- Parker, G., Paola, C., Whipple, K.X., and Mohrig, D., 1998, Alluvial fans formed by channelized fluvial and sheet flow. I: Theory: *Journal of Hydraulic Engineering*, 124, 985-995.
- Parker, G., Wilcock, P.R., Paola, C., Dietrich, W.E., and Pitlick, J. (2007) Physical basis for quasi-universal relations describing bankfull hydraulic geometry of single-thread gravel bed rivers. *Journal of Geophysical Research – Earth Surface*, 112, F04005.

- Pedersen, A., Kocurek, G., Mohrig, D., and Smith, V., 2015, Dune deformation in a multi-directional wind regime: White Sands Dune Field, New Mexico: *Earth Surface Processes and Landforms*, 40, 925-941.
- Peterson, F., 1994, Sand dunes, sabkhas, streams, and shallow seas: Jurassic paleogeography in the southern part of the Western Interior Basin, *in* Caputo, M.V., Peterson, N.A., and Franczyk, K.J., eds., *Mesozoic Systems of the Rocky Mountain Region, USA: SEPM, Rocky Mountain Section*, 233–272.
- Peterson, F., and Ryder, R.T., 1975, Cretaceous rocks in the Henry Mountains region, Utah and their relation to neighboring regions. *in* *Four Corners Geological Society Guidebook*, 8, p. 166-189.
- Ping, L., Narteau, C., Dong, Z., Zhang, Z., and Courrech du Pont, S., 2014, Emergence of oblique dunes in a landscape-scale experiment. *Nature Geoscience*, 7, 99.
- Pipiringos, G.N., and O’Sullivan, R.B., 1978, Principal unconformities in Triassic and Jurassic rocks, western interior United States; a preliminary survey: *United States Geologic Survey, Professional Paper*, 1035–A, 35 p.
- Pizzuto, J.E., 1987, Sediment diffusion during overbank flows: *Sedimentology*, 34, 301–317.
- Reesink, A.J.H., Van den Berg, J.H., Parsons, D.R., Amsler, M.L., Best, J.L., Hardy, R.J., Orfeo, O., and Szupiany, R.N., 2015, Extremes in dune preservation: Controls on the completeness of fluvial deposits: *Earth-Science Reviews*, 150, 652-665.
- Reitz, M.D., Jerolmack, D.J., and Swenson, J.B., 2010, Flooding and flow path selection on alluvial fans and deltas: *Geophysical Research Letters*, 37, L06401.

- Riggs, N.R., and Blakey, R.C., 1993, Early and Middle Jurassic Paleogeography and Volcanology of Arizona and Adjacent Areas, *in* Dunne, G.C., and McDougall, K.A., eds., Mesozoic Paleogeography of the Western United States – II: SEPM, Pacific Section 71, 347–375.
- Rodríguez-López, J.P., Clemmensen, L.B., Lancaster, N., Mountney, N.P., and Veiga, G.D., 2014, Archean to Recent aeolian sand systems and their sedimentary record: Current understanding and future prospects: *Sedimentology*, 61, 1487–1534.
- Romans, B.W., Castellort, S., Covault, J.A., Fildani, A., and Walsh, J.P., 2016, Environmental signal propagation in sedimentary systems across timescales: *Earth-Science Reviews*, 153, 7-29.
- Rubin, D.M., 1987, Cross-Bedding, Bedforms, and Paleocurrents: SEPM, Concepts in Sedimentology and Paleontology 1, 187 p.
- Rubin, D.M., and Hunter, R.E., 1982, Bedform climbing in theory and nature: *Sedimentology*, 29, 121–138.
- Rubin, D.M., and Hunter, R.E., 1987, Bedform alignment in directionally varying flows: *Science*, 237, 276–278.
- Sadler, P.M., 1981, Sediment accumulation rates and the completeness of stratigraphic sections: *The Journal of Geology*, 89, 569-584.
- Sadler, P.M., and Jerolmack, D.J., 2015, Scaling laws for aggradation, denudation and progradation rates: the case for time-scale invariance at sediment sources and sinks: Geological Society, London, Special Publications, 404, 69-88.

- Seminara, G., and Tubino, M., 1989, Alternate bars and meandering: Free, forced and mixed interactions. In S. Ikeda and G. Parker (Eds.), *River Meandering: Water Resources Monograph*, 12, 267-320. American Geophysical Union: Washington, D.C.
- Shaw, J.B., and Mohrig, D., 2014, The importance of erosion in distributary channel network growth, Wax Lake Delta, Louisiana, USA: *Geology*, 42, 31-34.
- Simms, A.R., Anderson, J.B., Milliken, K.T., Taha, Z.P., and Wellner, J.S., 2007, Geomorphology and age of the Oxygen isotope stage 2 (last lowstand) sequence boundary on the northwestern Gulf of Mexico continental shelf: *Geological Society, London, Special Publications*, 277, 29-46.
- Skelly, R.L., Bristow, C.S., and Ethridge, F.G., 2003, Architecture of channel-belt deposits in an aggrading shallow sandbed braided river: the lower Niobrara River, northeast Nebraska: *Sedimentary Geology*, 158, 249-270.
- Slingerland, R., and Smith, N.D., 2004, River avulsions and their deposits: *Annual Review of Earth and Planetary Sciences*, 32, 257-285.
- Stokes, W.L., 1961, *Fluvial and Eolian Sandstone Bodies in Colorado Plateau: AAPG SP-Geometry of Sandstone Bodies*, 22, 151-178.
- Stouthamer, E., and Berendsen, H.J.A., 2001, Avulsion frequency, avulsion duration, and interavulsion period of Holocene channel belts in the Rhine-Meuse Delta, the Netherlands: *Journal of Sedimentary Research*, 71, 589-598.
- Stouthamer, E., and Berendsen, H.J.A., 2007, Avulsion: The relative roles of autogenic and allogenic processes: *Sedimentary Geology*, 198, 309-325.

- Swanson, T., Mohrig, D., and Kocurek, G., 2016, Aeolian dune sediment flux variability over an annual cycle of wind: *Sedimentology*, 63, 1753–1764.
- Swanson, T., Mohrig, D., Kocurek, G., and Liang, M., 2017, A Surface Model for Aeolian Dune Topography: *Mathematical Geosciences*, 49, 635–655.
- Swanson, T., Mohrig, D., Kocurek, G., Cardenas, B.T, and Wolinsky, M.A., 2019, Preservation of autogenic processes and allogenic forcings within set-scale aeolian architecture I: numerical experiments: *Journal of Sedimentary Research*, accepted.
- Swanson, T., Mohrig, D., Kocurek, G., Perillo, M., and Venditti, J., 2018, Bedform spurs: a result of a trailing helical vortex wake: *Sedimentology*, 65, 191-208.
- Swartz, J.M., Mohrig, D., Passalacqua, P., Goff, J., and Gulick, S.P.S., in prep.
- Swartz, J.M., Mohrig, D., Passalacqua, P., Goff, J., and Gulick, S.P.S. (2018) From distributary to tributary: coastal drainage network position and morphometry are set by depositional processes. Presented at the American Geophysical Union 2018 Fall Meeting, EP21B-2230.
- Swezey, C., 1991, Description and interpretation of the Jurassic J-2 unconformity of the Western Interior (U.S.A.): Unpublished MS Thesis, University of Texas at Austin, Austin, 144 p.
- Taggart, S., Hampson, G.J., and Jackson, M.D., 2010, High-resolution stratigraphic architecture and lithological heterogeneity within marginal aeolian reservoir analogues: *Sedimentology*, 57, 1246–1279.
- Van De Lagewag, W.Y., Van Dijk, W.M., and Kleinans, M.G. (2013) Channel belt architecture formed by a meandering river. *Sedimentology*, 60, 840-859.

- van der Mark, C.F., Blom, .A., and Hulscher, S.J.M.H., 2008, Quantification of variability in bedform geometry: *Journal of Geophysical Research*, 113, F03020.
- Wang, J., and Bhattacharya, J.P., 2017, Plan-view paleochannel reconstruction of amalgamated meander belts, Cretaceous Ferron Sandstone, Notom Delta, south-central Utah, U.S.A: *Journal of Sedimentary Research*, 88, 58–74.
- Wang, Y., Straub, K.M., and Hajek, E.A., 2011, Scale-dependent compensational stacking: An estimate of autogenic time scales in channelized sedimentary deposits: *Geology*, 39, 811-814.
- Werner, B.T., 1995, Eolian dunes: computer simulations and attractor interpretation: *Geology*, 23, 1107–1110.
- Whiting, P.J., and Dietrich, W.E., 1993, Experimental constraints on bar migration through bends: Implications for meander wavelength selection: *Water Resources Research*, 29, 1091-1102.
- Willett, S.D., McCoy, S.W., Perron, J.T., Goren, L., and Chen, C.-Y., 2014, Dynamic reorganization of river basins: *Science*, v. 343, no. 1248765.
- Williams, R.M.E., Chidsey Jr., T.C., and Eby, D.E., 2007, Exhumed Paleochannels in Central Utah—Analog for Raised Curvilinear Features on Mars: *Central Utah-Diverse Geology of a Dynamic Landscape*, 221–235.
- Williams, R.M.E., Irwin, R.P., and Zimbelman, J.R., 2009, Evaluation of paleohydrologic models for terrestrial inverted channels: Implications for application to Martian sinuous ridges: *Geomorphology*, 107, 300–315.

- Wood, L.J., 2007, Quantitative seismic geomorphology of Pliocene and Miocene fluvial systems in the northern Gulf of Mexico, U.S.A.: *Journal of Sedimentary Research*, 77, 713-730.
- Wright, S., and Parker, G. (2003) Grain-size specific suspended sediment transport and flow resistance in large sand-bed rivers. In A. Gyr and W. Kinzelbach (Eds.), *Sedimentation and Sediment transport*, 221-227. Netherlands: Springer.
- Wu, C., Bhattacharya, J.P., and Ullah, M.S., 2015, Paleohydrology and 3D facies architecture of ancient point bars, Ferron Sandstone, Notom Delta, South-central Utah, USA: *Journal of Sedimentary Research*, 85, 399–418.
- Wu, C., Ullah, M.S., Lu, J., and Bhattacharya, J.P., 2016, Formation of point bars through rising and falling flood stages: Evidence from bar morphology, sediment transport and bed shear stress: *Sedimentology*, 63, 1458–1473.
- Zaitlin, B.A., Dalrymple, R.W., and Boyd, R., 1994, The stratigraphic organization of incised-valley systems associated with relative sea-level change: in Dalrymple, R.W., Boyd, R., and Zaitlin, B.A., eds., *Incised-Valley Systems: Origin and Sedimentary Sequences*: SEPM, Special Publication 51, p. 45-60.
- Zaki, A.S., Pain, C.F., Edgett, K.S., and Giegengack, R., 2018, Inverted stream channels in the Western Desert of Egypt. Synergistic remote, field observations and laboratory analysis on Earth with applications to Mars: *Icarus*, 309, 105-124.